Excitons and polaritons in two-dimensional transition metal dichalcogenides: a tutorial

EUNICE PAIK,[1] LONG ZHANG,[1,2] KIN FAI MAK,[3,4,5] JIE SHAN,[3,4,5] AND HUI DENG[1*]

[1]*Department of Physics, University of Michigan, Ann Arbor, MI 48109, USA*
[2]*Department of Physics, College of Physical Science and Technology, Xiamen University, Xiamen 361005, China*
[3]*Department of Physics, Cornell University, Ithaca, NY, USA*
[4]*School of Applied and Engineering Physics, Cornell University, Ithaca, NY, USA*
[5]*Kavli Institute at Cornell for Nanoscale Science, Ithaca, NY, USA*
[*]*dengh@umich.edu*

Contents

Abstract: Since the discovery of two-dimensional transition metal dichalcogenides monolayers as a direct band-gap semiconductors with pronounced room-temperature exciton transitions, research on excitons and polaritons in these materials have exploded worldwide. Here, we give an introductory tutorial on the basic properties of excitons and polaritons in these materials, emphasizing how they are different from those in conventional semiconductors, and discuss some of the most exciting new phenomena reported.

1. Introduction and overview

An exciton is an electron-hole quasi-particle that is an elementary unit of optical excitation in solids. It serves as a basis of light-matter interactions in semiconductor materials and modern optoelectronics technology. Exciton polaritons are new elementary excitations formed in solids when the exciton and light interaction enters the strong-coupling regime. They are light and matter hybrid quasiparticles that may allow us to combine the best of both worlds for exploration of many-body physics phenomena and development of new technologies.

While excitons and polaritons have been extensively studied in group III-V and II-VI semiconductors such as GaAs, GaN, CdTe and ZnO, the emergence of van der Waals semiconductors has opened doors to new opportunities unavailable in conventional materials. Van der Waals materials encompass a wide range of materials, including insulators, semiconductors, semimetals, magnets, and ferroics. The burgeoning field of 2D materials has been revolutionized by the discovery of graphene exfoliation in 2004 [1]. This discovery has propelled and expanded the research on 2D materials and continues to attract research interest. In this tutorial, we focus on transitional metal dichalcogenides (TMDCs), which are direct band-gap semiconductors in the monolayer form. They have a large binding energy, spin-valley degree of freedom, and ease of heterostructure engineering, making them an interesting playground for exploring exciton physics and novel exciton-polariton optoelectronic devices.

This article will give a tutorial on excitons and exciton-polariton physics in TMDCs and summarize the current progress in the field. We will introduce in the remainder of this section the general properties of 2D materials and light-matter interactions in 2D materials, then we will discuss in Section 2 properties of excitons in TMDCs, in Section 3 collective phenomena

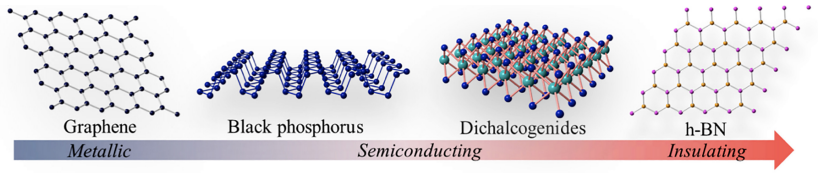

Fig. 1. Types of 2D materials. Reprinted from [W. Liao, Y. Huang, H. Wang, and H. Zhang, Appl. Mater. Today, 16, 435–455, 2019], with permission from Elsevier [2].

observed in TMDC exciton systems, and in Section 4 properties of TMDC exciton-polaritons. We will conclude in Section 5.

1.1. Two-dimensional materials

Van der Waals (vdW) 2D materials are layered atomic sheets bound by vdW forces, and encompasses metals, semiconductors, and insulators (Figure 1). Geim and Novoselov's Nobel Prize-winning work pioneered the field of 2D materials by isolating a single layer of graphene using scotch tape [1]. TMDCs are a class of 2D materials that have an indirect band gap (like silicon) in bulk form but have a direct band gap (like GaAs) in the monolayer limit. Unlike conventional 3D semiconductors, TMDCs have a reduced dimensionality, which enables exceptionally strong interactions with light and integration with a wide range of substrates. TMDC heterostructures can be constructed by stacking different combinations of TMDCs, allowing customizable optical, electrical, and structural properties while retaining the benefits of monolayer TMDCs. For instance, the optical properties can be engineered by changing the specific combination of TMDCs used to form heterostructures. Furthermore, the ability to manipulate the electronic band structures by changing the twist angle between layers opens up possibilities of studying strongly correlated physics. These unique optical and structural properties prompted active research of TMDCs for photonics and optoelectronic applications [3].

In 2D materials, exciton experiences reduced dielectric screening compared to 3D materials. Therefore, the exciton binding energy in 2D material is larger than in 3D materials. Due to their strong binding energy, excitons and exciton-polaritons in TMDCs can persist up to room temperature, making them a good candidate for room temperature photonics and optoelectronics. In addition, excitons dominate the optical spectrum of TMDCs, resulting in strong absorption and emission with measurable absorption. Lastly, higher-order excitonic transitions, which are analogous to the Rydberg series in the hydrogen atom, appear in the optical measurements of TMDCs.

Another unique property of TMDCs is the spin-valley physics of excitons and exciton-polaritons, which arises because of the broken inversion symmetry in the material. The inversion symmetry is broken because TMDCs have a hexagonal crystal structure with neighboring lattice sites occupied by different atoms. The broken symmetry results in degenerate direct band gap minima at the K and K' valleys at the corners of the hexagonal Brillouin zone. This contrasts with GaAs and other III-V semiconductors, where the band gap minima are at the center of the Brillouin zone, or the Γ point. Monolayer TMDCs have a strong spin-orbit interaction that leads to spin splitting at the valleys, which is opposite for the K and K' valleys. Consequently, the K and K' valleys are addressable with opposite circular polarizations of light, opening new ways of encoding and processing information using the valley degree of freedom. The formation of exciton-polaritons can further increase the practicality of spin-valley physics because the light effective mass of exciton-polaritons allows a longer diffusion length and further propagation of the 'information' stored in the valleys.

Engineering heterostructures with 3D materials could pose technical challenges because it is limited by epitaxial growth and lattice matching conditions. Therefore, the options for material

combinations and types of substrates are limited. On the other hand, 2D material heterostructures offer more flexibility and degrees of freedom. The layers of 2D materials are held together by relatively weak van der Waals forces, and the layers can be separated by exfoliation and carefully restacked to have arbitrary twist angles between layers. The twist angle and lattice mismatch between layers can introduce a moiré superlattice, which is a periodic variation of lattice alignment and stacking order in a heterostructure. The moiré superlattice results in a periodic modification of the potential landscape and can lead to excitons localization and modified optical selection rules. Thus, TMDC moiré heterostructures are a good platform to study correlated electronic states and collective many-body phenomena.

1.2. Light matter interactions for photonics

When carriers (electrons and holes) in TMDCs are excited by a laser, they form excitons, which are electron-hole pairs bound by Coulomb forces. Excitons can recombine to emit light. The binding energy is related to the strength of light-matter interaction, characterized by the oscillator strength, which has a fundamental impact on many optical properties of the material.

In monolayers, excitons are tightly confined in the in-plane direction and are referred to as intralayer excitons. Intralayer excitons have a large binding energy that is an order of magnitude greater than that of GaAs. Therefore, monolayer exciton emission can persist at room temperature and strongly interact with light.

In hetero- or homobilayers, electrons and holes can be spatially separated into different layers, resulting in interlayer excitons. Interlayer excitons have smaller oscillator strength compared to intralayer excitons, therefore weakly interact with light and have longer radiative lifetimes. Interlayer excitons also have a permanent out-of-plane dipole moment, which may facilitate electrical tuning of exciton properties [4–6] and collective many-body phenomena such as exciton condensation and superfluidity [7,8]. Moiré superlattices may form in heterostructures, providing unprecedented tunability of the excitonic band structures.

Photonic cavities provide a method of controlling and enhancing the interactions between excitons and photons in TMDCs. The exciton-photon interaction strength determines two distinct regimes of light-matter coupling: weak coupling and strong coupling. In the weak coupling regime, the decay rate is greater than the energy exchange rate. The spontaneous emission is irreversible but enhanced by the cavity, characterized by the Purcell factor (Figure 2(b)). Conventional photon lasing operates in this regime. Interlayer TMDC excitons have a smaller oscillator strength and therefore couple weakly with the cavity photons and generally remain in the weak coupling regime. In the strong coupling regime, the exciton and the cavity photon energy exchange rate (the coupling strength) is greater than the decay rates of the system and results in a reversible spontaneous emission rate and a formation of new hybridized eigenmodes called exciton-polaritons (Figure 2(a)). Exciton-polaritons are a unique platform for observing many-body phenomena and developing ultra-low threshold semiconductor lasers. Intralayer TMDC excitons are ideal for studying exciton-polaritons due to their strong oscillator strength.

2. Excitons in TMDCs: theory and experiments

An exciton is an electron-hole quasiparticle that is an elementary unit of optical excitation in solids. It serves as the basis of light-matter interactions in semiconductor materials. Semiconductors have a valence band filled with electrons and an empty conduction band. When the electron in the valence band is excited to the conduction band by an external source, it leaves behind a positively charged hole. The electron and hole are bound by Coulomb interaction forces and form an energetically favorable quasiparticle called excitons. The exciton electron-hole pair forms a dipole moment that interacts with the electromagnetic field of light and therefore serves as an essential component of photonic devices. In this chapter, we will discuss the theoretical and experimental work on excitons in monolayer TMDCs and introduce excitons in heterostructures.

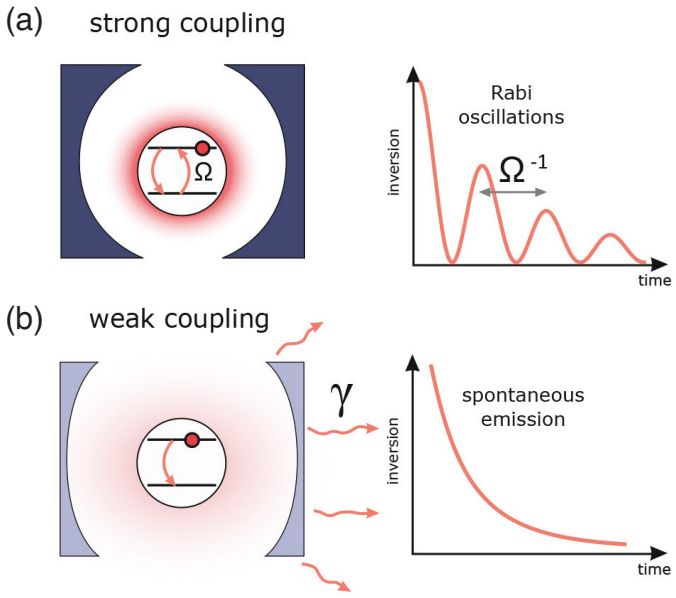

Fig. 2. Strong coupling versus weak coupling. (a) Schematic illustration of strong coupling. Ω is the exciton-photon coupling constant. (b) Schematic illustration of weak coupling. γ is the spontaneous decay rate. Reprinted with permission from [D. G. Baranov, M. Wersäll, J. Cuadra, T. J. Antosiewicz, and T. Shegai, ACS Photonics, 5, 24–42, 2018] [9]. Copyright 2018 American Chemical Society.

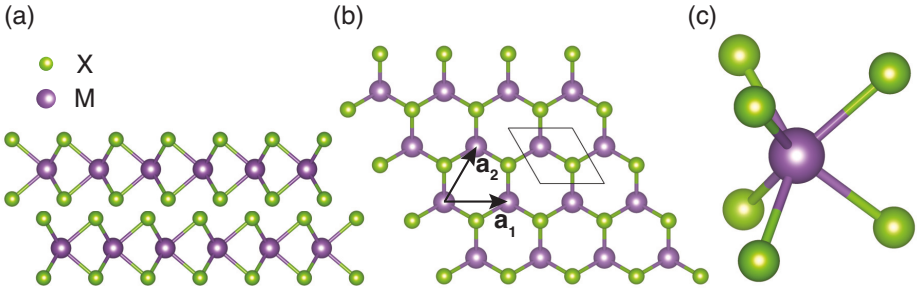

Fig. 3. Crystal structure of TMDCs. (a) Side view of two TMDC layers showing a 2H stacking structure. (b) Top view of the hexagonal crystal lattice structure. $\vec{a}_1$ and $\vec{a}_2$ indicate the Bravais lattice vectors and the polygon shape outlines the unit cell. (c) Unit cell of MX_2 with a trigonal prismatic geometry. Drawings created using VESTA.

2.1. Theory of excitons in Monolayer TMDCs

Unlike multilayers, TMDC monolayers have a direct band gap. Excitons in monolayers feature a strong binding energy, large oscillator strength, and momentum valley physics. This makes monolayer excitons, or, intralayer excitons, a fundamental component of studying light-matter interactions in TMDCs.

2.1.1. Crystal structure of monolayer TMDCs

Bulk TMDC crystals are composed of atomically thin layers of materials that are bound together by vdW forces. Because vdW forces are weak in comparison to the covalent bonds between

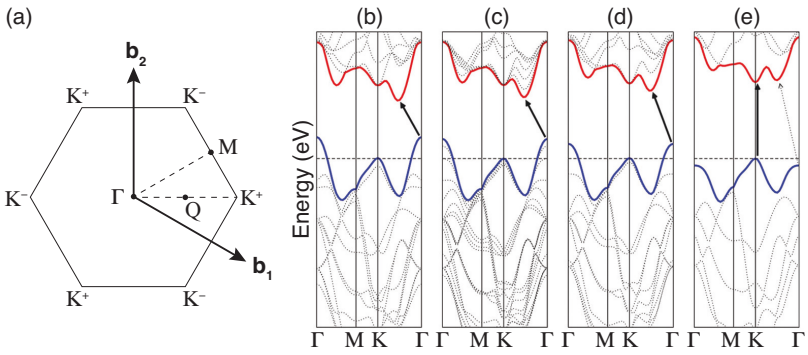

Fig. 4. Electronic band structure of TMDCs. (a) Hexagonal Brillouin zone (BZ) reciprocal lattice structure. $\vec{b}_1$ and $\vec{b}_2$ are reciprocal lattice basis vectors, and Γ, M, $K^{\pm}$, Q are symmetry points. (b-e) Electronic band structures of (b) bulk, (c) quadrilayer, (d) bilayer, and (e) monolayer MoS_2 calculated using density functional theory (DFT). The solid arrows indicate the lowest energy transition. Reprinted with permission from [A. Splendiani, L. Sun, Y. Zhang, T. Li, J. Kim, C.-Y. Chim, G. Galli, and F. Wang, Nano Lett., 10, 1271–1275, 2010] [11]. Copyright 2010 American Chemical Society.

atoms, the layers of material can be peeled off down to a single layer. This process is called exfoliation. The bulk crystal has a 2H stacking order, with each layer rotated by 180 degrees with respect to the neighboring layers, as shown in Figure 3(a).

A single layer of TMDC material is about 6 – 7 Å thick and has a hexagonal lattice structure in the in-plane direction, with alternating transition metal and chalcogen atoms occupying each lattice site as depicted in Figure 3(b). This alternating occupation of atoms breaks the inversion symmetry, which has important consequences for the electronic and optical properties. The unit cell of MX_2 has a trigonal prismatic molecular geometry, with the transition metal as the central atom, and six chalcogen atoms arranged at the vertices of the triangular prism (Figure 3(c)). The Bravais lattice is spanned by basis vectors:

$$\vec{a}_1 = (a, 0, 0), \quad \vec{a}_2 = \frac{a}{2}(1, \sqrt{3}, 0), \tag{1}$$

and the reciprocal lattice has the basis vectors:

$$\vec{b}_1 = \frac{4\pi}{\sqrt{3}a}\left(\frac{\sqrt{3}}{2}, -\frac{1}{2}, 0\right), \quad \vec{b}_2 = \frac{4\pi}{\sqrt{3}a}(0, 1, 0) \tag{2}$$

[10].

2.1.2. Band structure of monolayer TMDCs

In solid state physics, a single free electron in a periodic lattice structure can be represented by Bloch waves, and the periodic modulation of the potential opens gaps in the energy band structure. The local extrema in the band structure are called ‘valleys’. The crystal structure of TMDCs result in a hexagonal Brillouin zone (BZ) in reciprocal space with valleys at the K^+ and K^- points as depicted in Figure 4(a).

TMDCs have a direct band gap at the K^+ and K^- points in the monolayer limit. To explain this, we can consider the electronic band structure of bulk TMDCs. The direct band gap in monolayers occurs at the K point while the indirect band gap in multilayers occurs at the Γ point. The out-of-plane mass for electrons and holes at the K point exceeds the free electron mass, while at the Γ point it is a fraction of the free electron mass [12]. Therefore, reducing the layer number

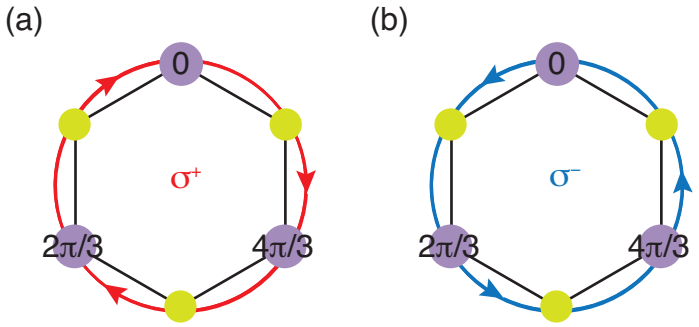

Fig. 5. Valley-contrasting Berry curvature. Opposite valley curvature in (a) K^+ and (b) K^- valleys results in opposite helicity of circularly polarized light coupled to each valley.

results in increased quantum confinement, which causes an increase in the indirect band gap, while the direct band gap remains the same. Comparing the monolayer TMDC band structure to that of graphene, graphene has a linear Dirac cone dispersion with a closed band gap, while monolayer TMDCs have a parabolic dispersion with an open band gap. This difference is due to the broken sub-lattice symmetry in TMDCs as compared to graphene, which results from the alternating occupation of lattice sites by transition metal and dichalcogenide atoms [13]. density functional theory (DFT) calculations show the band structure of the TMDC monolayers in more detail. Figures 4(b-e) are DFT calculated band structures of multilayers and monolayer MoS_2, which show the lowest energy valence-to-conduction band transition to be indirect in multilayers and direct in monolayers.

2.1.3. Spin-Valley locking

A unique property that monolayer TMDCs have over other conventional semiconductors is their spin-valley properties and valley-dependent optical selection rules. The monolayer unit cell has a trigonal prismatic crystal structure, and the inversion symmetry is broken. In other words, if we take the transition metal as the inversion center and perform the space-inversion transformation, the chalcogen atoms will be mapped to an empty lattice site. This broken symmetry results in changes in the band structure property, namely the large spin-orbit coupling and the valley-contrasting Berry phase.

The valence and conduction bands at the K^+ and K^- valleys are partially composed of d atomic orbitals. Due to the broken inversion symmetry, the energy bands develop a spin-splitting, and because of the heavy transition metal d orbitals (compared to that of carbon atoms) the spin-orbit coupling is strong compared to that of graphene [14, 15]. The spin-orbit splitting in the valence band is around 200 meV in Mo-based TMDCs, and 400 meV in W-based TMDCs. The splitting in the conduction band is smaller, a few tens of meV [16].

Another consequence of the broken inversion symmetry is the Berry phase. Berry showed that when an eigenstate slowly moves in a closed loop through a vector field, the eigenstate will return to the initial state but will acquire a phase [17, 18]. The acquired phase is called the Berry phase, and the curl of the vector field is called the Berry curvature. In the context of monolayer semiconductors, the K^+ and K^- valleys have opposite signs of Berry curvature. When Bloch electrons move in a closed loop around the K^+ and K^- valley band extrema, they acquire a Berry phase that is equal and opposite between the valleys [15, 19]. Schematic drawing of the Berry curvature for each valley is shown in Figure 5. The Berry curvature results in a valley orbital magnetic momentum, which leads to valley-dependent optical selection rules (see discussion in Sec. 2.1.6).

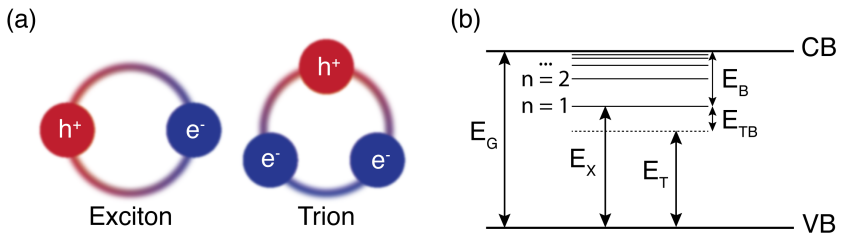

Fig. 6. Excitons and trions in monolayer TMDCs. (a) Schematic drawing of an exciton and a negatively charged trion. (b) Simplified energy diagram of the conduction band (CB), valence band (VB), monolayer band gap (E_G), exciton energy (E_X), trion energy (E_T), exciton binding energy (E_B), and trion binding energy (E_{TB}).

These valley properties can give rise to interesting phenomena, such as valley Zeeman and Hall effects [20], and can provide an extra degree of freedom for applications in Quantum information storage and processing.

2.1.4. Basics of excitons

A semiconductor at absolute zero temperature has a valence band filled with electrons and an empty conduction band. At finite temperatures, there is a probability of holes occupying the valence band and electrons occupying the conduction band, which is determined by the carrier density of states and the Fermi-Dirac distribution function. External sources, such as electromagnetic waves or electric fields, can further excite electrons into the conduction band, leaving a hole in the valence band. The electrons and holes can form a bound quasi-particle called excitons (Figure 6(a)), which is analogous to a hydrogen atom, where an electron is bound to a proton. Unlike hydrogen atoms however, excitons in semiconductors (also known as Wannier excitons) have a larger Bohr radius spanning multiple lattice sites, and a smaller binding energy. This is due to the small effective mass of electrons compared to that of holes and the presence of dielectric screening in semiconductors. Excitons can recombine to emit light and thus are a key component in studying light-matter interaction in TMDCs. Some of the beneficial properties of excitons will be discussed further in the following sections.

The interaction of electron and holes has important consequences for optical and electronic properties in the material. The free particle band gap is determined by the Bloch wave approximation and corresponds to the energy in which the electrons and holes are in a continuum state. Compared to the free particle band gap (E_G), exciton energy (E_X) is lower because it is a bound state. The exciton binding energy (E_B) is defined as the energy required to disassociate the electrons from the holes, and can be used to express the exciton energy:

$$E_X = E_G - E_B. \tag{3}$$

The exciton energy is also referred to as the optical band gap. The optical band gap is the lowest-energy state ($n = 1$) of the exciton. The energy diagram of the exciton energies are drawn in Figure 6(b).

The lowest-energy exciton is called the 1s exciton, whose wavefunction of the relative motion of electron and hole is analogous to the 1s state of a hydrogen atom. Excited states of exciton mimic the Rydberg serious of the hydrogen atom. In addition, when there is a finite electron or hole population in the conduction or valence band, the exciton may interact with the electron or hole gas collectively and form two polarons [21, 22], one at a slightly higher energy than

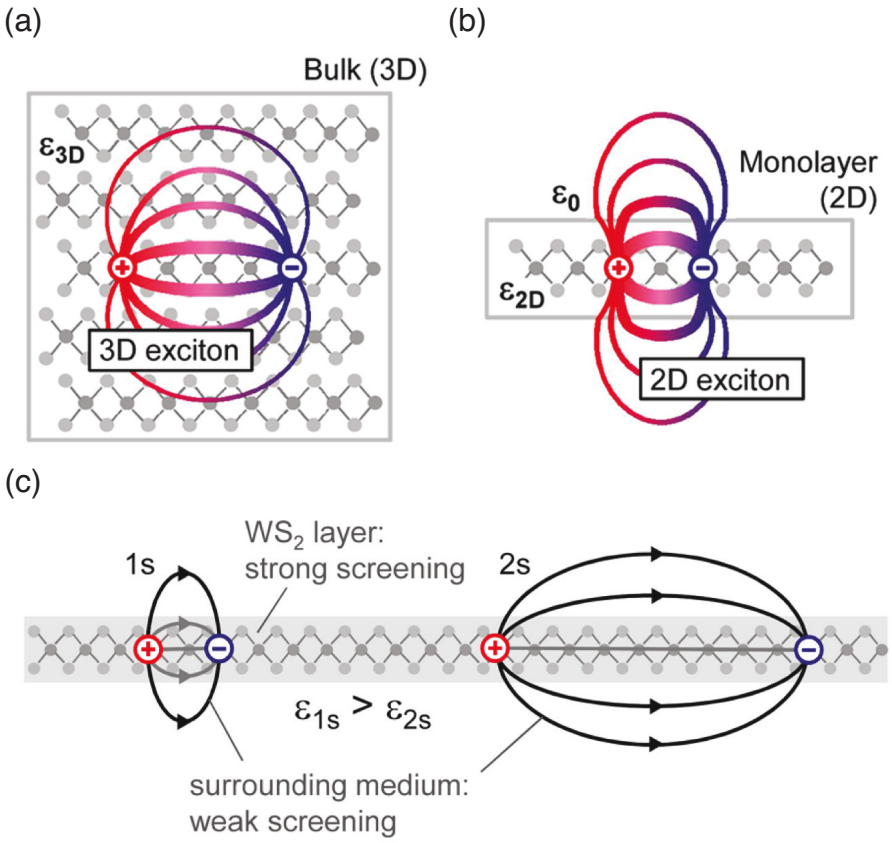

Fig. 7. Dielectric screening of excitons in monolayers. (a-b) Schematic drawing of the exciton dielectric screening in (a) 3D and (b) 2D. (c) Schematic drawing of 1s and 2s excitons in non-uniform dielectric environment. Reprinted with permission from [A. Chernikov, T. C. Berkelbach, H. M. Hill, A. Rigosi, Y. Li, O. B. Aslan, D. R. Reichman, M. S. Hybertsen, and T. F. Heinz, Phys. Rev. Lett., 113, 076802, 2014] [30]. Copyright 2014 by the American Physical Society.

the neutral exciton, one at a lower energy. The latter is often modeled as a trion (Figure 6(b)) and the difference between the exciton and trion energy is the trion binding energy (E_{TB}). In traditional 3D semiconductors, E_{TB} is typically on the order of 1 meV [23]. In comparison, the trion binding energy (E_{TB}) in TMDCs is about 30 meV and observable even up to room temperature [24, 25]. Both excited state excitons and trions interact with each other more strongly and respond to external field more strongly compared to the tightly bound neutral excitons, making them potentially interesting for studying nonlinear exciton and polariton physics [26–28]. But the stronger nonlinearity come at the expense of weaker binding and weaker oscillator strength. In this review, we focus on the charge neutral 1s excitons unless specified otherwise.

2.1.5. Binding energy

The stability of the exciton is largely determined by its binding energy, which also has important implications for light emission as we will discuss later. Excitons in TMDC monolayers have large binding energies on the order of 500 meV [29], two orders of magnitude greater than that of GaAs. This is due to a large reduced mass, reduced dielectric screening, and small electron-hole separation resulting from the decrease in dimensionality going from 3D to 2D. A schematic

drawing of the dielectric screening in 3D versus 2D is shown in Figure 7(a), 7(b). The monolayer exciton binding energy is larger than the room temperature thermal energy (≈ 25 meV), which makes monolayer excitons stable at room temperature, allowing room temperature photonic and optoelectronic devices.

To calculate the exciton binding energy, we start from the Wannier equation, which is a two-particle Schödinger equation that describes an electron in the conduction band and a hole in the valence band interacting via an attractive Coulomb potential [31]:

$$-\left[\frac{\hbar^2\nabla^2}{2\mu} + V(r)\right]\psi_\nu(r) = E_\nu\psi_\nu(r). \tag{4}$$

μ is the reduced mass of the exciton:

$$\mu = \frac{m_e m_h}{m_e + m_h}, \tag{5}$$

where m_e is the electron effective mass and m_h is the hole effective mass. $V(r)$ is the Coulomb potential:

$$V(r) = \frac{e^2}{4\pi\epsilon_r\epsilon_0 r}, \tag{6}$$

where e is the elementary charge, ϵ_r is the relative permittivity, and ϵ_0 is the vacuum permittivity.

The Wannier equation is analogous to the Schrödinger equation for an hydrogen atom. It turns out, going from 3D to 2D, the n quantum number goes from $n \to (n-1/2)$ [31–33]. This change manifests itself during the change of coordinates from spherical (3D) to polar (2D). The detailed analytical derivation can be found in Ref [34]. Solving the Wannier equation in 2D (using the 2D Laplace operator in polar coordinates) we obtain the eigen-energy:

$$E_B^n = \frac{\mu e^4}{2\hbar^2\epsilon_{\text{eff}}^2\,(n-1/2)^2}, \text{ with } n = 1, 2, 3, \cdots, \tag{7}$$

where ϵ_{eff} is the effective dielectric screening from the environment. Experimental measurements and theoretical studies of 2D excitons in monolayer TMDCs have shown deviation from this simplified model [30, 35–37]. This is due to the nonuniform dielectric environment experienced by the exciton in 2D materials [38]. Qualitatively, this is due to the different levels of dielectric screening experienced by the electric field lines between electrons and holes. The electric field lines experience a larger screening when going through the 2D material than when going through the surrounding medium as shown in Figure 7(c). For higher order excitons (higher quantum number n), the separation between electron and hole becomes larger, fewer electric field lines go through the 2D material, and thus the screening is reduced. This can be modeled as the Rytova-Keldysh potential [39, 40]:

$$V_{eh}(r) = -\frac{\pi e^2}{2r_0}\left[H_0\left(\frac{r}{r_0}\right) - Y_0\left(\frac{r}{r_0}\right)\right], \tag{8}$$

where H_0 and Y_0 are Struve and Bessel functions and r_0 is the effective screening length.

Because of the 2D nature of monolayer TMDCs, the substrate or capping material can increase the dielectric screening and reduce the exciton binding energy. However, the additional dielectric screening also renormalizes and reduces the free particle band gap [41]. This combined with the reduced binding energy results in minimal changes to the exciton ground state energy.

The strong binding energy of monolayer TMDC excitons offer benefits for the study of light-matter interactions. First, the large binding energy results in room-temperature stable excitons. Next, the higher order exciton states ($n = 2, 3, \cdots$) are experimentally observable [30] and have been used to demonstrate exciton-polaritons with higher interaction strength [42]. Lastly, the excitons interact strongly with light, which we will discuss further in the next section.

2.1.6. Optical selection rules and spin valley locking

Excitons are optically active if they can couple with light. They are generically called "bright excitons". The exciton-photon coupling require conservation of both the linear and angular momentum. The conservation of the linear momentum requires the exciton center-of-mass wave vector $\boldsymbol{k}$ to be equal to the in-plane projection of the photon wave vector $\boldsymbol{q}_{\parallel}$ [29]. Thus, the allowed wave vectors are $k < q_0 = \omega/c$, where ω is the photon frequency corresponding to the exciton resonance. In other words, the excitons that are within the "light cone" are bright excitons and couple to light by absorption or emission, while excitons outside of the light cone are "dark excitons" and are optically inactive. A schematic illustration of such dark and bright exciton formation is shown in Figure 8.

The total angular momentum has contributions from both the spin angular momentum and orbital angular momentum. In the absence of magnetic field or magnetic scattering, the allowed optical transitions are between the same spin states in the valence and conduction bands. In TMDC, it results in two bright excitons called the A exciton (lower energy) and the B exciton (higher energy) as represented in Figure 8(b). They are also called spin-singlet excitons, as the electron and hole have parallel spins. Transition between valence and conduction bands of opposite spins lead to spin-triplet excitons, where the electron and hole has anti-parallel spins; they form another type of dark exciton. In tungsten-based TMDCs, namely WS_2 and WSe_2 [43], these dark excitons are the lowest energy exciton state. Consequently, the dark states reduces the emission of WS_2 and WSe_2 at low temperature [44].

In addition to conservation of spin, the orbital and valley angular momentum need to be conserved. Since both the conduction and the valence band electrons have d orbitals, opposite helicities of circularly polarized light couple to the valleys K^+ (σ^+ polarization) and K^- (σ^- polarization) valleys, respectively (Figure 8(b) and 8(c)). The spin-valley locking property of TMDCs is thus transcribed to the valley selection rule of the optical transitions.

2.1.7. Oscillator strength and linewidth

For optically active excitons, the radiative decay rate can be obtained using the Fermi's golden rule [45]:

$$\Gamma_0 \sim |\langle f|\boldsymbol{e}\cdot\boldsymbol{r}|i\rangle|^2 \, \rho_{c,v}(\omega) \, \delta(E_c - E_v - \hbar\omega), \tag{9}$$

where f and i are final and initial states, $\rho_{c,v}(\omega)$ is the density of states, E_c and E_v are final and initial state energies, respectively, and $\hbar\omega$ is the energy of the electromagnetic field.

The strong binding energy of TMDC excitons leads to a small spatial separation of electrons and holes, and thus a larger wave function overlap. As a result, the excitons have a large oscillator strength and interact strongly with light. The exciton oscillator strength is a dimensionless quantity that quantifies the interaction between the exciton and electromagnetic waves. It can be derived from the interband optical transition matrix and is defined as follows [46]:

$$f = \frac{2\mu\omega}{\hbar} |\langle u_v|\boldsymbol{r}\cdot\boldsymbol{e}|u_c\rangle|^2 \frac{V}{\pi a_{B,2D}^3}, \tag{10}$$

where u_c and u_v are Bloch wave functions of electron and hole, respectively, ω is the frequency of the transition, V is the exciton quantization volume, and $a_{B,2D}$ is the Bohr radius in 2D. To determine the Bohr radius in 2D, we first consider the general form of the exciton radius in 3D:

$$r_{X,3D} = n a_{B,3D}, \text{ with } n = 1, 2, 3, \cdots. \tag{11}$$

Here, $a_{B,3D}$ is the exciton Bohr radius in 3D. The Bohr radius in 2D (where $n = 1$) is therefore:

$$a_{B,2D} = \frac{1}{2} a_{B,3D} = \frac{\epsilon_r \epsilon_0 \hbar^2}{2\mu e^2}. \tag{12}$$

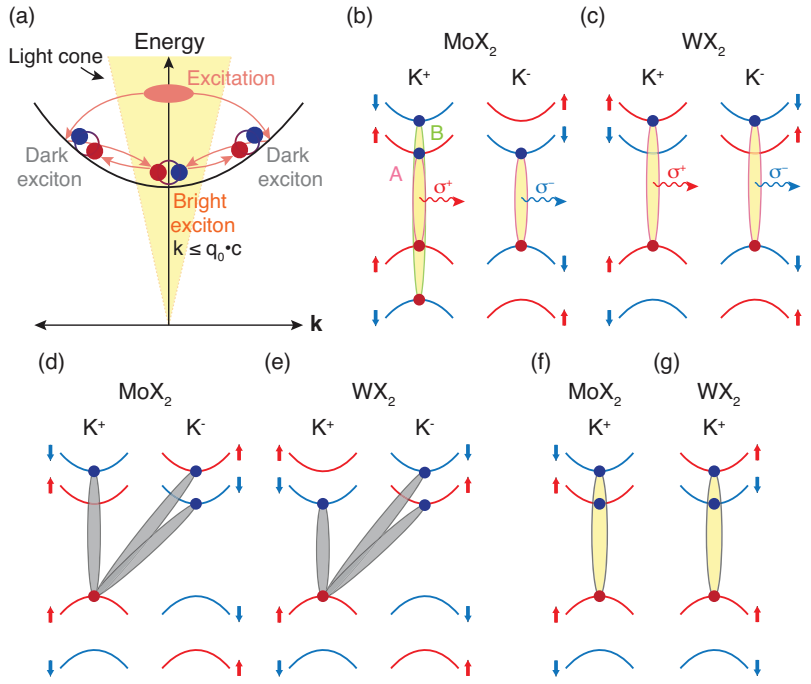

Fig. 8. Exciton formation and emission. (a) Schematic diagram of the exciton formation dynamics in the two-particle representation. The light cone is colored in yellow. Excitons inside of the light cone are bright excitons and excitons outside of the light cone are dark excitons. Excitons are created by excitation of carriers and subsequent relaxation to the ground state. Dark excitons can scatter into the light cone via phonon scattering and at finite temperatures bright excitons can scatter outside of the light cone. (b-c) Spin-valley band configurations and optical transitions for bright excitons in (b) Molybdenum-based, and (c) Tungsten-based monolayers. A and B represent the A-exciton and B-exciton transitions, respectively. Spin up and spin down states are represented in red and blue, respectively. (d-e) Dark exciton formation in (d) Molybdenum-based and (e) Tungsten-based monolayers. (f-g) Inter-valley bright trion formation for (f) Molybdenum-based and (g) Tungsten-based monolayers.

Hence, in 2D the exciton binding energy is 4 times larger and the Bohr radius is 2 times smaller than in 3D. Using a simplified picture, this is due the the exciton being confined to a 2D plane and being 'squeezed' together. In TMDCs, the exciton Bohr radius for the 1s state is on the order of 1 nm [47].

The exciton linewidth gives some information about the dynamics of the excited state population and how it interacts with light. Theoretical studies predict the radiative lifetime of 1s excitons in TMDCs to be on the order of 1 ps, which corresponds to a radiative linewidth of 1 meV [48, 49], about two orders of magnitude smaller than that of GaAs [50]. The radiative lifetime sets a lower bound for the linewidth. In real systems, defects, inhomogeneity, and impurities may lead to inhomogeneous broadening of the linewidth (Figure 9(a)), while fluctuations in the environment and scattering with phonon and carriers often result in additional homogeneous broadening.

Decreasing the exciton linewidth is important for thermalization of excitons and exciton-polaritons. In TMDCs, the best way to reduce the linewidth is by encapsulating the monolayer with hBN [52–54]. Capping the monolayers with hBN can ensure the surface roughness of the substrate does not transfer to the monolayer, and can also protect the exciton from charge transfers or local electric fields, thus reducing the inhomogeneous broadening of the linewidth.

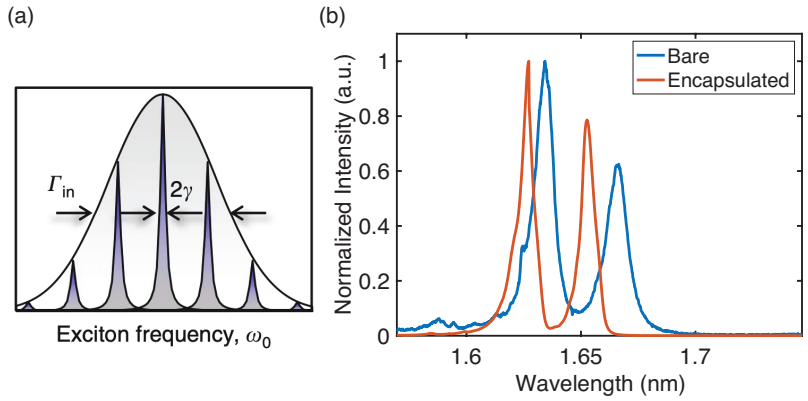

Fig. 9. Exciton linewidth in TMDCs. (a) Schematic representation of inhomogeneous linewidth broadening. Individual oscillators with linewidth 2γ have different frequencies due to the environmental variations. This results in an inhomogeneously broadened total linewidth (Γ_{in}). Figure reproduced with permission from [G. Moody, C. Kavir Dass, K. Hao, C.-H. Chen, L.-J. Li, A. Singh, K. Tran, G. Clark, X. Xu, G. Berghäuser, E. Malic, A. Knorr, and X. Li, Nat. Commun., 6, 8315, 2015] [51]. (b) Photoluminescence measurements of bare and encapsulated monolayer $MoSe_2$ at 5K.

Experimental studies show that hBN encapsulation results in linewidths as low as 2 meV [52]. Encapsulation also alters the dielectric environment experienced by the excitons and trions and can change their energies (Figure 9(b)).

2.2. Experimental studies of excitons in monolayer TMDCs

2.2.1. Monolayer TMDC sample preparation

Monolayer sample preparation techniques play an important role in making high quality samples that have strong emission and narrow linewidths. We review here three main types of methods to prepare monolayer TMDCs: exfoliation using polymers, exfoliation using metal tapes, and epitaxial growth or deposition.

First is mechanical exfoliation using polymers such as scotch tape or polydimethylsiloxane (PDMS) [1]. This method is readily implemented in typical lab environment and produces good quality samples, therefore is currently the most used method for making photonic devices. However, the typical dimension of the exfoliated flakes are on the order of 10s of μm, with low yield.

A general procedure for monolayer exfoliation is as follows: first a thin (sub-millimeter) flake of bulk crystal is exfoliated onto an adhesive tape, which is often referred to as 'mother tape'. Then, a sheet of polymer material, such as scotch tape, PDMS, or PVC tape, is brought in contact with the crystal on the mother tape and peeled off to cleave the crystal and transfer some layers onto the polymer sheet. To further thin down the crystal, a fresh sheet of polymer is pressed onto the existing one and peeled off. This process is repeated until optimal thickness is achieved. Next, the polymer sheet is pressed onto a clean substrate, usually a silicon dioxide (SiO_2) wafer, and peeled off to exfoliate some of the flakes onto the substrate. To locate the monolayers, the substrate is searched under an optical microscope and monolayers are identified by its optical contrast. On average, this method produces flakes that are on the order of 20×20 microns, which is sufficient for most optical characterization measurements.

Exciton optical characterization measurements or exciton-polariton devices benefit from exciton emission with narrow linewidths and high quantum field. To that end, different methods

to passivate and encapsulate the monolayers have been investigated with varying degrees of effectiveness. The most effectively and widely applicable method is to encapsulate the monolayer with hexagonal boron nitride (hBN). hBN has a flat 2D hexagonal lattice structure that provides a smooth, uniform surface for the TMDC material. Encapsulation also protects the TMDC material against degradation and reduces the charge fluctuation in the material and lowers the inhomogeneous broadening [52, 54]. Exfoliating hBN layers is very similar to exfoliating monolayer TMDCs, except that hBN can be a few to few-tens of layers thick. To encapsulate the monolayer TMDC with hBN using a dry transfer technique, a transfer stamp, usually comprised of a glass slide with a small piece of polymer, is used to pick up the top hBN layer, the TMDC layer, and the bottom hBN layer. The encapsulated sample stack is then transferred onto a desired target substrate and any residual polymer on the sample is washed away with a solvent. This method can produce samples with the highest optical quality at present.

The second method to produce monolayers is metal-assisted exfoliation. It can produce larger area monolayer flakes up to the centimeter scale and is a promising avenue for scalable 2D material devices [55–58]. However, removing of the gold from the 2D material results in degraded optical qualities. Recently, it was shown that, after removing gold, encapsulating the large area monolayer with 1-dodecanol molecules results in drastically improved optical qualities with defect states that are strongly suppressed [59]. The exciton and trion linewidths and photoluminescence quantum yield are comparable to that of hBN-encapsulated, tape-exfoliated small flakes and are highly uniform across multiple millimeters. Such dodecanol-encapsulated large-area monolayers can facilitate integration of TMDC monolayers with photonic structures and systematic development of TMDC photonic devices.

Lastly, large-area growth of monolayers uses techniques such as chemical vapor deposition (CVD) [60–65], molecular beam epitaxy (MBE) [66, 67], or atomic layer deposition (ALD) [68]. The optical quality of the epitaxial monolayers has been greatly improved over the past decade and has become competitive with exfoliated monolayers at room temperature. However defect densities in large-area monolayers are still much higher than the state-of-the-art bulk crystals or exfoliated monolayers, resulting in typically worse exciton linewidth and quantum yield at low temperatures. Further development of these methods will be crucial for 2D material based technologies.

2.2.2. Optical spectroscopy techniques

The strong binding energy of TMDC excitons leads to a small spatial separation of electrons and holes and thus a larger wave function overlap. As a result, the excitons have a large oscillator strength and a strong interaction with light. They often feature much stronger linear and nonlinear optical responses than those of typical semiconductors, when permitted by crystal symmetries. Therefore, optical spectroscopy is especially useful and versatile for the study of TMDC materials. We will focus on linear spectroscopy in this review, which has been well established and widely used to characterize fundamental properties of excitons. Nonlinear spectroscopy using ultrafast lasers has been used to study valley and carrier dynamics and nonlinear optical phenomena that are hard to access in conventional materials and in the linear regime. Furthermore, TMDCs can exhibit nonlinear characteristics when interacting with ultrafast pulses, and can serve as a basis for nonlinear photonics. This is a fast evolving and exciting topic that we refer the readers to a few recent reviews on the subject [69–74].

Identification of monolayers There are few different ways of identifying monolayer TMDCs. The fastest way is to search the exfoliated use an optical microscope to distinguish the monolayer among multilayers through optical contrast. Another way to determine monolayers is through reflection contrast and photoluminescence (PL) measurements. Monolayer excitons have a direct bandgap and a strong oscillator strength thus a strong absorption and emission at the exciton

resonance energy that can be seen through reflection and PL measurements. Raman spectroscopy is another method that can be used to determine the number of TMDC layers. There are two Raman active modes that can be measured via spectroscopy: A_{1g} and E^1_{2g}. A_{1g} corresponds to the out-of-plane vibrations of the two chalcogen atoms in opposite directions. E^1_{2g} corresponds to the in-plane vibrations of the chalcogen atoms with respect to the transition metal atom [75]. The energies, intensities and the lineshapes of the Raman peaks are sensitive to the layer numbers and can therefore be used to identify monolayers.

Exciton measurements The lowest energy exciton optical transition ($n = 1$) can be directly measured by linear reflectance contrast, PL, and photoluminescence excitation (PLE) measurements. The large binding energy of excitons results in room-temperature stable excitons and experimentally observable higher order ($n = 2, 3, \cdots$) exciton states [30]. In monolayer TMDCs, there are both bright and dark excitons. The optical transition between the same spin states in the valence and conduction bands results in the formation of two bright excitons called the A exciton (lower energy) and B exciton (higher energy). Furthermore, dark exciton is the lowest energy state in tungsten-based TMDCs, namely WS_2 and WSe_2 [43], leading to reduced emission at low temperature [44].

Linewidth measurements The exciton linewidth gives some information about the dynamics of the excited state population and how it interacts with light. In TMDCs, the radiative lifetime of the 1s exciton is predicted to be on the order of 1 ps (or 1 meV) [48, 49].

In real materials, the linewidth is often dominated by various inhomogeneous broadening and additional dephasing mechanisms due to defects, inhomogeneity, environmental fluctuations, and scattering. Therefore, special experimental techniques, such as 2D Fourier transform spectroscopy [51, 76], mid-infrared absorption spectroscopy [77], and high-resolution time-resolved spectroscopy [78] are required to extract the radiative lifetime. Notably, it is remarkable that the exciton linewidth in high-quality TMDC monolayers can be comparable or of the same order of magnitude as the radiative linewidth. This is unique among semiconductor excitons of greater than zero-dimension. In such monolayers, light-matter interactions approach the coherent limit; even a monolayer can function as a high-reflectance mirror [79, 80] or a perfect absorber [81].

2.3. Excitons in multi-layer crystals and heterostructures

2D materials offer a platform that allows the creation of heterostructures with a variety of functions. In this section, we focus on the spectroscopic experiments of TMDCs heterobilayers. In the first part, the interlayer exciton state as a novel state in heterobilayers will be reviewed. We will discuss band alignment, lifetime, oscillator strength, electric dipole momentum, magnetic dipole momentum, valleytronics, and optical selection rules. The above features of interlayer excitons can be explained without the consideration of moiré lattices. In the second part, we will summarize the evidence of moiré excitons, such as the splitted exciton species, moiré assisted electronic band hybridization, and moiré-manipulated optical selection rules. Other observations such as moiré twist angle dependence of exciton lifetime and diffusion length can also provide additional evidence of the moiré superlattice. These phenomena can be understood in a single particle picture considering the moiré superlattice, and the moiré manybody physics is reviewed in the next section.

2.3.1. Interlayer excitons

A beneficial property of TMDCs is the ability to form heterostructures without lattice matching constraints. Unlike 3D materials, 2D materials do not have dangling bonds, which means they can

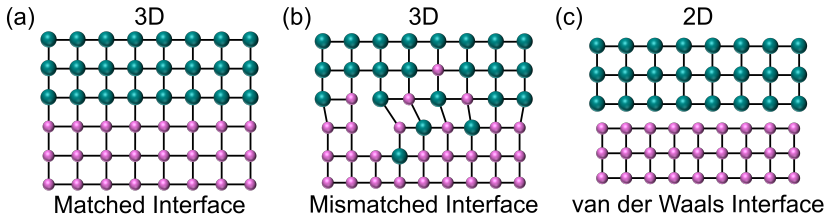

Fig. 10. Heterostructure lattice matching. Schematic drawing of a 3D (a) lattice matched and (b) lattice mismatched heterostructure interface. The lattice mismatch induces strain and defects along the boundary. (c) 2D heterostructure interface. The layers are bound together by vdW forces.

be integrated with other materials without inducing strain or defects at the boundary (Figure 10). Furthermore, there is a wide variety of 2D materials with different band gaps and work functions that can be used for heterostructure engineering, allowing a greater degree of flexibility than 3D bulk semiconductors.

When two different semiconductor materials are combined to form a heterostructure, an electron in one layer and a hole in another can be bound to form an interlayer exciton. The electron and hole wave functions in interlayer excitons are spatially separated, whereas in intralayer excitons they are closer together. Therefore, interlayer excitons are also known as spatially indirect excitons, and they have been first reported in GaAs/AlGaAs coupled quantum wells to use as electro-optical modulators [82].

In 2D materials, interlayer excitons in both homo- and heterobilayers feature a strong binding energy compared to 3D semiconductors, making them useful for high-temperature applications. The spatial separation of electron and holes result in a long radiative lifetime, a long valley depolarization time, and a permanent out-of-plane dipole moment with strong dipole-dipole interactions. Such spatially indirect excitons can exhibit a variety of physical phenomena including quantum-confined Stark effect [83–86], exciton condensation and superfluidity [7, 87–91], and strongly-correlated electronic states [92–94].

Interlayer excitons have been demonstrated in a wide range of TMDCs materials, including $MoSe_2$ [95], WSe_2 [86], and MoS_2 [96–99] homobilayers, and $MoSe_2/WSe_2$ [6, 100–104], MoS_2/WS_2 [105, 106], MoS_2/WSe_2 [107, 108], and WS_2/WSe_2 [109] heterobilayers.

In general, interlayer excitons in TMDC heterobilayers have a smaller oscillator strength compared to the intralayer excitons in monolayers and therefore weakly interact with light. However, there are hybrid inter/intralayer exciton states [110, 111] and homobilayer excitons [96–99] that maintain a sufficiently high oscillator strength for cavity coupling. This will be further explored in section 4.3.

Band alignment Stacking two monolayer TMDCs will result in a heterobilayer, and the band edge alignment is generally in a staggered form, which implies a type II heterostructure. A simplified diagram of the interlayer exciton formation and the $WSe_2/MoSe_2$ band energy diagram is shown in Figure 11. The conduction band minimum and valence band maximum comes from two different layers, which is confirmed by photoelectron spectroscopy and first principle calculations. Therefore, optically or electrically injected electrons and holes will relax to two separate layers and form a new bound state, called interlayer exciton. The first experimental evidence of interlayer exciton is reported in a $WSe_2/MoSe_2$ by PL spectrum [100]. PL from bilayers replicates the main features of the constituent monolayers including the neutral excitons and trions, but with a highly reduced intensity. Besides, a new emerging peak was observed at the

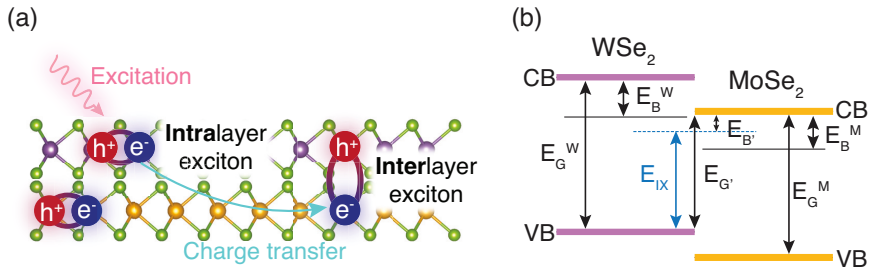

Fig. 11. Interlayer exciton schematic. (a) Schematic illustration of the intralayer and interlayer exciton formation. Intralayer excitons are created by external excitation of charges. Charge transfer of carriers between layers created spatially separated interlayer excitons. (b) Type II band alignment of a $WSe_2/MoSe_2$ heterobilayer. E_G^W (E_G^M) is the band gap energy of WSe_2 ($MoSe_2$). E_B^W (E_B^M) is the binding energy of WSe_2 ($MoSe_2$) intralayer exciton. $E_{G'}$ is the interlayer band gap energy, $E_{B'}$ in the interlayer exciton binding energy, and E_{IX} is the interlayer exciton energy (Note: this is a simplified picture that ignores the twist angle between layers). Figure made with data presented in [112].

longer wavelength, which is assigned to be the emission from the interlayer exciton. The origin of interlayer exciton is further confirmed by the PL excitation spectra. The interlayer exciton emission intensity is enhanced when the excitation laser frequency is on resonance with the intralayer excitons. Up to now, interlayer excitons have been reported in different heterobilayers. Among them, interlayer exciton energy of $WSe_2/MoSe_2$, $WS_2/MoSe_2$, WSe_2/MoS_2, and $MoSe_2/MoS_2$ is well separated from that of the corresponding intralayer excitons, and can be easily identified from the PL spectrum. In $WS_2/MoSe_2$ and WS_2/MoS_2, the interlayer exciton and intralayer exciton are almost degenerate, and the coupling between intralayer and interlayer excitons needs to be considered.

Ultrafast interlayer charge transfer Considering a type II heterobilayer optically pumped at a frequency above intralayer exciton energy, optically excited carriers will quickly separate into electrons in one layer and holes in the other layer. Such an interlayer charge transfer process is extremely fast in heterobilayers, which can happen at a femtosecond (fs) timescale. This ultrafast process was first identified in a WS_2/MoS_2 heterobilayer. After optically exciting MoS_2 intralayer excitons in a MoS_2/WS_2 heterobilayer, the hole was observed to transfer from the MoS_2 layer to the WS_2 layer within 50 fs [113]. Similar ultrafast charge transfer process has also been observed in the other heterobilayers, and is found to be twist angle independent. A number of studies have been carried out to understand the mechanism behind the ultrafast process and its twist angle independence, which are summarized in a review [114]. The key reason for the ultrafast charge transfer is that the small layer separation of around 1 nm leads to interlayer exciton state with strong coulomb interaction. Therefore, these energetically more favorable interlayer exciton state will be occupied by the optically excited electron hole pairs in a very short time scale. The twist angle independence is explained by the assistance of phonon scattering process and strong interlayer hybridization via Γ and Q valleys.

Electrical dipole momentum The interlayer exciton has two different kinds of dipole moments. The first kind corresponds to the optical transition between the vacuum state and the exciton state, which determines oscillator strength. The second kind is the static electric dipole. We will briefly discuss them separately as follows.

As a result of the spatial separation of the electron and hole, the oscillator strength of interlayer exciton is smaller than that of intralayer exciton by 2-3 orders of magnitude. This contrast is confirmed by three different types of measurements. The PL lifetime of intralayer and interlayer exciton is typically ps and ns, respectively. Remarkably, the longest reported interlayer exciton PL lifetime is around μs [115]. Photocurrent spectroscopy measurements on an $MoSe_2/WSe_2$ p-n junction show ~200 times lower photocurrent generation from interlayer excitons than from intralayer excitons [116]. Optical absorption of interlayer excitons measured using electromodulation spectroscopy show the interlayer exciton intrinsic radiative lifetime to be 0.4 ns [117].

The static electric dipole is along the out of plane direction, and proportional to the layer separation d. By applying the electric field along the out of plane direction, interactions between the electric dipole and the electric field will induce the shift of the exciton resonance, which is called D.C. Stark effect. This Stark effect of interlayer excitons has been observed in different types of heterobilayers [6, 83]. By fitting the field dependence of the energy shift, the dipole momentum can be extracted, which has dependence on the interlayer separation. This static dipole momentum can also leads strong dipole-dipole interaction, manifested as a strong blueshift of the interlayer exciton resonances with increasing densities.

Magnetic dipole momentum The influence of the magnetic field on the exciton can be expressed as: $\Delta E_X = \Delta E^c - \Delta E^v - \Delta E_X^b$, where ΔE_c, ΔE_v, and ΔE_X^b are the Zeeman shifts of the conduction band extrema, valence band extrema, and the binding energies, respectively. In TMDCs systems, the exciton binding energy acquires negligible diamagnetic shift when the magnetic field is under 10 T. Therefore, the magnetic response is simplified to be $\Delta E_X = \Delta E^c - \Delta E^v = -(\mu^c - \mu^v)B$, where μ^c and μ^v are the magnetic moments of the conduction and valence bands. μ^c and μ^v are further contributed by three parts: spin, orbital, and valley angular momentum. For bright intralayer exciton of monolayer TMDCs, the contribution from spin is cancelled because of the parallel spin of electrons and holes. The contribution from the valley orbital number is negligible [118]. The orbital angular momentum for the valence and the conduction band are $2\hbar$ and 0, respectively. For the K valley, the Zeeman shift of the neutral exciton energy depends only on magnetic moments of the orbital angular momentum, which is $(\mu^v - \mu^c) = -2\mu_B$.

In heterobilayers, the magnetic response of the interlayer exciton depends on the total angular momentum engineered by the stacking orders and relaxed optical selectivity. In contrast with intralayer exciton in monolayers, spin non-conserved optical transition of interlayer exciton is allowed in heterobilayers as a result of the broken out-of-plane mirror symmetry, corresponding to the spin triplet exciton. The spin conserved transition corresponds to the spin singlet exciton. Four cases need to be considered: spin singlet and triplet excitons in a heterobilayer with AA (twist angle close to 0°) and AB stacking orders (twist angle close to 60°). For a singlet exciton, the spin angular momentum contributed by electron and hole will cancel. For a triplet exciton, the total contribution of the spin will be μ_B. In a heterobilayer with AA stacking order, where the K valley of electron and hole is aligned, the contribution of valley angular momentum is negligibly small, similar with monolayer intralayer exciton. However, in the case of AB stacking order where K and K′ valley are aligned, the valley angular momentum of electron and hole will constructively contribute to the total angular momentum.

Optical selection rules Compared to intralayer excitons, the optical selection rule for interlayer exciton is more complex, as they also depend on the atomic registries in the bilayer and are affected by the breaking of plane mirror symmetry.

Unlike the monolayer excitons whose spin-conserved (spin flip) interband transitions can only couple to photons with in-plane (out-of-plane) polarization, such restriction is removed for the interlayer excitons due to the breaking of the out-of-plane mirror symmetry in the heterobilayers,

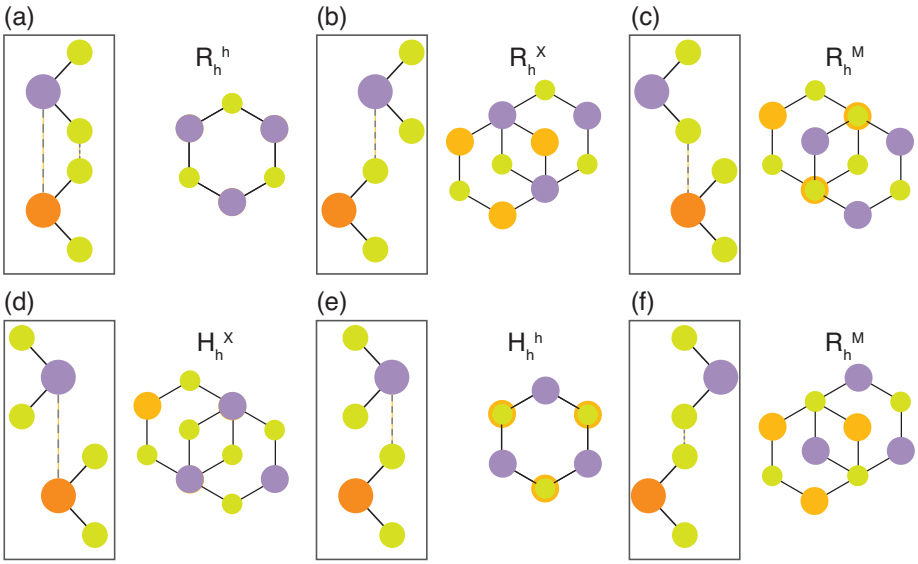

Fig. 12. Stacking order and atomic registries of heterobilayers. (a-c) Atomic registries of R-stacked heterobilayer. (d-f) Atomic registries of H-stacked heterobilayer. Both the side view (on left) and the top view (on right) are illustrated.

	R_h^h	R_h^X	R_h^M	H_h^X	H_h^h	H_h^M
$v,\uparrow \leftrightarrow c',\uparrow$	σ^+	σ^-	z	σ^+	σ^-	z
$v,\uparrow \leftrightarrow c',\downarrow$	z	σ^+	σ^-	z	σ^+	σ^-
$v,\downarrow \leftrightarrow c',\downarrow$	σ^+	σ^-	z	σ^+	σ^-	z
$v,\downarrow \leftrightarrow c',\uparrow$	σ^-	z	σ^+	σ^-	z	σ^+

Table 1. The inter-valley optical selection rules between the valence band of one layer and the conduction band of another layer. Made with data presented in [119].

both the spin singlet exciton and spin triplet interlayer exciton can couple to photon with in-plane polarization. This has been verified in a $WSe_2/MoSe_2$ heterobilayer, where the PL emission from both the spin singlet and triplet exciton are observed. Moreover, the singlet and triplet exciton from the same valley will couple to photon with different circular polarization, also in agreement with experiments [102, 119, 120].

The heterobilayer also allow engineering of the atom registry alignment, which modifies the optical selection rule via the phase factors of the Bloch wavefunction. Theoretically, one-to-one correspondence between the interlayer atomic registry and the optical transition dipole can be established. Therefore, to determine the optical selection rule of an interlayer transition, both the atom registry and the spin configurations need to be considered, as summarized in Figure 12 [119]. The light polarization that corresponds to the inter-valley optical transition at each atomic registry is summarized in Table 1 [119].

In CVD-grown heterobilayers, due to the small difference in the lattice constants of WSe_2 and $MoSe_2$ monolayers, lattice relaxation leads to precise R- or H-stacking [121]. Opposite optical helicities were measured between interlayer excitons of such R-stacked and H-stacked bilayers, as predicted by theory. However, the larger inhomogeneous linewidth prevented differentiation

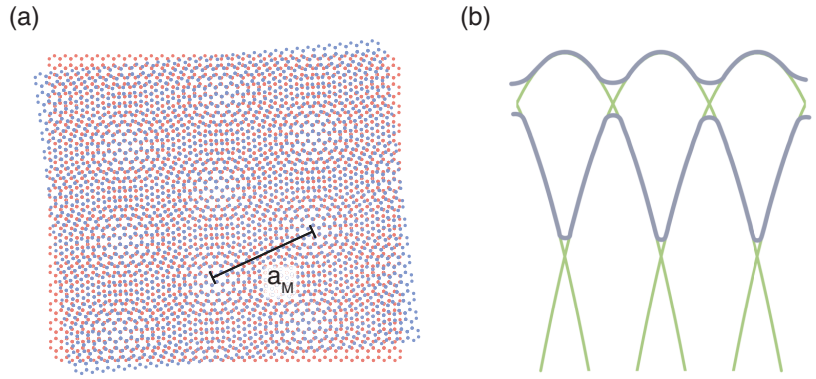

Fig. 13. Moiré superlattice. (a) Diagram of a moiré superlattice pattern. a_M is the superlattice constant. (b) Schematic of the monolayer TMDC bands folded due to the superlattice potential. The green lines represent the monolayer band dispersion and the gray lines represent the new folded mini bands. Reprinted from [E. C. Regan, D. Wang, E. Y. Paik, Y. Zeng, L. Zhang, J. Zhu, A. H. MacDonald, H. Deng, and F. Wang, Nat. Rev. Mater., 2022] [122].

between exciton and trion transitions. In $WSe_2/MoSe_2$ heterobilayers made of twist-aligned, exfoliated monolayers with R-stacked atomic registries [102], exciton and trion of the opposite helicities were measured, again in full agreement with the theoretical prediction.

Valleytronics of interlayer exciton The valley degree of freedom of intralayer excitons can be transferred to the interlayer exciton by aligning the two constituent monolayers [101]. Interestingly, a much higher degree of valley polarization can be preserved for interlayer excitons in heterobilayers, with a much longer valley-depolarization time [102]. This can be understood by considering two time scales. First, the optically injected intralayer exciton will be decomposed to electron and hole in the two layers, and this process can happen in fs scale, which is much faster than the valley depolarization rate of intralayer exciton (ps). Once the highly polarized interlayer excitons are formed, their depolarization rate is much slower than the monolayer intralayer exciton, because the valley depolarization, mainly induced by electron hole exchange interaction in monolayers, is highly suppressed in the heterobilayer as a result of spatial separation. Experimentally, the circular polarization degree of interlayer exciton of more than 80% was measured even in time-integrated PL spectra, with high-above resonance pumping. The valley polarization lifetime, measured from the polarization and time resolved PL spectra of interlayer exciton, is around tens nanoseconds, 3 orders of magnitude higher than that of the intralayer exciton [102].

2.3.2. Moiré excitons

In twisted TMDCs bilayers, moiré superlattices can be created through a small twist angle or lattice mismatch between the two constitute layers, providing a powerful method to engineer excitonic states in TMDCs (Figure 13(a)). The moiré lattice has a period many times of the monolayer crystal's lattice constant. Correspondingly, in momentum space, the crystal Brillouin zone folds into a much smaller one, as illustrated in Figure 13(b). The folded bands form mini bands with a smaller bandwidth, sometimes becoming nearly flat. Such tunable minibands provide an ideal platform for observing strongly correlated electronic states [123–128]. Moiré excitons can scatter resonantly with electrons or holes at certain filling factors, creating a 2D Feshbach molecule that can be tuned in and out of resonance with external electric field and

adding a layer of tunablity [129, 130].

Moiré induced split exciton levels and engineered optical selectivity Exciton in moiré lattices, called moiré excitons, can manifest as discrete exciton resonances or mini-bands, split from the monolayer exciton resonance, as a result of the moire lattice confinement [131, 132]. They may also manifest in special optical selection rules as they are distribute mainly at different locations in the moiré lattice with different atom registries [132–135].

Moiré induced band hybridization The above two features of moiré excitons were demonstrated in both interlayer and intralayer excitons. In a special combination $WS_2/MoSe_2$, the conduction bands of the two layers are almost aligned, and strong coupling between intralayer exciton and interlayer exciton is realized through the conduction band hybridization. The momentum-conservation of the hybridization is satisfied by the bandfolding induced by the moiré lattice, which is further confirmed by the twist angle dependence of the hybrid excitons [110]. Such phenomena have also been observed in the combination of WSe_2/WS_2 [136].

Twist angle dependence of moiré exciton dynamics Twist angle between two TMDCs layers, has become a new tuning knob to engineer exciton states. The twist angle dependence of moiré-exciton dynamics was experimentally studied, including PL lifetimes and diffusion length. In $WSe_2/MoSe_2$ hetrobilayers, the PL lifetime of moiré excitons was found to increase by one order of magnitude when the angle is increased from 1° to 3.5°. This is mainly due to the increased K valley misalignment between the two monolayers, and the electron hole recombination requires the phonon scattering. The twist angle dependence of interlayer exciton diffusion is also studied [109, 137, 138]: When the twist angle is small, the interlayer exciton is more likely localized within the moiré unite cell because of the larger moiré peirod and shorter interlayer exciton lifetime. With increasing the twist angle, the diffusion of interlayer exciton can be resolved with reduced moiré period and longer PL lifetime.

3. Collective phenomena of TMDC excitons

3.1. Exciton lasers in TMDCs

TMDC materials have a variety of exciton species and the freedom to integrate with a wide range of substrates, making them ideal for observing and controlling light-matter interactions and collective phenomena. They also offer new opportunities for compact and efficient optoelectronic and photonic devices.

The spatially indirect nature of interlayer excitons results in a strong dipole interaction and a long exciton lifetime, which can be beneficial properties for collective and controllable many-body phenomena [7, 139].

Interlayer excitons in $WSe_2/MoSe_2$ heterobilayers have been widely studied because of their strong PL emission. By integrating the heterobilayer with a photonic cavity, the interlayer exciton emission can be enhanced by the cavity feedback and, under the right conditions, lasing can occur. Figure 14(a) shows a schematic of a heterobilayer integrated with a photonic grating cavity. A direct band gap between the two monolayer materials can form when the layers are nearly commensurate with one another, and the interlayer excitons can have a sufficiently large oscillator strength for emission (Figure 14 (b)). With a type-II band alignment, the heterobilayer forms a three-level system that allows efficient pumping through the intralayer exciton resonances followed by rapid electron transfer to a lower-energy empty conduction band [141, 142] (Figure 14(c)). As a result, population inversion is readily achieved at the reduced bandgap while avoiding fast intralayer radiative loss of the carriers.

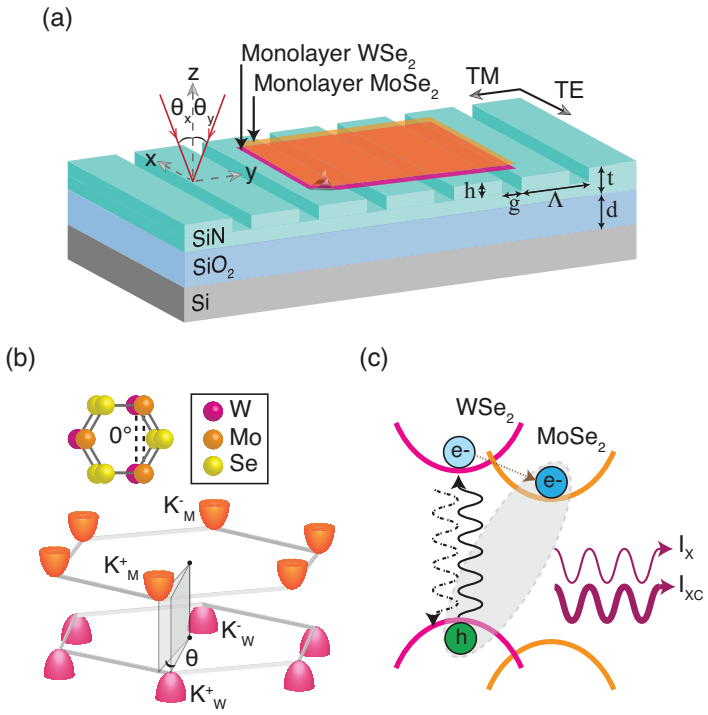

Fig. 14. Illustration of the heterobilayer/grating cavity laser system. (a) Schematic of the laser device consisting of a heterobilayer on a grating cavity. The along-bar (cross-bar) direction and polarization are defined as x (y) and TE (TM) respectively. Grating cavity design parameters are the following: total SiN thickness (t), SiO_2 thickness (d), grating thickness (h), grating period (Λ), gap width (g). We define θ_x (θ_y) as the azimuthal angle of the light beam along the x-z (y-z) plane with respect to the z-axis, as indicated by the red arrows. (b) Illustration of the rotationally aligned heterobilayer with twist angle $\theta = 0°$ (top), and the correspondingly direct band gap at the K valleys (bottom). (c) Band alignment and carrier dynamics of the heterobilayer. The heterobilayer has a type II band alignment, forming a three-level system for the injected carriers. Intralayer excitons are excited by a pump laser in the WSe_2 layer (solid wavy line). Some electrons transfer to the lower $MoSe_2$ conduction band on a fast (10 - 100 fs) time scale (dotted line), while others recombine as intralayer excitons with lifetimes of 1-10 ps (dash-dotted wavy line). Without the cavity, the interlayer excitons (dashed line) recombine with a lifetime on the order of 1 ns (I_X), and, with cavity enhancement, on the order of 100 ps (I_{XC}). Reprinted from [E. Y. Paik, L. Zhang, G. W. Burg, R. Gogna, E. Tutuc, and H. Deng, Nature, 576, 80–84, 2019] [140].

Lasing using interlayer excitons in TMDC heterobilayers has been demonstrated with a photonic crystal cavity at room temperature [143] and one dimensional (1D) grating resonator cavity with the formation of spatial coherence [140]. These studies set the stage for small-scale, energy-efficient, electrically injected, room-temperature semiconductor nanolasers that are easily integrable with existing silicon-based photonics.

3.2. Exciton condensation at high temperatures

Bose-Einstein condensation (BEC) of excitons is a macroscopic quantum phenomenon that attracts much interest in the condensed matter physics community [87, 144–146]. In three dimensions (3D), this is expected to happen when the exciton thermal de Broglie wavelength becomes comparable to the average inter-exciton separation; a macroscopic occupation of excitons in the ground state emerges below the condensation temperature. Such macroscopic occupation is, however, not possible in 2D [147–149]; the long-wavelength phase fluctuations in the exciton fluid destroy long-range phase coherence. Instead, it is expected that the system develops quasilong-range phase coherence and exciton superfluidity below the characteristic Berezinskii-Kosterlitz-Thouless (BKT) transition temperature [147–149], which is comparable but lower than the degeneracy temperature of the exciton fluid [7, 148, 150].

The emergence of atomically thin TMDC semiconductors that support tightly bound excitons [3, 29] provides an ideal avenue to explore the physics of exciton BEC in 2D [7, 8, 151–154]. Compared to double layers of semiconductor quantum wells and graphene [87, 90, 91, 155–157], the large exciton binding energy in TMDCs favors exciton BEC at much higher temperature scales [7, 8, 151–154]. As an estimate, the exciton degeneracy temperature in 2D is proportional to the exciton density and inversely proportional to the exciton mass. The maximum exciton density just before complete ionization of the excitons into an electron-hole plasma is $n_{max} \sim a_B^{-2} \propto E_B$ (a_B is the exciton Bohr radius); it implies a maximum degeneracy temperature on the order of the exciton binding energy $E_B \sim 300$ meV in monolayer TMDCs. Exciton BEC above room temperature is possible.

Unfortunately, the large binding energy in monolayer TMDCs also imply very strong light-matter interactions and therefore very short exciton lifetime [3, 29], which makes both the build up of a high exciton density and exciton thermalization difficult or impossible. To overcome this difficulty, theoretical studies have proposed the realization of exciton BEC in a dipolar interlayer exciton fluid [7, 8, 151–154, 158] (Figure 15(a)). Compared to intralayer excitons in monolayer TMDCs, the exciton binding energy is reduced because of interlayer electron-hole separation. The interlayer separation, however, endows excitons with negligible electron-hole wavefunction overlap and therefore much longer lifetimes [84, 159]. The compromise between binding energy and lifetime strikes a good balance and provides a realistic setting to stabilize exciton BEC in the 100 K (or higher) temperature scale [7, 8, 151–154] (Figure 15(c)). Moreover, the permanent dipole of interlayer excitons induces strong dipolar exciton-exciton interactions [8, 151]. The strong interaction further favors exciton BEC by suppressing both density and phase fluctuations [148, 149]; it can also stabilize other exotic ground states of excitons, such as exciton Wigner solids and supersolids [158, 160]. Below we review recent experimental progress in the studies of dipolar interlayer exciton fluids with and without a lattice.

3.2.1. Strongly correlated excitons in a continuum

Although optical pumping can create dipolar interlayer excitons in a rather simple TMDC heterobilayer with type-II band alignment [6, 83, 159], it remains difficult to produce a high-density exciton fluid using this method because of the short exciton lifetime at high exciton densities due to electron-hole wavefunction overlap and Auger relaxations [83]. Instead, we will focus in this section Coulomb-coupled TMDC bilayers with type-II band alignment, in which a thin hexagonal boron nitride (hBN) tunnel barrier is inserted between the two TMDC layers

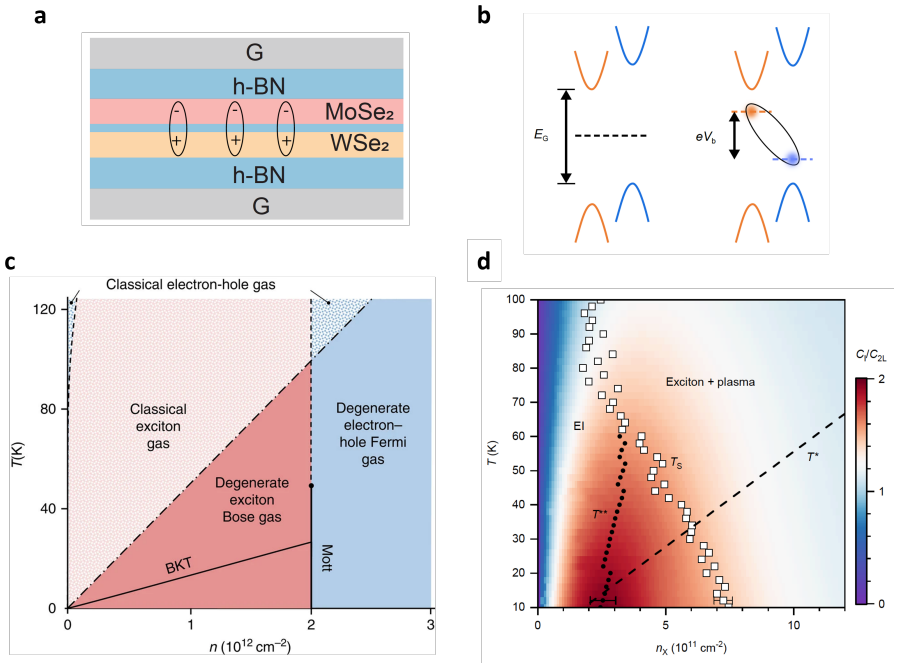

Fig. 15. Dipolar exciton fluid. (a) Schematic of a Coulomb-coupled $MoSe_2/WSe_2$ electron–hole double-layer encapsulated by top and bottom graphite gates. (b) Type-II band alignment of the double-layer with interlayer band gap E_G (left). An interlayer bias voltage V_b separates the electron and hole chemical potentials (dashed lines) and reduces the charge gap (right). Interlayer excitons are formed spontaneously when V_b, which acts as a chemical potential for excitons, exceeds the exciton energy $E_G - E_B$. (c,d) Schematic (c) and experimental (d) exciton phase diagram in the temperature and exciton density plane. (c) The dashed lines indicate crossovers and the solid lines mark the phase transitions. The dot is the Mott critical point. (d) Exciton compressibility as a function of temperature and exciton density. The white squares denote the exciton ionization temperature, which characterizes a crossover from the EI (left) to an electron–hole plasma (right). The dashed line and dotted line show, respectively, the degeneracy temperature per flavour for non-interacting excitons and the temperature corresponding to the exciton compressibility peak. Panel (a) reprinted from [Z. Wang, D. A. Rhodes, K. Watanabe, T. Taniguchi, J. C. Hone, J. Shan, and K. F. Mak, Nature, 574, 76–80, 2019] [88]. Panels (b) and (d) reprinted from [L. Ma, P. X. Nguyen, Z. Wang, Y. Zeng, K. Watanabe, T. Taniguchi, A. H. MacDonald, K. F. Mak, and J. Shan, Nature, 598, 585–589, 2021] [92]. Panel (c) reprinted with permission from [M. M. Fogler, L. V. Butov, and K. S. Novoselov, Nat. Commun., 5, 4555, 2014] [7].

to further prevent electron-hole recombination [88, 92] (Figure 15(a)). The two TMDC layers are separately contacted by metal electrodes; an interlayer bias voltage can populate electrons in one layer and holes in the other, forming a dipolar exciton fluid below the exciton Mott density [7, 158]. We will first discuss the limit of an equilibrium exciton fluid, in which the excitons have practically infinite lifetime [92]. The electron and hole layers are maintained at the same electrochemical potentials as the metal electrodes, which serve as electrical reservoirs [151]; the exciton density and chemical potential are determined by the electrostatics of a parallel plate capacitor. We will then discuss the physics of a non-equilibrium exciton fluid, in which the electron and hole layers have different electrochemical potentials from the metal electrodes [88]. The exciton density is determined by a balance between electrical pumping from the electrodes and exciton decays [161].

Thermodynamics of an equilibrium exciton fluid We consider a TMDC heterobilayer (e.g. $MoSe_2$/WSe_2) with a thin hBN barrier and type-II band alignment (Figure 15(a,b)). The two TMDC layers are separately contacted by metallic electrodes, which serve as electrical reservoirs for excitons [92,151]. The Fermi energy is aligned for the two layers and inside the semiconductor band gap, E_G, under zero interlayer bias voltage. The Fermi levels of the two layers are split by a finite bias voltage, V_b; the charge gap of the system is reduced to $E_G - V_b$. When the charge gap becomes smaller than the interlayer exciton binding energy, $E_B \geq E_G - V_b$, an interlayer exciton fluid or an excitonic insulator is expected to form spontaneously [162–164]. The exciton chemical potential, which is equal to the difference in the electron and hole chemical potentials, is given by V_b (Ref. [151]). A highly tunable exciton fluid (in both density and chemical potential) is created.

A recent experiment has realized such electrically tunable exciton fluid in equilibrium [92]. The Coulomb-coupled electron-hole double layer structure is further encapsulated by top and bottom electrical gates (Figure 15(a)). The gates allow tuning of the electron-hole density imbalance and measurements of the differential penetration capacitance, C_P. Measurement of C_P is achieved by applying a small A.C. voltage on the top gate and collecting the induced charge density through the bottom gate (Figure 16(a)). It measures how well the heterobilayer screens an A.C. electric field and is approximately given by the charge compressibility of the entire double layer [165–167]. The bias and gate voltage dependence of C_P is shown in Figure 16(b). The red region corresponds to a charge-incompressible double layer with $C_P \approx C_{gg}$, the gate-to-gate geometrical capacitance; the double layer fails to screen the A.C. electric field here. When one of the TMDC layers is doped with charge carriers (electrons or holes), the double layer becomes charge-compressible with $C_P \ll C_{gg}$ (the blue region); the A.C. electric field is efficiently screened. The charge gap of the system at a specific bias voltage is given by the integration of C_P/C_{gg} with respect to the gate voltage. It vanishes for $V_b \geq E_G \approx 0.68V$.

In addition to penetration capacitance measurements, the electron-hole interlayer capacitance, C_I, is also measured by applying a small A.C. bias voltage on one of the TMDC layers and collecting the induced charge density through the other layer (Figure 16(c)). It is equal to the isothermal exciton compressibility, κ_X (Ref. [151]). Figure 16(d) shows the bias and gate voltage dependence of C_I. The blue region is exciton-incompressible with $\kappa_X \approx 0$, i.e. there is no exciton in the double layer. The system is exciton-compressible only when both electrons and holes are populated in the double layer (red region), i.e. an exciton fluid is formed. Intriguingly, the onset of the exciton-compressible region occurs at $V_b \approx 0.65V$, which is about 30 mV below the onset of the charge-compressible region at $V_b \approx E_G$. Therefore, the triangular region bound by the two onsets (white dashed lines) and the charge-incompressible region (red dashed lines) represents a system that is charge-incompressible but exciton-compressible, i.e. an excitonic insulating state [161]. The difference in V_b between the two onsets provides a measurement of the exciton binding energy $E_B \approx 25$ mV in the zero-exciton-density limit [151].

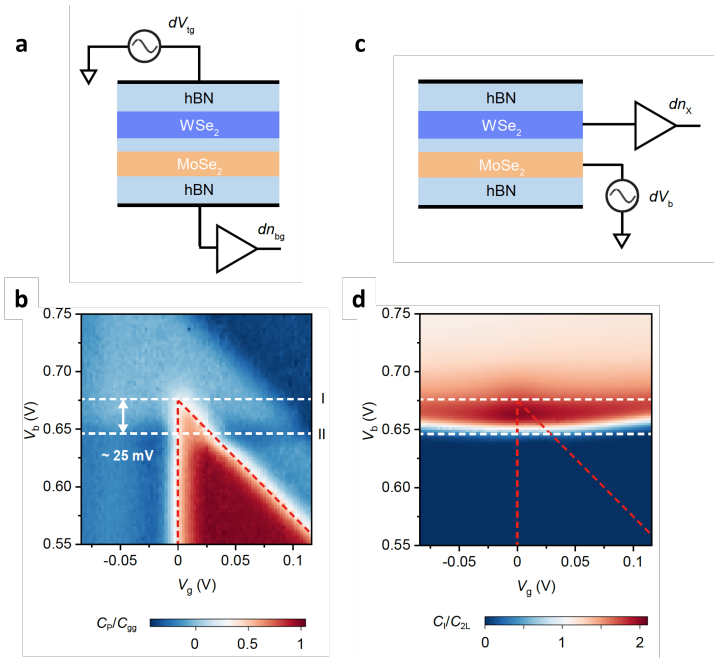

Fig. 16. Excitonic insulator in Coulomb-coupled bilayers. (a,c) Schematics of the penetration (a) and interlayer capacitance (c) measurements. The double layer is A.C. grounded in (a). (b,d) Normalized penetration capacitance (b) and interlayer capacitance (d) as a function of bias and gate voltages. The charge incompressible region in (b) is enclosed by red dashed lines. White dashed line I and II correspond to the bias voltages at which the charge gap closes and the exciton population appears, respectively. Their difference (25 mV) provides an estimate of the exciton binding energy in the limit of zero exciton density. Reprinted from [L. Ma, P. X. Nguyen, Z. Wang, Y. Zeng, K. Watanabe, T. Taniguchi, A. H. MacDonald, K. F. Mak, and J. Shan, Nature, 598, 585–589, 2021] [92].

The ability to control the exciton density continuously also allows experimental mapping of the exciton phase diagram. Figure 15(d) shows the exciton compressibility as a function of temperature and the exciton density. The square data points show the ionization temperature of the exciton fluid; it separates the crossover from an excitonic insulator to an electron-hole plasma; the density-tuned transition between these two states in the zero-temperature limit is known as the Mott transition [168]. The ionization temperature is determined by penetration capacitance measurements; specifically, the charge gap of the double layer vanishes above the ionization temperature at each exciton density. The dashed line denotes the degeneracy temperature per flavor for non-interacting excitons [7]; it scales linearly with the exciton density with a slope that is determined by the non-interacting exciton density of states in 2D. The actual degeneracy temperature of the exciton fluid (black dots), as determined by the position of the exciton compressibility maximum, also scales linearly with the exciton density but with a slope that is about 5-6 times larger than that for the non-interacting degeneracy temperature. For a strongly correlated exciton fluid, in which the exciton-exciton interaction energy far exceeds the exciton kinetic energy, the degeneracy temperature is no longer determined by the kinetic energy but by the interaction energy [149, 169]. A 5-6 times larger slope corresponds to an exciton dimensionless coupling constant (the ratio of the interaction energy to the kinetic energy) about 10-12. The exciton fluid is in the strong correlation regime, which helps suppress both

density and phase fluctuations of the exciton fluid and enhances the superfluid transition (or BKT) temperature [149, 169]. The existence of exciton superfluidity remains to be demonstrated.

Evidence of exciton condensation from optoelectronics studies A device structure similar to Figure 15(a) but with thinner hBN barrier can also support an out-of-equilibrium exciton fluid by electrical pumping. When the electrical contacts to the electron and hole layers have contact resistance large compared to the interlayer tunneling resistance, the electron and hole layers can no longer be maintained at the same electrochemical potential with the metallic electrodes; the potential drops at the contacts dominate the interlayer potential drop [161] (Figure 17(a)). In this limit, electrons and holes are continuously pumped into the TMDC layers from the metal electrodes; they also recombine/decay (both radiatively and non-radiatively) at the electron-hole tunnel junction. The net result is an out-of-equilibrium exciton fluid with density that is not determined by electrostatics but by the balance between pumping and decay in the steady state [161]. Compared to the equilibrium exciton fluid in the previous sub-section, the excitons here are more tightly bound because of the thinner hBN barrier; the radiative recombination of the excitons at the tunnel junction and the accompanied electroluminescence (EL) also enables an optoelectronic probe of the exciton fluid. However, it is difficult to determine the exciton density because the pumping and decay rates are poorly characterized.

Intriguingly, a threshold dependence of the exciton EL intensity on the tunneling current, which increases with the exciton density, is observed [88] (Figure 17(b)). Intensity correlation measurements also show photon bunching near the EL threshold, corresponding to enhanced photon number fluctuations. Moreover, both the EL intensity and the intensity correlation depend sensitively on the electron-hole density imbalance in the exciton fluid near and slightly above the threshold. These results signify the onset of exciton condensation as the exciton density increases with the tunneling current. The EL threshold and the accompanied photon bunching are analogous to the onset of lasing, which is an out-of-equilibrium continuous phase transition [170–172]. In particular, photons condense into a single cavity mode above the lasing threshold, accompanied by critical photon number fluctuations near the threshold. There is, however, no optical cavity in the electron-hole double layer device. Instead, the onset of exciton condensation and spontaneous interlayer phase coherence induces superradiant EL above the threshold [144]. The photon bunching near the threshold corresponds to critical fluctuations near the continuous phase transition from a normal exciton fluid to an exciton condensate. The sensitivity to electron-hole density imbalance near and slightly above the threshold is also consistent with the emergence of exciton condensation, which requires electron-hole Fermi surface nesting [173–175].

Finally, we note that although the experimental observations point to possible exciton condensation, EL intensity and intensity correlation measurements are not phase sensitive measurements that can directly reveal the emergence of spontaneous interlayer phase coherence. Future studies on the spatial and temporal dependence of the electric field correlation function are required to unambiguously establish the onset of spontaneous phase coherence [144, 145].

3.2.2. Strongly correlated excitons in a moiré lattice

Semiconductor moiré materials are a unique platform to explore the interplay between strong electronic correlations and non-trivial band topology [128, 176]. They can be thought of as a periodic array of artificial atoms that can trap electrons in the moiré length scale [177–180]. Both the average electron filling per moiré atom and the trapping potential depth can be continuously tuned by electrostatic gating, realizing a highly controllable quantum system [123–127, 181–184]. In addition to trapping electrons, heterostructures of semiconductor moiré materials can also trap excitons to realize strongly correlated bosonic physics in a lattice [93, 94, 185–188], akin to cold atom experiments with optical trapping [189].

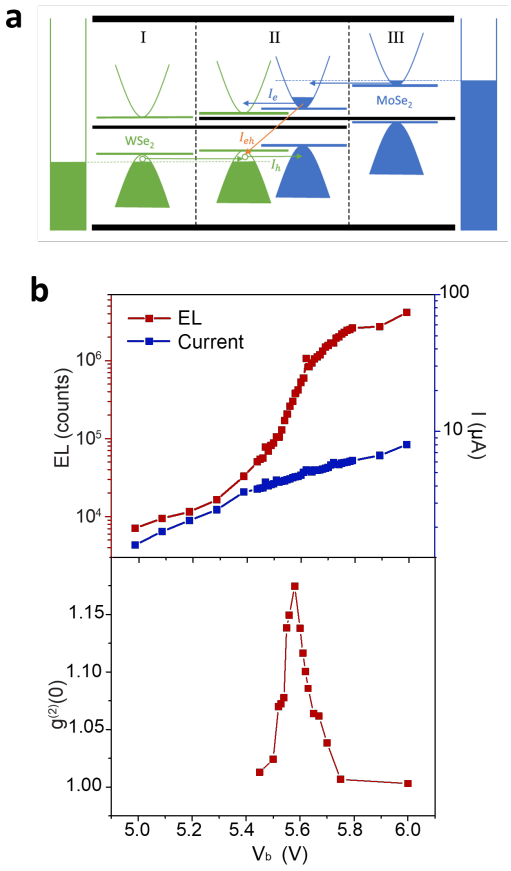

Fig. 17. Evidence of out-of-equilibrium exciton condensation. (a) Schematic of electron-hole transport processes in a bilayer TMD system with isolated monolayer TMD regions near the contacts and effective contact resistances that are larger than the interlayer tunnel resistance. The thick black lines show the bilayer system and the top and bottom gates. The $MoSe_2$ and WSe_2 bands are shown in blue and green, respectively, and the dotted lines show the electron and hole Fermi levels set by the gate and bias voltages. The tunneling current is limited by the injection current from region III, and regions II and III in the $MoSe_2$ layer are not able to reach equilibrium. Reprinted figure with permission from [Y. Zeng and A. H. MacDonald, Phys. Rev. B, 102, 085154, 2020] [161]. Copyright 2020 by the American Physical Society. (b) Bias voltage dependence of the integrated electroluminescence intensity and tunnelling current (top), and of the electroluminescence intensity correlation at zero time delay (bottom). A threshold behavior is observed near 5.6 V. Reprinted from [Z. Wang, D. A. Rhodes, K. Watanabe, T. Taniguchi, J. C. Hone, J. Shan, and K. F. Mak, Nature, 574, 76–80, 2019] [88].

There are several related but different heterostructures that can realize correlated exciton physics in a lattice. The simplest structure is twisted bilayer TMDC near AB-stacking [186, 190] (or near H-stacking for natural bilayer TMDCs). The spin-valley locking in each monolayer [19, 191] nearly spin-forbids the interlayer tunneling process in this stacking structure, effectively realizing two Coulomb-coupled moiré lattices. A related but different structure is to insert another multilayer TMDC, as a tunnel barrier, in between the AB-aligned bilayer TMDC [186, 187]. Because of the lattice mismatch between different TMDCs, Coulomb-coupled moiré lattices are formed at both the top and bottom interfaces of the multilayer structure. The advantage compared to AB-twisted bilayer TMDCs is the additional suppression of interlayer tunneling by the barrier. A third structure is to Coulomb-couple a TMD moiré lattice with a monolayer TMDC through a thin hBN barrier [93, 94, 185]. The moiré layer provides the trapping potentials for excitons. The hBN barrier effectively suppresses interlayer tunneling. In all cases, the separation between the active TMDC layers is substantially smaller than the moiré period of the superlattice. The entire heterostructure is also encapsulated between top and bottom electrical gates that can independently tune the total electron density of the heterostructure and the vertical electric field that redistributes electrons between the constituent TMDC layers.

To see how excitons are formed in these structures, we start with one moiré layer in the Mott or Wigner-Mott insulating state (see Section 3.3.2 for more discussions) and the other layer depleted of electrons [93, 94, 187] (Figure 18(a)). Excitons are formed when electrons are transferred by the vertical electric field to the empty layer because the transferred electrons remain bound to the empty sites (holes) left behind in the original moiré layer in order to minimize the total Coulomb repulsion energy of the entire system. The exciton binding energy is approximately the interlayer on-site Coulomb repulsion U' for the Mott state and the interlayer nearest-neighbor Coulomb repulsion V' for the Wigner-Mott state. These interlayer Mott and Wigner-Mott states after electron transfer are distinct from the original layer-polarized Mott and Wigner-Mott states because bosonic degrees of freedom (excitons) that can hop around the lattice are created. They can be regarded as excitonic insulators that host an exciton fluid. The exciton-exciton interaction is equal to the difference in the intra- and inter-layer Coulomb repulsion between the electrons [188]. The exciton kinetic energy is also substantially suppressed by the moiré potential [192]. The net result is a strongly correlated exciton fluid in a lattice.

Excitonic insulating states at total integer and fractional fillings of the moiré lattice The emergence of an excitonic insulating state at filling factor $\nu = 1$ of the moiré lattice has been recently reported in Coulomb-coupled WSe_2/WS_2 moiré and WSe_2 monolayer [93, 94]. The band alignment near the valence band maximum of both layers is shown in Figure 18(c). Because of the interlayer coupling in the WSe_2/WS_2 moiré bilayer, the WSe_2 moiré valence band maximum is pushed up in energy with respect to that of monolayer WSe_2 under zero vertical electric field. Electrostatic gating can independently tune the Fermi level (or the hole doping density) and the band alignment (or the interlayer charge distribution). Starting from a Mott insulator at $\nu = 1$ of the WSe_2/WS_2 moiré lattice and an empty WSe_2 monolayer, an excitonic insulating state is expected to emerge when holes are transferred from the moiré layer to the monolayer while keeping the total filling factor unchanged.

The electrostatics phase diagram of the Coulomb-coupled heterostructure has been mapped out by photoluminescence (PL) spectroscopy [93, 94]. In the parameter range shown in Figure 18(b), four different regions can be identified: 1) a charge-neutral monolayer and a hole-doped moiré layer in region I; 2) a hole-doped monolayer and a moiré layer in the Mott insulating state in region II; 3) both layers are hole doped in region III; and 4) a charge-neutral moiré layer and a hole-doped monolayer in region IV. Correlated insulating states at both fractional and integer filling factors can be identified in the moiré layer in region I. The band alignments corresponding to the four different electrostatics regions are summarized in Figure 18(c). Excitonic insulating

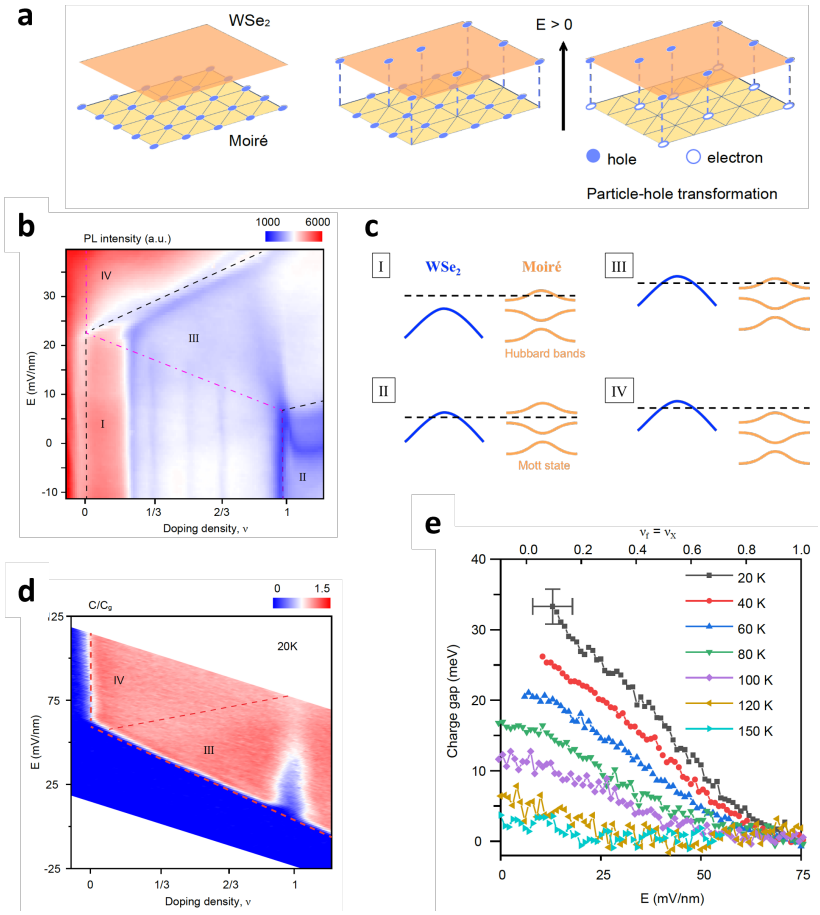

Fig. 18. Excitonic insulator in a moiré latter. (a) Left, electronic Mott insulator at $\nu = 1$ when all the holes reside in the moiré layer. Middle, some of the holes are transferred to the WSe_2 monolayer under a positive electric field. They are tightly bound to the empty moiré sites to minimize the total Coulomb repulsion energy. Right, the empty sites in the moiré layer are equivalent to electrons under a particle–hole transformation. A dipolar exciton fluid in the moiré lattice forms. (b) Peak PL intensity of the moiré layer as a function of ν and electric field. The four regions I–IV are defined by the electrostatic doping density in the monolayer (ν_f) and moiré layer (ν_m). Region I, $\nu_f = 0$ and $0 < \nu_m < 1$. Region II, $\nu_f > 0$ and $\nu_m = 1$. Region III, $\nu_f > 0$ and $0 < \nu_m < 1$. Region IV, $\nu_f > 0$ and $\nu_m = 0$. The boundaries are shown in the dashed and dash-dotted lines. (c) Corresponding band alignments in the two layers for the electrostatics regions I-IV. The single-particle band is shown for monolayer WSe_2 and the Hubbard bands are shown for the moiré layer. The dashed line denotes the Fermi level. (d) Normalized differential gate capacitance C/C_g as a function of ν and electric field. Only regions III and IV are accessible because of the device structure. A charge-incompressible state is observed at total filling $\nu = 1$ in region III. (e) Charge gap extracted from the capacitance as a function of electric field (bottom axis) and doping density (or exciton density; top axis) in the monolayer at varying temperatures. Reprinted from [J. Gu, L. Ma, S. Liu, K. Watanabe, T. Taniguchi, J. C. Hone, J. Shan, and K. F. Mak, Nat. Phys., 18, 395–400, 2022] [94].

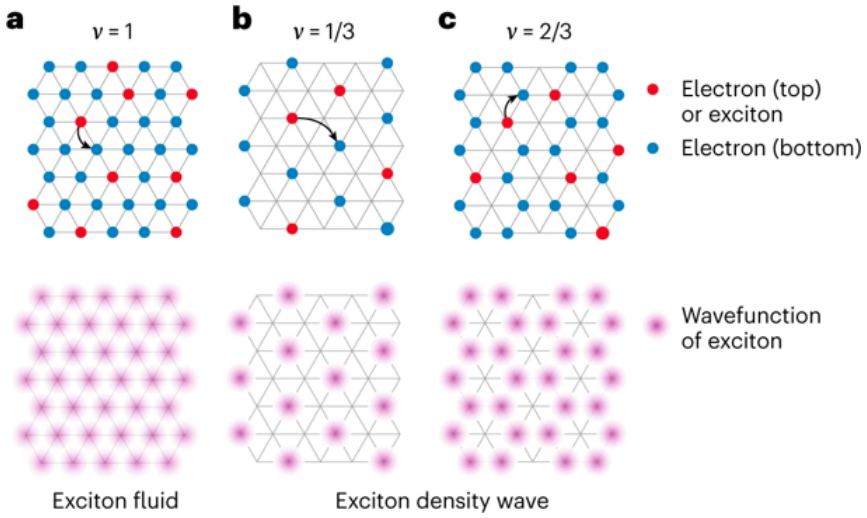

Fig. 19. Exciton densities. (a-c) Schematic representation of the inter-layer Mott insulator at total filling $\nu = 1$ (a), and of the inter-layer Wigner crystals at $\nu = 1/3$ (b) and $\nu = 2/3$ (c). Top, electrons in the top (red) and bottom (blue) layer. Electrons in the top layer are bound to the empty sites in the bottom layer directly below them to minimize the Coulomb interactions. The bound states form interlayer excitons that can hop around the moiré lattice (arrows). The exciton hopping is unrestricted in (a), but is guided to the channels defined by the inter-layer Wigner crystals in (b) and (c). Bottom: The exciton density distribution shows an exciton fluid at $\nu = 1$ that preserves the lattice symmetry and exciton density waves at $\nu = 1/3, 2/3$ that break the translational symmetry of the lattice. Reprinted from [Y. Zeng, Z. Xia, R. Dery, K. Watanabe, T. Taniguchi, J. Shan, and K. F. Mak, Nat. Mater., 22, 175–179, 2023] [187].

state is expected to emerge at total filling factor $\nu = 1$ in region III, where holes are shared between the two layers.

Figure 18(d) shows the electric field and filling factor dependence of the differential bottom gate capacitance, C, of the device covering regions III and IV (the only regions accessible in capacitance measurements [94]). The differential capacitance is directly connected to the charge-compressibility of the Coulomb-coupled heterostructure. Specifically, the system is charge-compressible for $C \approx C_g$, the bottom gate geometrical capacitance (red regions), and is charge-incompressible for $C < C_g$ (the blue area in region III). The charge-incompressible state at total filling $\nu = 1$ in region III is consistent with the emergence of an excitonic insulator. The extracted charge gap (or the exciton binding energy) as a function of the vertical electric field (bottom axis) and the exciton density (in units of the moiré density, top axis) is shown in Figure 18(e). The charge gap decreases with increasing exciton density and temperature. It vanishes continuously at about 80% of the moiré density at 20 K; the value provides an estimate of the Mott density, above which the exciton fluid is ionized to an electron-hole plasma. The exciton ground state is expected to be a superfluid [185, 186, 188], which remains to be demonstrated experimentally.

In the Coulomb-coupled moiré-monolayer system, no correlated insulating state can be identified at total fractional fillings in region III. Only an excitonic insulating state at $\nu = 1$ is observed; the state hosts excitons hopping between moiré lattice sites without restriction; the resultant exciton density distribution preserves the translational symmetry of the lattice (Figure 19(a)). The lack of total fractional states is likely caused by the high electron kinetic energy in the WSe_2 monolayer, which quantum melts the generalized Wigner crystals (or Wigner-Mott

insulators) at total fractional fillings. To stabilize these states in region III, the monolayer has to be replaced by a more correlated system with substantially lower electron kinetic energy. This has been recently demonstrated in an angle-aligned monolayer WS_2/bilayer WSe_2/monolayer WS_2 heterostructure [187]. The heterostructure supports Coulomb-coupled moiré lattices of nearly identical period at the top and bottom interfaces. Using a Rydberg sensing technique that can probe the charge-compressibility of the heterostructure [125] (see 3.3.2 for details of the technique), excitonic insulating states at total fractional fillings $\nu = 1/3, 2/3, 4/3, 5/3$ in region III have been reported. The states can be understood as exciton density waves [193, 194], in which excitonic hopping is restricted to sites that are defined by the interlayer Wigner crystals at $\nu = 1/3, 2/3, 4/3, 5/3$ in order to minimize the total Coulomb repulsion energy (Figure 19(b,c)). In contrast to the excitonic insulating state at total filling $\nu = 1$, the resultant exciton density distribution spontaneously breaks the translational symmetry of the lattice. It provides a rare physical realization of symmetry-broken exciton insulators, whose ground state is expected to be a supersolid [194–196].

3.3. Probing strongly correlated electrons with excitons

In addition to realizing strongly correlated states of excitons, the tightly bound excitons in 2D TMDCs and the accompanied strong light-matter interaction also provide a unique opportunity to probe strongly correlated states of electrons, especially in the regime of low carrier density and magnetic moment density usually inaccessible by probes developed for conventional quantum materials. We will discuss the recent progress in this interesting direction of research. In particular, we will focus on the tunable Hubbard model physics realized in TMDC moiré materials and discuss how one could use excitons as a probe for the correlated insulating states, quantum phase transitions and magnetic properties in these materials.

3.3.1. Hubbard model physics

TMDC moiré materials are formed by stacking either two identical TMDC monolayers with a small twist angle (homobilayer) or two different TMDC monolayers with a lattice mismatch (heterobilayer). In both cases, the interference in the constituent atomic structures produces a moiré superlattice. Because the moiré period is many times larger than the atomic lattice constant of the TMDC monolayers, one can discard the original atomic lattice structure as long as low-energy physics is concerned [177, 197]. The moiré band structure within the mini-Brillouin zone can be obtained by treating electrons with a band mass of the monolayer TMDCs moving in a smooth periodic moiré potential of the superlattice.

In the case of a sufficiently isolated moiré conduction/valence band, the low-energy physics can be mapped to a single-band extended Hubbard model in a triangular lattice [177]. The electrons can hop between nearest-neighbor sites with an amplitude t, experience an on-site Coulomb repulsion U when two electrons are at the same site, and interact with other electrons at different sites via the extended-range Coulomb repulsion V. The typical energy scales in TMDC moiré materials are $t \sim 1 - 10$ meV, $U \sim 100$ meV and $V \sim 50$ meV. In many cases, the Coulomb energy can completely dominate the electron kinetic energy; the system is in the strongly correlated regime.

In a typical experiment, the TMDC moiré material is encapsulated between top and bottom gates with hBN as the gate dielectric (Figure 20(a)). The two gates allow independent tuning of the electron filling factor of the moiré lattice ν (or electron density) and the vertical electric field, which tunes the moiré band offset between the two TMDC layers via the Stark effect. Because the moiré potential originates from spatially modulated interlayer hopping in the TMDC bilayers [177, 197], tuning the moiré band offset tunes the moiré trapping potential depth, which in turn tunes the electronic bandwidth ($\propto t$) predominantly [183]. The setup realizes a highly controllable quantum manybody system with tunable chemical potential and effective interaction

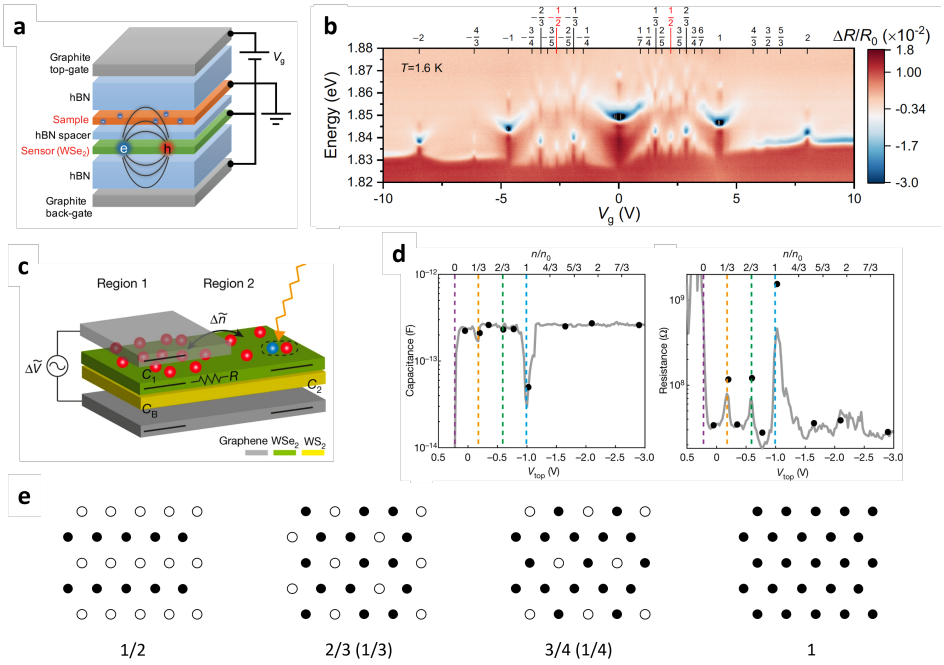

Fig. 20. Mott and Wigner-Mott insulators. (a) Schematic device structure and electric circuitry. The bound electron–hole pair (exciton) with its electric-field lines beyond the sensor layer probes the compressibility in the sample controlled by electrostatic gating. (b) Gate-dependent reflection contrast spectrum near the 2s exciton in the sensor. An abundance of insulating states is revealed by blueshifts and enhanced spectral weight in the 2s exciton resonance. The top axis shows the filling factor for the insulating states. (c) Device schematic for an optically detected capacitance and resistance measurement in a WSe_2/WS_2 moiré. A small a.c. bias leads to charge redistribution between region 1 and region 2, which is detected by changes in the optical reflectivity in region 2. C_1, C_B and C_2 are the geometric capacitances in the system, and R and C_Q are the doping-dependent resistance and quantum capacitance, respectively, of the sample. (d) Capacitance (left) and resistance (right) of region 1. The decreased capacitance and increased resistance indicate emerging insulating states at $\nu = 1/3, 2/3, 1$. (e) Ground state charge configurations at different filling factors. Filled and unfilled circles denote occupied and empty sites for state ν, respectively. The occupied and empty sites are switched for the state $1 - \nu$. Panels (a), (b), (e) reprinted from [Y. Xu, S. Liu, D. A. Rhodes, K. Watanabe, T. Taniguchi, J. Hone, V. Elser, K. F. Mak, and J. Shan, Nature, 587, 214–218, 2020] [125]. Panels (c), (d) reprinted with permission from [E. C. Regan, D. Wang, C. Jin, M. I. Bakti Utama, B. Gao, X. Wei, S. Zhao, W. Zhao, Z. Zhang, K. Yumigeta, M. Blei, J. D. Carlström, K. Watanabe, T. Taniguchi, S. Tongay, M. Crommie, A. Zettl, and F. Wang, Nature, 579, 359–363, 2020] [123].

strengths measured by U/t and V/t. Below we will discuss the application of excitons in TMDCs to probe the emergent correlated states of electrons in a Hubbard system.

3.3.2. Mott and Wigner-Mott insulators

In the strong correlation limit ($U/t \gg 1$ and $V/t \gg 1$), the TMDC moiré system is in the Mott insulating state at $\nu = 1$ (half-band-filling) [123, 124, 126, 127, 181, 183] and the Wigner-Mott insulating state (or generalized Wigner crystal) at fractional lattice fillings [123, 125, 182, 198] (Figure 20(e)). These states are charge-incompressible, i.e. gapped for charge excitations. They emerge as an attempt of the system to minimize the total Coulomb energy cost. In the Mott insulating state, the charges are localized to the moiré sites by the strong on-site Coulomb U; the low-energy physics are governed by collective spin excitations (see Section 3.3.5). In contrast to the Mott insulating state, which preserves the translational symmetry of the moiré lattice, the Wigner-Mott insulating states break the translation symmetry of the lattice; the charges are localized by the extended-range Coulomb V. Similar to the Mott insulating state, collective spin excitations govern the low-energy physics.

These states were detected by multiple spectroscopy methods involving TMDC excitons [123, 125, 199–202]. Here we focus on two techniques: 1) optical readout of electronic compressibility [123] and 2) Rydberg sensing of dielectric constant [125]. The first method relies on the strong light-matter interactions and the sensitivity of the excitonic absorption on the doping density in 2D TMDCs [3, 29]. The TMDC moiré device is divided into two regions, the sample region with both top and bottom gates and the readout region with only the bottom gate (Figure 20(c)). The bottom gate sets a particular doping density in the readout region in order to achieve a high sensitivity of the excitonic absorption to a small change in the doping density in this region. The top gate controls the doping density in the moiré sample, in this case angle-aligned WSe_2/WS_2 bilayer. A small A.C. top gate voltage is also applied to modulate the doping density in the sample region. When there is an extremely large contact resistance at the TMDC-metal junction (not shown), charges modulated at a sufficiently high frequency cannot go through the contact region; instead, they can only be transferred between the sample and the readout regions. The amount of charges that can be transferred and the rate of the transfer depend on the geometric capacitances of the top and bottom gates, and the quantum capacitance and resistance of the moiré sample. Therefore, by measuring the modulated charge density in the readout region as a function of the modulation frequency (through optically detecting the change in the excitonic absorption), both the quantum capacitance and resistance of the moiré sample can be extracted (Figure 20(d)). The Mott insulating state at $\nu = 1$ and the Wigner-Mott insulating states at $\nu = 1/3, 2/3$ are observed.

The second method utilizes the sensitivity of the exciton binding energy in monolayer TMDCs to their surrounding dielectric environment [3, 29, 203]. The optical transitions in monolayer TMDCs are dominated by excitonic Rydberg resonances (1s, 2s, 3s, ...) [3, 29]. Measurements of the Rydberg resonances allow the determination of the exciton binding energy. The binding energy increases (decreases) with decreasing (increasing) dielectric constant of the surrounding environment. We now consider a device structure, in which a sample of interest is brought close to but without direct electronic coupling with a monolayer TMDC (Figure 20(a)). This can be achieved by inserting a thin hBN barrier between the sample and the TMDC monolayer. The exciton binding energy in the monolayer TMDC is now sensitive to the dielectric constant of the sample. In particular, the binding energy is large (small) when the sample is charge-incompressible (compressible). The monolayer TMDC is a sensor of the electronic states in the sample.

In practice, Rydberg sensing of electronic states can be carried out by monitoring the energy and spectral weight of the 2s Rydberg resonance in the sensor [125]; the 2s Rydberg state has a Bohr radius about 5 nm, providing a convenient distance range for the sample-sensor separation. Figure 20(b) shows the dependence of the sensor's 2s Rydberg state reflection contrast spectrum

on the doping density (or ν) in a WSe_2/WS_2 moiré sample. A blue shift in the 2s resonance accompanied by an enhanced reflection contrast is observed at each insulating state in the moiré sample. These include the $\nu = 2$ band insulating state, the $\nu = 1$ Mott insulating state and an abundance of Wigner-Mott insulating states at fractional lattice fillings. These states are fully consistent with the predictions of an extended triangular lattice Hubbard model in the flat band limit.

3.3.3. Mott and Wigner-Mott transitions

Whereas the TMDC moiré system in the strong correlation limit is in the Mott insulating state at $\nu = 1$ and the Wigner-Mott insulating state at fractional lattice fillings, it is a Fermi liquid in the weak correlation limit. A transition from the correlated insulating states to a Landau Fermi liquid is expected when the moiré bandwidth is comparable to U or V (Ref. [204, 205]). Such bandwidth-controlled metal-insulator transition (MIT) is driven first-order in most cases because the transition is accompanied by other structural and magnetic phase transitions that break symmetries [204]. Whether a continuous bandwidth-controlled MIT exists has remained as an open question [206–209]. This is particularly the case for the Wigner-Mott transition, which involves translational symmetry breaking of the lattice; whether a continuous Wigner-Mott transition is possible is far from clear. The geometrically frustrated triangular lattice and the 2D nature of TMDC moiré materials, both of which suppress magnetic ordering, could favor continuous bandwidth-controlled MITs. Quantum spin liquids have also been predicted near such MITs [206, 210].

Recently, bandwidth-controlled MITs have been realized in TMDC moiré materials [181, 183]. Electrical transport measurements have provided strong evidence of a continuous Mott transition at fixed filling factor $\nu = 1$. No magnetic phase transition is detected near the MIT down to 5% of the Curie-Weiss temperature [183], suggesting a quantum phase transition from a non-magnetic Mott insulator to a Landau Fermi liquid. In addition to electrical transport measurements, the Rydberg sensing technique has also been applied to monitor the dielectric constant near the bandwidth-controlled MITs in angle-aligned $MoSe_2/WS_2$ bilayers [211]. By tuning the moiré band offset by a vertical electric field, a continuously vanishing oscillator strength for the 2s Rydberg state in the sensor is observed near both the Mott and Wigner-Mott transitions. The result shows a diverging dielectric constant near the MITs. The observed dielectric catastrophe reflects the critical charge dynamics near these transitions [212], suggesting that both the Mott and Wigner-Mott transitions are continuous in this system.

3.3.4. Stripe phases and electronic liquid crystals

In addition to breaking the translational symmetry of the moiré lattice, some correlated insulating states at fractional fillings also break the rotational symmetry of the system, e.g. $\nu = 2/5, 1/2, 3/5$ (Figure 20(e)). These are known as stripe crystals [213, 214]; they form as a compromise between competing short-range and long-range Coulomb repulsions. The strong light-matter interactions in 2D TMDCs provide a unique opportunity to probe these states using excitonic enhanced optical anisotropy measurements. Because of the spontaneously broken rotational symmetry in the system, the complex optical conductivities parallel and perpendicular to the major axis of the stripe phases are different. Linearly polarized incident light reflected from the sample would in general have its polarization axis rotated by a small angle (unless the incident polarization is parallel or perpendicular to the major axis). The polarization rotation angle can be significantly enhanced when the photon energy is near the strong exciton resonances in the TMDC moiré material.

Based on this idea, a recent study has measured the polarization rotation angle as a function of the electron filling factor in angle-aligned WSe_2/WS_2 bilayers [215] (Figure 21(a)). A strong optical anisotropy peaked at $\nu = 1/2$ is observed. The anisotropy signal decreases to zero

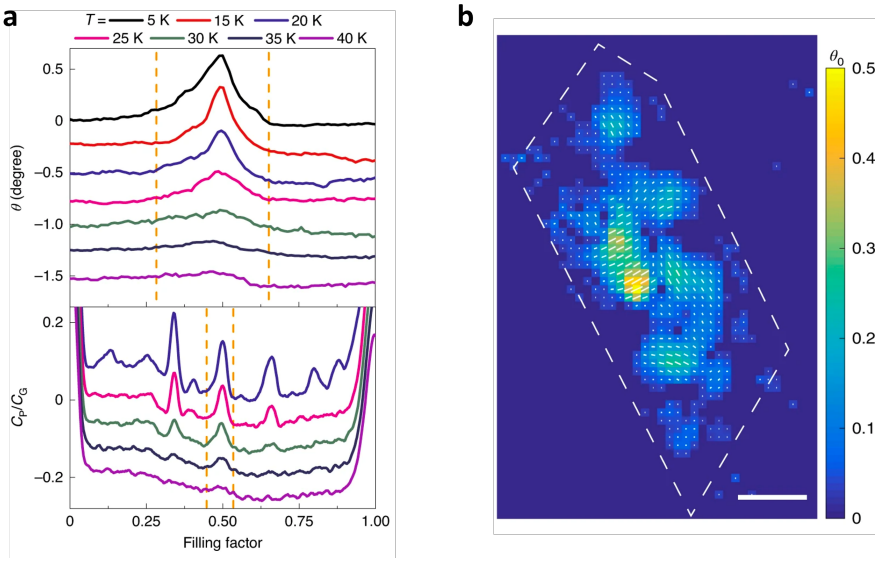

Fig. 21. Stripe phases. (a) Gate-dependent polarization rotation (upper panel) and the corresponding penetration capacitance (lower panel) at different temperatures. The curves are vertically displaced for clarity. The peak at $\nu = 1/2$ decreases continuously with temperature and disappears around 35 K, showing continuous thermal melting of the stripe crystal. Vertical dashed lines mark the region with optical anisotropies (upper panel) and the upper limit of the insulating region around $\nu = 1/2$ (lower panel). The optical anisotropies persist into the compressible region. (b) Domain pattern of electronic stripes at $\nu = 1/2$. The length and orientation of the line segments at each pixel represent the local amplitude and orientation of anisotropy and the color corresponds to the anisotropy amplitude. Reprinted from [C. Jin, Z. Tao, T. Li, Y. Xu, Y. Tang, J. Zhu, S. Liu, K. Watanabe, T. Taniguchi, J. C. Hone, L. Fu, J. Shan, and K. F. Mak, Nat. Mater., 20, 940–944, 2021] [215].

above the melting temperature ($\approx$ 35 K) of the stripe crystal. Moreover, by rotating the incident polarization angle and monitoring the polarization rotation angle at each point of the sample, a spatial map of the major axis of the stripe crystal can be obtained (Figure 21(b)). (The polarization rotation angle is zero when the incident polarization is parallel/perpendicular to the major axis.) The result demonstrates multiple stripe domains inside the mesoscopic sample.

Intriguingly, strong optical anisotropy is not only observed at the stripe crystals at $\nu = 2/5, 1/2, 3/5$ but also observed at generic filling factors, where the system is charge-compressible based on differential capacitance measurements (Figure 21(a)). A broad optical anisotropy peak centered at $\nu = 1/2$ but extends all the way down to $\nu = 1/3$ and up to $\nu = 2/3$ is observed. The presence of strong optical anisotropy at compressible electronic states demonstrates the emergence of electronic liquid crystals [214,216]. Analogous to the stripe crystals at commensurate fractional fillings, electronic liquid crystals at incommensurate fillings also break the rotational symmetry spontaneously, but the translational symmetry of the lattice is restored. Here the parental $\nu = 1/2$ stripe crystal can be viewed as the building block for the continuum of stripe phases extending from $\nu = 1/3$ to $\nu = 2/3$ (Ref. [215]). Electron and hole doping from $\nu = 1/2$ induces electronic liquid crystals except at $\nu = 2/5, 3/5$, where stripe crystals again form at commensurate fillings. How this continuum of stripe phases melts to a Landau Fermi liquid by bandwidth tuning is an interesting direction to be explored by future studies.

3.3.5. Interacting local magnetic moments

The strong light-matter interactions and the spin/valley-dependent optical selection rules in 2D TMDCs also provide a very sensitive optical probe of the magnetic properties in TMDC moiré materials. Specifically, left- and right-handed light couple exclusively to the transitions at the K and K' valleys (or the up and down spins), respectively. When the TMDC is doped with charges, the difference in the left- and right-handed optical absorption, known as the magnetic circular dichroism (MCD), is proportional to the valley/spin polarization in the material. (Please refer to Ref. [19, 191] for reviews on the spin/valley-dependent optical selection rules in 2D TMDCs.) The use of circularly polarized light as the basis for measurement (instead of linearly polarized light) ensures that the signal is only sensitive to time-reversal symmetry breaking. As an estimate of the sensitivity in magnetic measurements, a typical MCD signal near the excitonic resonance in TMDC moiré materials is about 0.1 at magnetic saturation. Typical MCD noise level is about $10^{-6}/\sqrt{\text{Hz}}$ in polarization-modulation measurements. The number of magnetic moments within a diffraction-limited light spot is about 10^4 in moiré materials. The excitonic enhanced MCD is therefore sensitive down to the single moment level.

The high magnetic sensitivity opens the door to investigate the local moment physics in strongly correlated moiré systems described by the Hubbard model. For example, the charge degree of freedom is frozen in a Mott insulator in the strong correlation limit (see Section 3.3.2); only the spin degree of freedom remains; the low-energy physics is governed by the collective spin excitations [177]. As an attempt to become a metal, however, the electrons can lower its total energy (by $\sim t^2/U$ per particle) by hopping virtually to a nearest-neighbor site and back, effectively exchanging two electrons at adjacent sites [217]. The Mott insulator in the strong correlation limit is therefore approximately a lattice of interacting magnetic moments connected by a nearest-neighbor Anderson superexchange interaction $J \sim t^2/U$. The adjacent spins have to be anti-aligned in order to make the virtual hopping because of the Pauli exclusion principle; the magnetic interaction in a Mott insulator is antiferromagnetic.

The magnetic field dependent moiré exciton MCD at $\nu = 1$ of the WSe_2/WS_2 moiré lattice is shown in Figure 22(a) (Ref. [124]). The MCD saturates above ~ 1 T at low temperatures; the saturation magnetic field increases quickly with temperature because of thermal excitations of spins. Because the MCD is proportional to the sample magnetization, the zero field MCD slope is proportional to the magnetic susceptibility χ. The temperature dependence of χ is well described by the Curie-Weiss law $\chi^{-1} \propto T - T_{CW}$ (Figure 22(b)), which is a phenomenological manifestation of local moment physics in the system. Here $T_{CW} \propto J$ is the Curie-Weiss temperature; it provides a measure of the net magnetic interaction between the local moments. A Curie-Weiss temperature $T_{CW} \approx -1$ K can be extracted for the Mott insulator. The negative sign shows antiferromagnetic interaction, consistent with the expected Anderson superexchange. The small value reflects the localized Wannier wavefunction in the strong correlation limit, i.e. $t \ll U$.

Similar to the Mott insulating state, local moment physics is also expected for the Wigner-Mott insulating states at fractional lattice fillings. The low-energy physics of the Wigner-Mott insulators in the strong correlation regime can also be mapped to lattice spin models [219]. Interestingly, Curie-Weiss behavior is also observed at generic fillings $0 < \nu < 2$ (Ref. [124, 220]). These charge-compressible states with local moment physics could be exotic metals in the strong correlation limit [221]; they deserve further investigations. The filling factor dependence of the extracted Curie-Weiss temperature for WSe_2/WS_2 moiré is summarized in Figure 22(c). Starting from the Mott insulator at $\nu = 1$, doping above $\nu = 1$ turns the magnetic interaction from antiferromagnetic ($T_{CW} < 0$) to ferromagnetic ($T_{CW} > 0$) near $\nu = 1.2$. Its possible connection to Nagaoka ferromagnetism [222] in a triangular lattice deserves more in-depth investigations. On the other hand, doping below $\nu = 1$ in general strengthens the antiferromagnetic interaction, which is maximized near $\nu = 0.6$; the magnetic interaction becomes negligible at small fillings because the moments are far apart so that the exchange amplitude drops substantially.

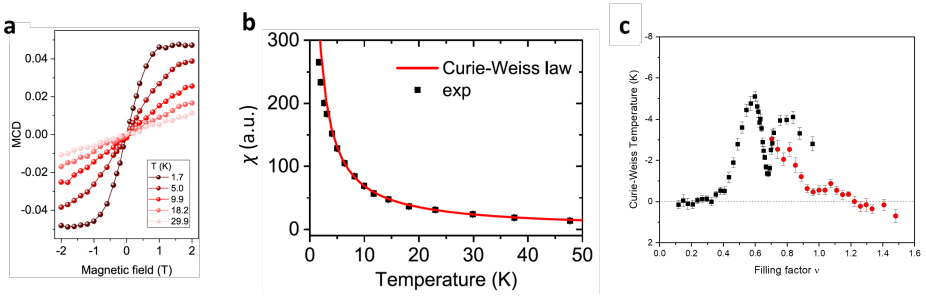

Fig. 22. Interacting local magnetic moments in a moiré lattice. (a) Magnetic-field dependence of spectrally integrated MCD at $\nu = 1$ and at representative temperatures. The MCD saturates above ~ 1 T at 1.7 K. The slope at zero magnetic field is extracted to represent the magnetic susceptibility. (b) Temperature dependence of the extracted magnetic susceptibility at $\nu = 1$. The red curves are Curie–Weiss fits from 6.4 K to 48 K, revealing a Curie-Weiss temperature of $-0.6 \pm 0.2K$. (c) Dependence of the extracted Curie-Weiss temperature on the filling factor. A transition to ferromagnetic interaction is seen near $\nu = 1.2$ and a substantially suppressed antiferromagnetic interaction is observed at $\nu = 2/3$. Red and black data points are results from analysis of the exciton Zeeman splitting and the exciton MCD, respectively. Panels (a) and (c) reprinted from [Y. Tang, K. Su, L. Li, Y. Xu, S. Liu, K. Watanabe, T. Taniguchi, J. Hone, C.-M. Jian, C. Xu, K. F. Mak, and J. Shan, Nat. Nanotechnol., 18, 233–237, 2023] [218]. Panel (b) reprinted from [Y. Tang, L. Li, T. Li, Y. Xu, S. Liu, K. Barmak, K. Watanabe, T. Taniguchi, A. H. MacDonald, J. Shan, and K. F. Mak, Nature, 579, 353–358, 2020] [124].

Intriguingly, a substantially suppressed antiferromagnetic interaction is also observed at the Wigner-Mott insulator at $\nu = 2/3$. The suppression is gone when the Wigner-Mott insulator is quenched by metallic screening of the long-range Coulomb repulsion from a metal gate close to the sample [220]. While the exact origin of the suppression is far from clear at this stage, the observation reflects the frustrated magnetic interaction in the system. In particular, because the moiré trapping potential, an approximate harmonic trapping potential, is rather smooth and shallow compared to the Coulomb potential of real atoms, the Wannier wavefunction is more extended spatially. This can substantially enhance the non-local magnetic interactions compared to the local interactions [223, 224]. At this stage, it is believed that the non-local ferromagnetic interactions compete strongly with the local antiferromagnetic interactions near $\nu = 2/3$, giving rise to the observed suppression in the magnetic interaction strength. However, it remains unclear why suppression of magnetic interactions is only observed at the $\nu = 2/3$ Wigner-Mott insulator but not at the other commensurate fractional fillings. More in-depth studies are required.

In addition to probing magnetic properties in the strong correlation limit $U \gg t$, MCD spectroscopy has also been employed to monitor the magnetic properties of semiconductor moiré materials through the bandwidth-controlled Mott transition [183]. In particular, the temperature-dependent magnetic susceptibility on both the insulating and the metallic sides has been measured through the transition. No signature of magnetic instability is observed; the magnetic susceptibility evolves smoothly through the transition down to about 5% of the Curie-Weiss temperature. The results are consistent with a bandwidth-controlled transition from a nonmagnetic Mott insulator to a Landau Fermi liquid. For comparison, a recent experiment on AB-twisted bilayer WSe_2 has reported the emergence of long-range antiferromagnetic ordering in a honeycomb lattice charge-transfer insulating state [190]. This difference may highlight the impact of geometric frustrations in long-range magnetic ordering.

4. Polaritons in TMDCs

Exciton-polaritons are quasiparticles that arise from strong coupling between excitons and cavity photons. They are formed when the exciton and cavity photon coupling strength is greater than the loss and decoherence of the system. Due to their half-exciton and half-photon nature, polaritons offer unique properties. Coulomb interaction between the excitonic components leads to strong optical nonlinearity, enabling correlated-many-body phenomena and optical logic devices. The photon component can be leveraged to obtain a small effective mass (4-5 orders of magnitude smaller than that of free electrons), enabling macroscopic quantum degeneracy, such as polariton condensates, superfluidity, vortices, and BEC-BCS state, at higher temperatures (up to room temperature). Taking advantage of nanofabrication techniques and laser shaping methods, various potential landscapes can be imprinted onto the polariton state through both its photonic and excitonic component. Therefore, polaritons can provide a new platform for complex circuitry, such as neuromorphic networks and quantum simulation. Lastly, polariton is a natural driven dissipative system, where non-Hermitian physics can be explored. Overall, exciton-polaritons combine coherence, nonlinearity, topology, and non-Hermitian physics into one platform, underpinning their potential not only in fundamental physics, but also in device concepts.

Monolayer TMDCs are direct bandgap semiconductors featuring robust excitons that interact strongly with photons, with binding energies two orders of magnitude larger and oscillator strengths one to two orders of magnitude larger than those of GaAs. Therefore, they are promising for exploring polaritonic physics and devices above the cryogenic temperatures. Moreover, 2D Van der Waals heterostructures (vdWHs) made of different 2D materials can be created and integrated with any optical structures without lattice matching constraints, allowing unprecedented flexibility for engineering the electronic properties and light-matter coupling. The most common types of cavities used for TMDC exciton polaritons include vertical cavities constructed with DBRs and slab photonic crystal cavities, which will be discussed in this section. Lastly, many unique properties of vdWHs, such as spin-valley locking, strong phonon–charge interactions, and moiré lattice in twisted bilayers, promise a wealth of novel phenomena and opportunities of new polariton devices.

4.1. Coupling between monolayer TMDC excitons and cavity photons

Light-matter interactions in TMDCs Controlling and enhancing the interactions between light and matter is essential to construct integrated photonic devices that use light to efficiently store and process information. Classically, light-matter interaction is a resonant interaction of charged particles and electromagnetic waves. This classical model is also known as the Lorentz oscillator model, where atoms are considered to be small harmonically oscillating dipoles and the driving force is the electromagnetic waves. Quantum mechanically, we can consider a transition between two atomic states, ψ_1 with energy E_1, and ψ_2 with energy E_2. The time-dependent wave functions are:

$$\psi_1(\boldsymbol{r}, t) = \psi_1(\boldsymbol{r}) e^{-iE_1 t/\hbar}, \tag{13}$$

$$\psi_2(\boldsymbol{r}, t) = \psi_2(\boldsymbol{r}) e^{-iE_2 t/\hbar}. \tag{14}$$

The average position of the atom is defined as:

$$\langle \boldsymbol{r}(t) \rangle = \int \psi^*_{\text{tot}} \boldsymbol{r} \psi_{\text{tot}} d^3\boldsymbol{r}, \tag{15}$$

where ψ_{tot} is the superposition of ψ_1 and ψ_2 ($\psi_{\text{tot}} = \psi_1 + \psi_2$). The strength of the light-matter interaction depends on the transition dipole moment:

$$\langle \boldsymbol{p} \rangle = e \langle \boldsymbol{r} \rangle, \tag{16}$$

which has a matrix component:

$$e \int \psi_2^*(\boldsymbol{r})\ \boldsymbol{r}\ \psi_1(\boldsymbol{r}) d^3\boldsymbol{r}, \tag{17}$$

and an oscillation component:

$$e^{-i(E_1-E_2)t/\hbar}. \tag{18}$$

We can see that an incident electromagnetic field resonant with the transition energy $(E_2 - E_1)$ can put the atom into a superposition state of ψ_1 and ψ_2, and the atom can oscillate between the two states and emit electromagnetic radiation.

As the dipole radiates, the total power decays at a rate called the radiative decay rate (γ_{rad}). There are also non-radiative decay channels and decay rate (γ_{nr}). As the dipoles collide with each other, they can pick up a phase and can decrease the macroscopic polarization ($\boldsymbol{P}$). This is called the dephasing rate ($1/T_2'$). All of these decay channels determine the total polarization decay rate (γ).

We can solve the equation of motion for the macroscopic polarization and define:

$$\boldsymbol{P} = \epsilon_0 \chi \boldsymbol{E}. \tag{19}$$

$\boldsymbol{E}$ is the incident electric field with frequency ω, and χ is the electric susceptibility:

$$\chi = \frac{Ne^2}{m\epsilon_0} \frac{1}{(\omega_0^2 - \omega^2) + 2i\gamma\omega}, \tag{20}$$

where N is the number of dipoles and ω_0 is the resonant frequency. The real part of χ is a dispersive function and describes the real refractive index of the material. The imaginary part is a Lorentzian function and describes the absorption of the material [225]. The susceptibility of a material contains information about the strength of the light-matter interaction and the optical properties.

Aside from the light-matter interaction that is intrinsic to the material, we can use external methods to control and enhance the interactions. Cavity provides a powerful method to achieving this.

Weak exciton-photon coupling In the weak coupling regime, the photon escapes the cavity before being resonantly reabsorbed by the exciton, and the light-matter coupling rate is smaller than the decay rate of the system. Therefore, the decay of exciton is irreversible and the cavity only alters the radiative lifetime of the exciton. When the exciton energy is resonant with the cavity mode energy, the optical density of states increases and the spontaneous decay rate of the exciton is enhanced. On the other hand, when the exciton energy is off-resonant, the emission rate decreases.

The spontaneous emission rate of a dipole emitter follows the Fermi's golden rule:

$$\Gamma_{i\to f} = \frac{2\pi}{\hbar^2} |\boldsymbol{p} \cdot \boldsymbol{E}(\boldsymbol{r}, t)|^2 \rho(\omega), \tag{21}$$

where $|\boldsymbol{p} \cdot \boldsymbol{E}(\boldsymbol{r}, t)|^2$ is the transition dipole matrix element and $\rho(\omega)$ is the photon density of states. For photons that have a linear dispersion relation ($E = \hbar\omega = \hbar ck$), the 3D density of states in vacuum is:

$$\rho_{\text{vac}}(\omega) = \frac{\omega^2 V n^3}{\pi^2 c^3}, \tag{22}$$

where ω is the angular frequency of light, V is the mode volume, and n is the refractive index. On the other hand, the density of states in a cavity is modified and can be calculated using a new

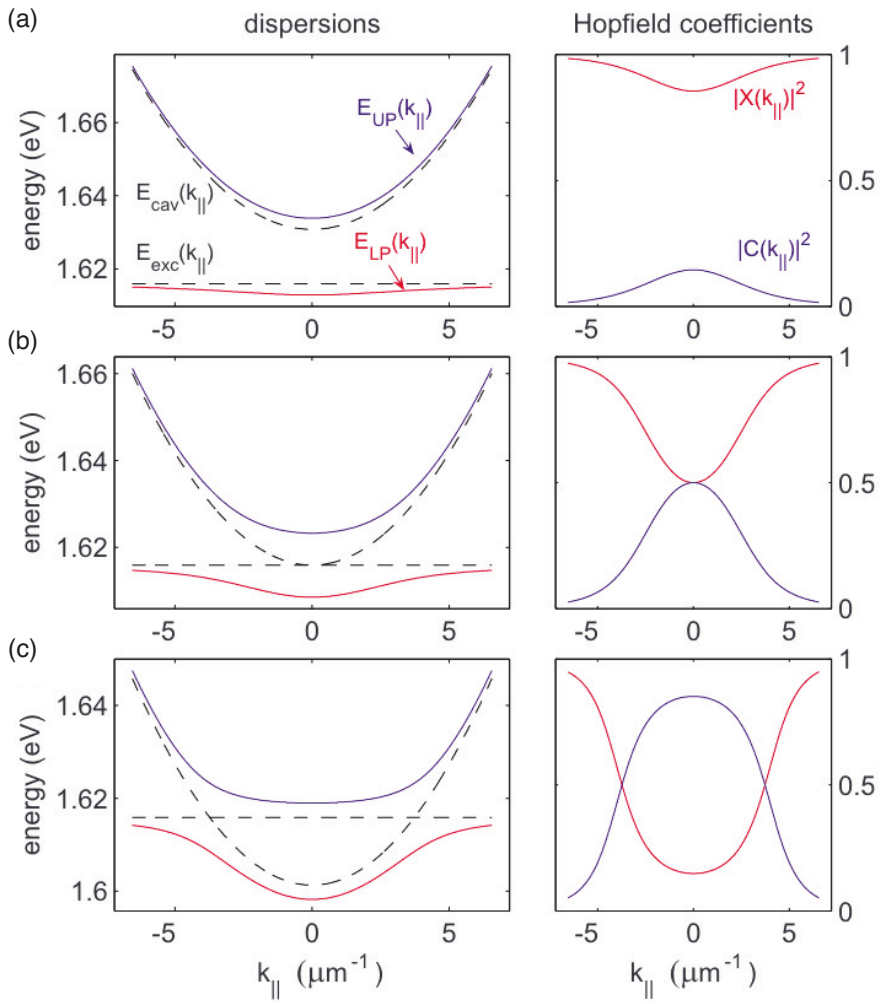

Fig. 23. Polariton energy dispersion and Hopfield coefficients at different detunings. The detunings are: (a) $+2\hbar\Omega$, (b) 0, and (c) $-2\hbar\Omega$. Reprinted from [H. Deng, H. Haug, and Y. Yamamoto, Rev. Mod. Phys., 82, 1489–1537, 2010] [46].

cavity wave vector. The cavity density of states is [226]:

$$\rho_{\text{cav}}(\omega) = \frac{2}{\pi} \frac{\Delta\omega_c^2}{4(\omega - \omega_c)^2 + \Delta\omega_c^2}. \tag{23}$$

Recall $Q = \omega_c/\Delta\omega_c$. At resonance, the ratio of spontaneous emission rates inside the cavity and in the vacuum can be written as:

$$F_P = \frac{\Gamma_{\text{cav}}}{\Gamma_{\text{vac}}} = \frac{3}{4\pi^2}\left(\frac{\lambda_c}{n}\right)^3 \frac{Q}{V}, \tag{24}$$

where λ_c is the resonance wavelength. This is also known as the Purcell factor.

Strong exciton-photon coupling In the strong coupling regime, the photon can be emitted and reabsorbed by excitons coherently and reversibly, and the light-matter coupling rate is larger than

the decay rate of the system. In other words, the photon is reabsorbed by the exciton before it escapes the cavity. In the strong coupling regime, the energy eigenstates of excitons and cavity photons mix and hybridize to form new energy eigenstates that are a superposition of the exciton and cavity modes. Thus, the new elementary excitations are called exciton-polaritons, which are quasi-particles that result from strongly coupled light and matter. Experimentally, strong coupling is demonstrated by measuring the anti-crossing of the polariton energies as the exciton and cavity mode energies cross, through reflectivity or PL measurements.

The Hamiltonian of exciton-polaritons in a microcavity is given by:

$$\hat{H}_{\text{pol}} = \hat{H}_{\text{cav}} + \hat{H}_{\text{exc}} + \hat{H}_{\text{I}}, \tag{25}$$

where $\hat{H}_{\text{cav}}$ is the cavity, $\hat{H}_{\text{exc}}$ is the exciton, and $\hat{H}_{\text{I}}$ is the interaction Hamiltonians. Using the rotating wave approximation, the Hamiltonian of the exciton-polariton system can be written in the matrix form:

$$\hat{H}_{\text{pol}} = \begin{pmatrix} \hat{a}^\dagger & \hat{e}^\dagger \end{pmatrix} \begin{pmatrix} E_{\text{cav}} - i\gamma & g \\ g & E_{\text{exc}} - i\kappa \end{pmatrix} \begin{pmatrix} \hat{a} \\ \hat{e} \end{pmatrix}$$

Where, $\hat{a}^\dagger$ and $\hat{e}^\dagger$ are creation operators of photon and exciton modes. E_{cav} and E_{exc} are the energies of the uncoupled exciton and photon respectively, with the corresponding out coupling and decay rate described by γ and κ. g is the coupling strength. The energies of polaritons, which are the eigenenergies of the Hamiltonian, are deduced from the diagonalization procedure as:

$$\begin{aligned} E_{LP,UP}(k_\parallel) =& \frac{1}{2}\left[E_{\text{exc}} + E_{\text{cav}} + i(\kappa + \gamma)\right] \\ & \pm \sqrt{g^2 + \frac{1}{4}\left[E_{\text{exc}} - E_{\text{cav}} + i(\kappa - \gamma)\right]^2}. \end{aligned} \tag{26}$$

The difference between cavity and exciton energies is referred to as the detuning:

$$\Delta E(k_\parallel) = E_{\text{cav}}(k_\parallel, k_z) - E_{\text{exc}}(k_\parallel). \tag{27}$$

$X_{k_\parallel}$ and $C_{k_\parallel}$ are Hopfield coefficients and they describe the exciton and photon fraction in lower and upper polaritons. They are defined as [227]:

$$|X_{k_\parallel}|^2 = \frac{1}{2}\left(1 + \frac{\Delta E(k_\parallel)}{\sqrt{\Delta E(k_\parallel)^2 + 4\hbar^2\Omega^2}}\right) \tag{28}$$

$$|C_{k_\parallel}|^2 = \frac{1}{2}\left(1 - \frac{\Delta E(k_\parallel)}{\sqrt{\Delta E(k_\parallel)^2 + 4\hbar^2\Omega^2}}\right), \tag{29}$$

where $|X_{k_\parallel}|^2 + |C_{k_\parallel}|^2 = 1$. The polariton energy dispersions and corresponding Hopfield coefficient at different energy detunings are shown in Figure 23.

When the uncoupled exciton and cavity photon are at the same energy $E_{exc} = E_{cav}$, LP and UP energies have the minimum separation $2\hbar\Omega = E_{UP} - E_{LP} = 2\sqrt{g^2 - \frac{1}{4}(\gamma - \kappa)^2}$,which is the Rabi splitting. To reach strong coupling, reversible energy exchange between the exciton and photon modes is required, and the two splitted modes need to be spectrally separable. The minimum mode-splitting needs to be greater than the sum of the half linewidths of the modes.

$$2\hbar\Omega > \gamma + \kappa, \text{ or, } g > \sqrt{(\gamma^2 + \kappa^2)/2}. \tag{30}$$

Exciton-polaritons possess properties of both excitons and photons so their properties can be determined by the exciton and photon fractions, or the Hopfield coefficients ($|X|^2$, $|C|^2$). The polariton effective mass is:

$$\frac{1}{m_{\mathrm{LP}}} = \frac{|X|^2}{m_{\mathrm{exc}}} + \frac{|C|^2}{m_{\mathrm{cav}}} \tag{31}$$

$$\frac{1}{m_{\mathrm{UP}}} = \frac{|C|^2}{m_{\mathrm{exc}}} + \frac{|X|^2}{m_{\mathrm{cav}}}, \tag{32}$$

where X and C are Hopfield coefficients, m_{exc} is the exciton effective mass, and m_{cav} is the cavity effective mass. The polariton radiative lifetime is:

$$\gamma_{\mathrm{LP}} = |X|^2\gamma_{\mathrm{exc}} + |C|^2\gamma_{\mathrm{cav}} \tag{33}$$

$$\gamma_{\mathrm{UP}} = |C|^2\gamma_{\mathrm{exc}} + |X|^2\gamma_{\mathrm{cav}}, \tag{34}$$

where γ_{exc} is the exciton lifetime and γ_{cav} is the cavity photon lifetime.

Selection of Materials From the perspective of materials, the four types of well known TMDCs have been employed separately to demonstrate strong coupling with cavity photons. To obtain well resolved Rabi splitting, monolayer prepared by mechanical-exfoliation method is preferred compared to CVD grown monolayers because of reduced inhomogeneous linewidth. Monolayers encapsulated with few-layer hBN exhibit even narrower linewith approaching the limit of homogeneous linewidth. It has been shown that monolayer WS_2 prepared by the mechanical exfoliation provides the narrowest exciton linewidth at room temperature. Therefore, WS_2 based polariton systems exhibit the most well resolved splitting at room temperature over the other TMDCs. $MoSe_2$ typically exhibits the narrowest linewidth at low temperature, and has been used to investigate polariton lasing at low temperature [228]. MoS_2 and WSe_2 possess very strong valley polarization and valley coherence, and are integrated with cavities to investigate the valleytronics of polaritions, which will be discussed in details in the following sections.

4.2. Cavities for TMDC polaritons

A cavity is an optical resonator that confines and stores light at resonant frequencies. A microcavity has size that is comparable to the wavelength of light [229]. Microcavities confine light by reflecting it back when it reaches the boundary of the cavity. The microcavities used for semiconductors rely primarily on the photonic band gap and internal reflection. Much like an electronic band gap, photonic band gap is created when a periodic modulation of the dielectric material results in band folding and opens up a band gap. Cavities that utilize internal reflection are often made with high index materials and rely on the reflection of light at the interface between a dielectric and the surrounding medium to trap light within the cavity.

Optical resonators are characterized by two main parameters: the quality factor and mode volume. The quality factor (Q) is a measure of how well the light stays confined in the cavity. In another words:

$$Q = 2\pi\frac{\text{stored energy}}{\text{energy loss per cycle}}, \tag{35}$$

which is equivalent to:

$$Q = \frac{\omega_c}{\Delta\omega_c}, \tag{36}$$

where ω_c is the resonance frequency, and $\Delta\omega_c$ is the spectral linewidth, or the FWHM, of the resonator modes [230]. A microcavity with a high Q-factor can allow longer photon lifetime, which is important for strong coupling.

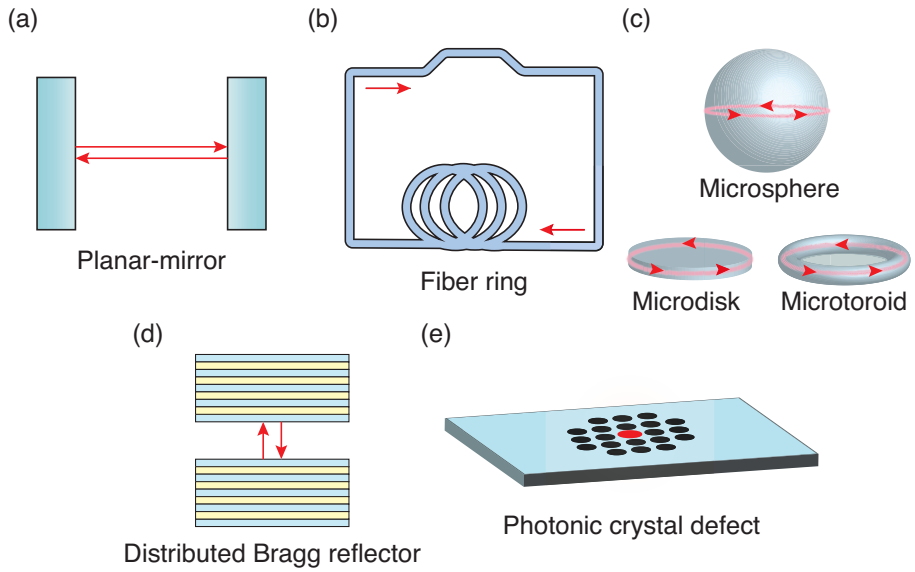

Fig. 24. Types of cavities. (a) Planar-mirror cavity, (b) fiber ring cavity, (c) whispering gallery mode cavities, (d) DBR cavities, and (e) photonic crystal defect cavity.

The mode volume is the volume occupied by the optical mode:

$$V_{\text{eff}} = \frac{\int_V \epsilon(\boldsymbol{r})|\boldsymbol{E}(\boldsymbol{r})|^2 d^3\boldsymbol{r}}{\max[\epsilon(\boldsymbol{r})|\boldsymbol{E}(\boldsymbol{r})|^2]}, \tag{37}$$

where ϵ_r is the dielectric constant, $|\boldsymbol{E}(\boldsymbol{r})|$ is the electric field strength, and V is a quantization volume encompassing the resonator [231].

For a given material, where the exciton oscillator strength is fixed, cavity with smaller mode volume and higher quality factor will be highly desirable to obtain exciton polaritons with large coupling strength and strong coherence. They can be characterized by the Rabi splitting and linewidth in the spectra of polaritons. There are many different types of cavity configurations that are available for study, including mirror cavities, fibers or waveguides, whispering gallery modes, DBRs, and photonic-crystal defects (Figure 24). Strong exciton-photon coupling have been demonstrated in TMDCs monolayers integrated with various types of optical structures including dielectric DBRs cavities, Tamm plasma cavities, full metal cavities, nano plasmonics, and dielectric photonic crystals. In this section, we will introduce some of these cavity structures.

4.2.1. DBR cavities

Theory DBR microcavities are one of the most widely used cavities for semiconductors because they have high reflectivity. DBR is a periodic structure composed of alternating high and low refractive index materials, each with an optical thickness of $\lambda/(4n)$, where n is the index of refraction. Considering a single dielectric layer of thickness $\lambda/(4n)$, the optical path difference of incident light reflected off of the bottom surface is $\lambda/(2n)$ (which results in a total phase shift of π), and therefore adds in phase with the light reflected off of the top surface (which experiences a π phase shift), maximizing the reflectivity.

The reflectivity of the DBR stack can be calculated using the transfer matrix method. First, we consider a single layer of material with index of refraction n_1 and thickness l, with electromagnetic waves incident from a material with index n_0, and the material is on a substrate with index of refraction n_s. A schematic illustration is shown in Figure 25. For simplicity, we consider

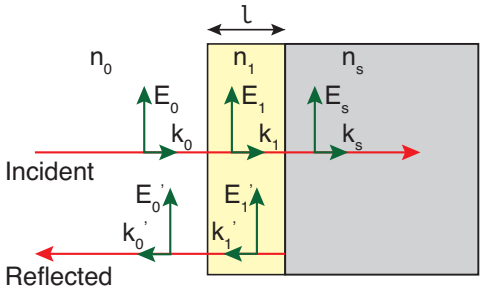

Fig. 25. Electric field (E) and wave vectors (k) for a single dielectric layer on a substrate. The index of refraction of the incident material is n_0, dielectric material is n_1, and substrate is n_s. l is the thickness of the dielectric material.

normally incident light. The boundary conditions dictate that the tangential component of electric ($\vec{E}$) and magnetic ($\vec{H}$) fields must be continuous across the boundary. Along the first interface:

$$E_0 + E_0' = E_1 + E_1' \tag{38}$$
$$H_0 - H_0' = H_1 - H_1' \tag{39}$$
$$\text{or } n_0 E_0 - n_0 E_0' = n_1 E_1 - n_1 E_1'. \tag{40}$$

At the second interface,

$$E_1 e^{ikl} + E_1' e^{-ikl} = E_s \tag{41}$$
$$H_1 e^{ikl} - H_1' e^{-ikl} = H_s \tag{42}$$
$$\text{or } n_1 E_1 e^{ikl} - n_1 E_1' e^{-ikl} = n_s E_s. \tag{43}$$

The above equations can be simplified to:

$$1 + \frac{E_0'}{E_0} = \left(\cos kl - i\frac{n_s}{n_1}\sin kl\right)\frac{E_s}{E_0} \tag{44}$$
$$n_0 - n_0\frac{E_0'}{E_0} = (-in_1 \sin kl + n_s \cos kl)\,\frac{E_s}{E_0}. \tag{45}$$

Re-writing it in matrix form:

$$\begin{bmatrix} 1 \\ n_0 \end{bmatrix} + \begin{bmatrix} 1 \\ -n_0 \end{bmatrix}\frac{E_0'}{E_0} = \begin{bmatrix} \cos kl & -\frac{i}{n_1}\sin kl \\ -in_1 \sin kl & \cos kl \end{bmatrix}\begin{bmatrix} 1 \\ n_s \end{bmatrix}\frac{E_s}{E_0}, \tag{46}$$

which can be further simplified to:

$$\begin{bmatrix} 1 \\ n_0 \end{bmatrix} + \begin{bmatrix} 1 \\ -n_0 \end{bmatrix} r = M \begin{bmatrix} 1 \\ n_s \end{bmatrix} t, \tag{47}$$

where r is the reflection coefficient, t is the transmission coefficient, and M is the transfer matrix:

$$M = \begin{bmatrix} \cos kl & -\frac{i}{n_1}\sin kl \\ -in_1 \sin kl & \cos kl \end{bmatrix}. \tag{48}$$

For N layers the transfer matrix is:

$$M = M_1 M_2 M_3 \cdots M_N = \begin{bmatrix} A & B \\ C & D \end{bmatrix}, \tag{49}$$

and the reflection coefficient is:

$$r = \frac{An_0 + Bn_s n_0 - C - Dn_s}{An_0 + Bn_s n_0 + C + Dn_s}. \tag{50}$$

Now, we consider a pair of layers, one with a low index n_l and one with a high index n_h, each with $\lambda/(4n)$ layer thickness. Here, kl is $\pi/2$ so the transfer matrix is:

$$\begin{bmatrix} 0 & -\frac{i}{n_l} \\ -in_l & 0 \end{bmatrix} \begin{bmatrix} 0 & -\frac{i}{n_h} \\ -in_h & 0 \end{bmatrix} = \begin{bmatrix} -\frac{n_h}{n_l} & 0 \\ 0 & -\frac{n_l}{n_h} \end{bmatrix}. \tag{51}$$

If the DBR has N pairs, the transfer matrix is:

$$M = \begin{bmatrix} \left(-\frac{n_h}{n_l}\right)^N & 0 \\ 0 & \left(-\frac{n_l}{n_h}\right)^N \end{bmatrix}. \tag{52}$$

The reflectance of the DBR is:

$$R = |r|^2 = \left[\frac{(n_0/n_s)(-n_l/n_h)^{2N} - 1}{(n_0/n_s)(-n_l/n_h)^{2N} + 1}\right]^2 \tag{53}$$

[232]. We can see that more layers and higher refractive index contrast result in higher reflectance of the DBR mirror. A DBR has a broad, high reflectivity band called the stop band corresponding to a 1D photonic band gap. The width of the stop band is [233]:

$$\delta\lambda = \lambda_0 \frac{4}{\pi} \arcsin\left(\frac{n_h - n_l}{n_h + n_l}\right), \tag{54}$$

where λ_0 is the center wavelength of the stop band. Higher refractive index contrast results in a wider stop band. An example of a 1D DBR reflection spectrum calculated using the transfer matrix method is shown in Figure 26.

To form a cavity, two high-reflectance DBRs are stacked together with a spacer layer in between. The optical thickness of the spacer layer is a multiple of $\lambda_c/2$, where λ_c is the cavity resonance wavelength (Figure 27(a)). A plot of the refractive index and calculated electric field intensity is shown in Figure 27(b). In essence, the DBR cavity is a Fabry-Perot etalon with a sharp transmission peak at the resonance wavelength given by the airy function. The transmission is [232]:

$$T = \frac{(1 - R_1)(1 - R_2)}{[1 - \sqrt{R_1 R_2}]^2 + 4\sqrt{R_1 R_2}\sin^2(\phi/2)}, \tag{55}$$

where R_1 and R_2 is the reflectivity of the two mirrors and ϕ is the phase difference that light acquires during a cavity round trip. The cavity resonance is a dip in the reflection spectrum, as shown in Figure 27(c).

The cavity dispersion energy for a planar DBR cavity is defined as [234]:

$$E_{\text{cav}} = \frac{\hbar c}{n_c}\sqrt{k_\parallel^2 + k_z^2}, \tag{56}$$

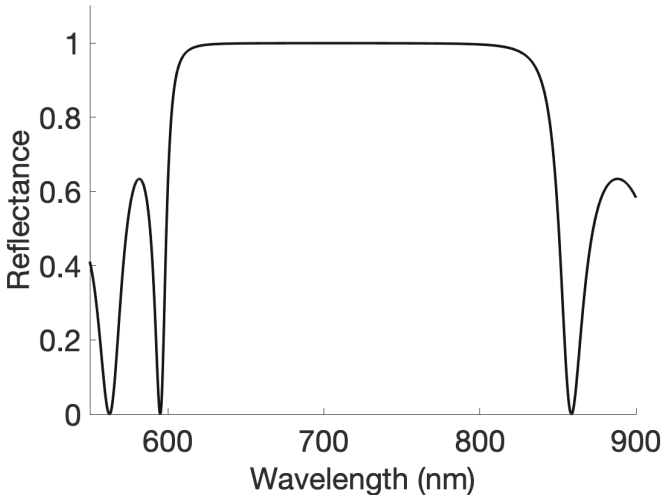

Fig. 26. Reflection spectrum of a DBR mirror calculated using the transfer matrix method.

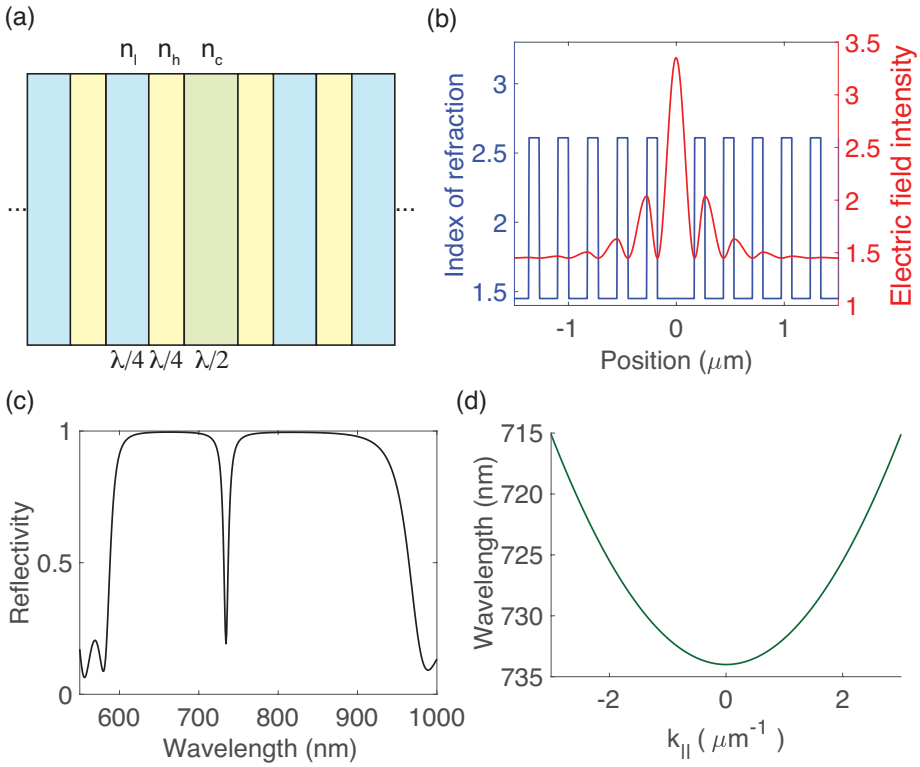

Fig. 27. DBR microcavity. (a) Simplified schematic of the planar DBR microcavity structure. Each of the DBR layers has a $\lambda/4$ optical thickness with alternating high-index (n_h) and low-index (n_l) materials. The cavity optical length is $\lambda/2$ and the cavity index of refraction is n_c. (b) Cavity index of refraction and electric field intensity profiles. (c) Reflectivity spectrum of the DBR cavity calculated by the transfer matrix method. (d) Calculated angle-resolved energy dispersion of the DBR cavity.

where n_c is the cavity index of refraction, and $k_\parallel$ (k_z) is the wave vector parallel (perpendicular) to the mirror layers. In the limit where $k_\parallel << k_z$, the above equation can be simplified as:

$$E_{\text{cav}} \approx \frac{\hbar c}{n_c} k_z + \frac{\hbar^2 k_\parallel^2}{2m_{\text{cav}}}, \tag{57}$$

where the cavity effective mass is:

$$m_{\text{cav}} = \frac{2\pi\hbar}{\lambda_c c}. \tag{58}$$

Figure 27(d) shows the plotted cavity dispersion.

DBR cavities for TMDCs DBR cavities are attractive for TMDC exciton-polariton devices because of its robust structure and relatively simple cavity modes that can be simulated and measured. To ensure a high-quality microcavity device, integrating the active media with the cavity requires careful and methodical fabrication steps to minimize defects and strain introduced during the process. This is especially important for exciton-polariton devices because reducing the loss in the system is critical for strong coupling. For conventional III-V semiconductors such as GaAs, the DBR mirrors are grown monolithically, along with the active quantum well layer.

Exciton-polaritons with TMDC materials and DBR cavities have been demonstrated in recent years using a variety of different cavity fabrication methods. Typically, the TMDC active layer is mechanically transferred or grown onto the bottom DBR and the top DBR encapsulates the TMDC layer. There are several different methods of transferring the top DBR. First method is direct deposition of the top DBR on top of the TMDC material [235, 236]. This method can require high processing temperatures which can induce strain and lower the sample optical quality. Another method is to use a open cavity system with the top DBR mounted on a piezo-controlled stage. In addition to retaining the TMDCs as pristine, the cavity resonance can be tuned flexibly and the quality factor was raised to 1500 [237]. However, the mode volume is larger than the compact DBR cavity, resulting in a smaller Rabi splitting. Most recently, a new method to prepare a double DBR cavity is developed, where the top DBR can be stacked on to monolayer TMDCs by a dry-transfer technique. Such cavities show cavity quality factor up to 10000, and retain the small mode volume of a compact DBR cavity as well [238, 239].

4.2.2. Dielectric photonic crystal and grating cavities

Dielectric photonic crystals (PC), with high quality factor, small mode volume, and unprecedented tuning flexibility, have attracted more interests to explore light matter interaction with TMDCs.

The first verification of strong coupling between a dielectric photonic crystal cavity and TMDCs excitons is realized in a one dimensional subwavelength grating [240]. A photonic grating cavity utilizes a guided mode resonance (GMR) and is a slab of dielectric material patterned with a sub-wavelength periodic modulation along the in-plane direction. Essentially, it is a slab waveguide with a periodic pattern. The waveguide supports a guided mode and the periodic pattern tunes the mode dispersion and couples light in and out of the waveguide.

A slab waveguide is a high index medium (the 'slab') sandwiched between lower index layers (the 'cladding'), as illustrated in Figure 28. Then, total internal reflection traps light within the wave guide. Solving the electromagnetic wave equation from Maxwell's equations, we can obtain a solution for the S-polarized waves (in-plane, perpendicular to the wave propagation direction), which is an exponential function in the cladding and a oscillatory function in the slab:

$$E_{\text{cladding}} = E_c e^{\pm\alpha x}, \text{ where } \alpha = \sqrt{\beta^2 - n_0^2 k_0^2}, \tag{59}$$

$$E_{\text{slab}} = E_s \cos(hx) + E_a \sin(hx), \text{ where } h = \sqrt{n_h^2 k_0^2 - \beta^2}. \tag{60}$$

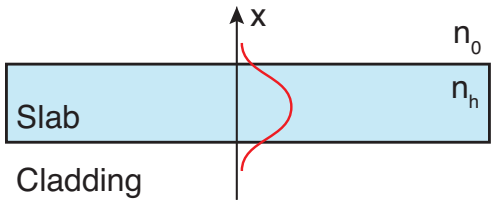

Fig. 28. Slab waveguide. n_0 is the index of refraction of the cladding and n_h is the index of the slab. Red solid line is an illustration of the electric field profile of a symmetric mode.

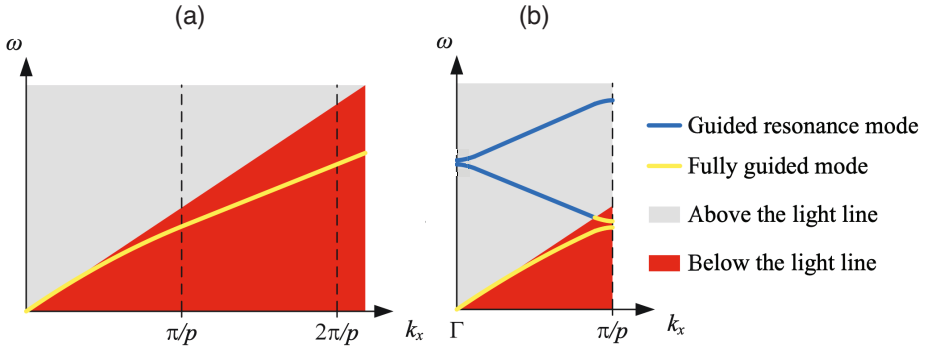

Fig. 29. Guided resonance mode of (a) a slab waveguide versus (b) a patterened photonic grating mode. p is the periodicity of the photonic grating. Reprinted with permission from [J. O. Grepstad, M. M. Greve, B. Holst, I.-R. Johansen, O. Solgaard, and A. Sudbø, Opt. Express, 21, 23640–23654, 2013] [241].

β is the total propagation constant, n_0 is the refractive index of the cladding, $k_0 = \omega^2/c^2$ is the vacuum wave vector, and n_h is the refractive index of the slab. At the edges of the slab boundary, the fields must be continuous. We can see that a higher index contrast between the slab and the cladding results in more confinement of the electromagnetic fields within the slab. The electric field of the resonant mode is confined in the slab and exponentially decays in the cladding region. Therefore, for a realistic device, it is important to place the active medium as close to the waveguide as possible and also have a slab that is thick enough to support a guided mode but not too thick as to reduce the coupling between the mode and the active medium.

The GMR in a slab waveguide is not optically accessible and lies outside of the light cone. The periodic patterning of the slab folds the resonance band and makes the guided mode optically accessible (Figure 29). Because the periodicity is present only along one of the directions, the guided mode is anisotropic and has polarization dependence. On resonance, the light must be trapped inside of the cavity and not interfere destructively with each other. Thus, the phase difference between the diffracted and transmitted wave is π and total destructive interference of transmitted light occurs at the resonance [242]. Experimentally, the resonance mode shows up as a peak in the reflectance spectrum. The line shape of the reflectance peak is an anti-symmetric Fano resonance due to the interference between the portion of the light that goes directly through the slab and the light that couples to the guided mode before decaying [243].

2D materials can be incorporated simply by exfoliation onto the top of the PC. For a given

monolayer TMDC, the Rabi splitting that can be achieved is mainly determined by the slab thickness, which controls the field overlap between the exciton and GMRs mode. Numerical simulation indicates that strong coupling can be achieved in a wide range of slab thickness [244]. Such a design has also been demonstrated experimentally, and dispersion of exciton polaritons have been observed in a WSe_2-PC structure at low temperature and a WS_2-PC structure at room temperature [240]. Interestingly, boundary in continuum state in the 1D grating has also been utilized to couple with TMDCs exciton, where strong polariton nonlinearity was observed [245]. The 1D grating is extended to a 2D photonic crystal [246], and additional degree of freedom in 2D allows more flexible mode engineering. By integrating monolayers with a topological hexagonal photonic crystal, helical topological polaritons are demonstrated [247, 248].

4.2.3. Tamm plasma cavities

Tamm plasma cavities and full metal cavities are constructed by replacing one or both DBRs with metal mirrors. They can reduce the mode volume and simplify the fabrication process, but can result in a lower quality factor. Plasmonic cavities are nanoscale metalic structures that can further reduce the mode volume by overcoming the diffraction limit, and thereby can achieve the largest Rabi splitting. Various single plasmonic nanocavities, including nanorods [249–251] and nanoprisms [252, 253] have been used to couple with TMDCs excitons, and the Rabi splitting detected by the scattering spectra is above 100 meV, establishing strong coupling.

An interesting topic in plasmonic-TMDCs polariton hybrid systems is to reduce the number of excitons involved in the coupling, paving the way to quantum nonlinearity in TMDCs polariton systems [254]. A hybrid plasmonic structure comprising of a nanoparticle and a metal mirror allow small mode volumes and high field confinements. Such hybrid plasmonic structures have been integrated with monolayer TMDCs, and the effective exciton number contributing to coupling is reduced to single-digit level [255]. To improve the quality factor of plasmonic cavities and retain the small mode volume at the same time, plasmonic arrays can be integrated with TMDC monolayers [256–259].

4.3. Special properties of TMDC polaritons

4.3.1. Valleytronics of TMDCs polaritons

The spin-valley properties and the consequent valley-dependent optical selection rules give TMDC excitons an additional degree of freedom for valleytronics applications. This valley degree of freedom of excitons can be transferred to polaritons via strong light matter interactions. In addition, valley coherence of TMDCs excitons, an important property for manipulating and controlling optical information, is a result of coherent superposition of the $K^{\pm}$ exciton states, and can be transferred to polaritons [237, 260] (Figure 30 (a,b)).

The valley polarization of excitons, manifested as the circular polarization of the PL emission, is enhanced in the strong coupling regime. For excitons, the relatively low degree of polarization in PL mainly results from the valley depolarization rate being faster than the radiative rate. These two competing processes can be controlled in the polariton system. The spatially extended polariton wavefuction can reduce the valley depolarization induced by defects on the nanometer-scale [261]. In addition, the total decay rate of polaritons is enhanced through the cavity

4.3.2. Nonlinearity in TMDCs polaritons

Another important property of excitons and polaritons is their nonlinearity. Excitons show nonlinear responses to both the intensity of a coherent laser and the density of carriers. The optical nonlinearity results from the exciton-photon coupling and thus scales with the optical dipole moment of the material and is greatly enhanced in TMDCs due to the large oscillator strength of intralayer excitons. The strong optical nonlinearity has manifested in strong optical Stark effect. In monolayer TMDC on the DBR, a Stark shift of a few meV, corresponding to an

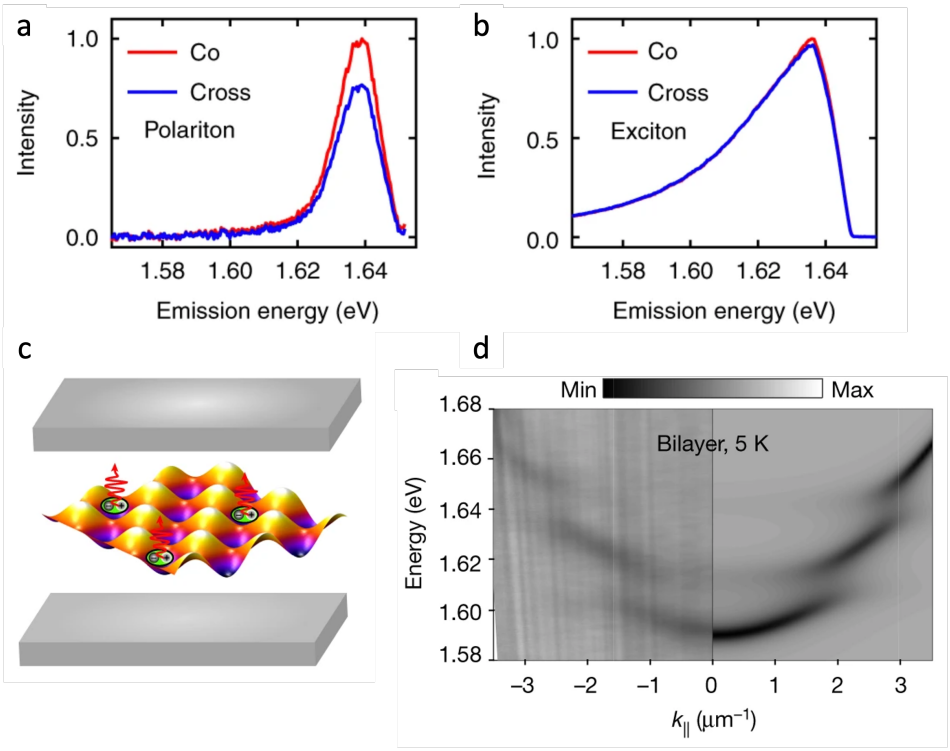

Fig. 30. Special properties of TMDC polaritons. (a,b) Valley coherence of polariton (a) and exciton (b) shown as a measurement of co- and cross- polarized PL intensities. Reprinted from [260], CC BY 4.0. (c) Schematic diagram of a moiré polariton structure. (d) Angle-resolved reflection spectrum of the moiré polariton. Reprinted from [L. Zhang, F. Wu, S. Hou, Z. Zhang, Y.-H. Chou, K. Watanabe, T. Taniguchi, S. R. Forrest, and H. Deng, Nature, 591, 61–65, 2021] [111].

effective magnetic field up to 40 T was measured [73]. The nonlinear response to the carrier density results from interactions among the carriers. It is often expressed in terms of band renormalization, exciton-exciton interaction dominated by contact interactions, and phase space filling due to the Pauli exclusion principle. All three effects generally scale with the exciton Bohr radius. In the TMDCs system, the exciton Bohr radius is about 1 nm, as opposed to ~ 10 nm in GaAs, and therefore the resulting nonlinear interaction strength is much smaller than the GaAs system.

Polaritons show nonlinear response due to their exciton component, but modulated by the exciton fraction and exciton-cavity coupling. The exciton fraction results in a proportionally reduced nonlinearity in polaritons. However, the nonlinear response is mostly commonly measured through the shift the resonance and should be compared with the linewidth of the resonance. Polariton linewidth has contributions from both the exciton and the cavity component and, in high-Q cavities, can be substantially smaller than the exciton linewidth. Therefore nonlinear responses that are difficult to measure in excitonic systems can become measurable in polaritons.

The polariton nonlinearity is also modulated by the exciton-cavity coupling, which can result in a nonlinear response much stronger than that of the excitons through phase space filling. Phase space filling leads to reduced exciton oscillator strength, which simply saturates the nonlinear response for exciton systems. In contrast, for polaritons, the reduced oscillator strength leads

to reduced vacuum Rabi-splitting and in turn a blue (red) shift of the lower (upper) polariton resonance, producing effectively an additional nonlinear response. This additional nonlinearity still scales with the exciton Bohr radius and therefore is still weaker in TMDC polaritons than polaritons in conventional materials.

To increase the polariton nonlinearity in TMDC systems, a variety of unconventional excitonic states have been investigated. Rydberg 2s excitons feature a larger exciton Bohr radius than 1s excitons and thus a stronger nonlinearity [42]. Charged polaritons, such as trion or polaron polaritons [27, 262], have stronger direct Coulomb interaction between the charges and are predicted to exhibit an unconventional polariton blockade at high enough densities [28]. Interlayer excitons in homobilayers have a finite but sufficiently small electron-hole separation, therefore they feature dipole-dipole interactions between the finite out-of-plane permanent dipole moment while retaining high enough oscillator strength to establish strong coupling [263, 264].

The increase in nonlinearity in these polariton system comes at the expense of reduced binding energy of the excitonic transition, or stability and operating temperature of the excitonic and corresponding polaritonic states. Interestingly, moiré superlattices provide a new route to mitigate this fundamental trade-off of quantum-well exciton based polariton systems.

4.3.3. Moiré polariton and its nonlinearity

Moiré superlattices provide a powerful tool to engineer the energies, wavefunctions, and optical selection rules of excitons, because they provide a lattice potential on the length and energy scale of those of the excitons. When excitons couple with cavity modes to form polaritons, however, the polariton properties are expected to become less sensitive to fluctuations on the exciton's length and energy scales and the effect of the moiré superlattice is obscured. Interestingly, contrary to this intuition, it was shown that moiré superlattices can provide a new route to achieve strong polariton nonlinearities [111].

In moiré superlattices form in the nearly twist-aligned $WS_2/MoSe_2$ heterobilayer, the lowest-energy excitons states are moiré excitons with large oscillator strength. They form moiré polaritons when placed in a resonant cavity. Meanwhile, these moiré excitons are spatially confined in the moiré superlattice, leading to strong on-site exciton-exciton interactions and exciton blockade in a moiré unit cell. In another word, each moiré unit cell functions as a quantum dot and single exciton filling in each cell leads to full saturation of its oscillator strength. Effectively, the period of the moiré superlattice replaces the Bohr radius as the length scale for polariton nonlinearity, without affecting the binding energy and Borh radius of the moiré excitons. Such a moiré exciton-polariton system can exhibit a nonlinearity enhanced by $(a_M/a_B)^2 \sim 10 - 100$. It introduces quantum dot-like nonlinearity into a cooperatively coupled solid-state system, opening a door to novel quantum many-body physics and polariton devices [111]. Theoretical studies on moiré polaritons predict single or multiphoton lasing [265] and non-local interactions, which can lead to steady states with broken translational symmetry [266].

4.4. Manipulation of TMDCs polaritons

TMDCs provide a platform on which polariton properties can be manipulated with unprecedented flexibility via both the excitonic and photonic components. In polariton systems based on conventional materials, the exciton properties are largely determined by the as-fabricated material and tuning is limited by the requirement of integration with high-quality microcavities; the cavity materials and cavity structures used are also highly restricted due to the requirements of integration. In contrast, TMDCs can be readily integrated with a variety of cavity materials and structures (see Sec. 4.2) while at the same time, TMDC excitons can still be controlled through electrical contacts placed in close proximity and by the broad freedom in 2D heterostructure engineering (see Sec. 2.3).

To manipulate the material, electrically doping the TMDC layers can continuously tune the

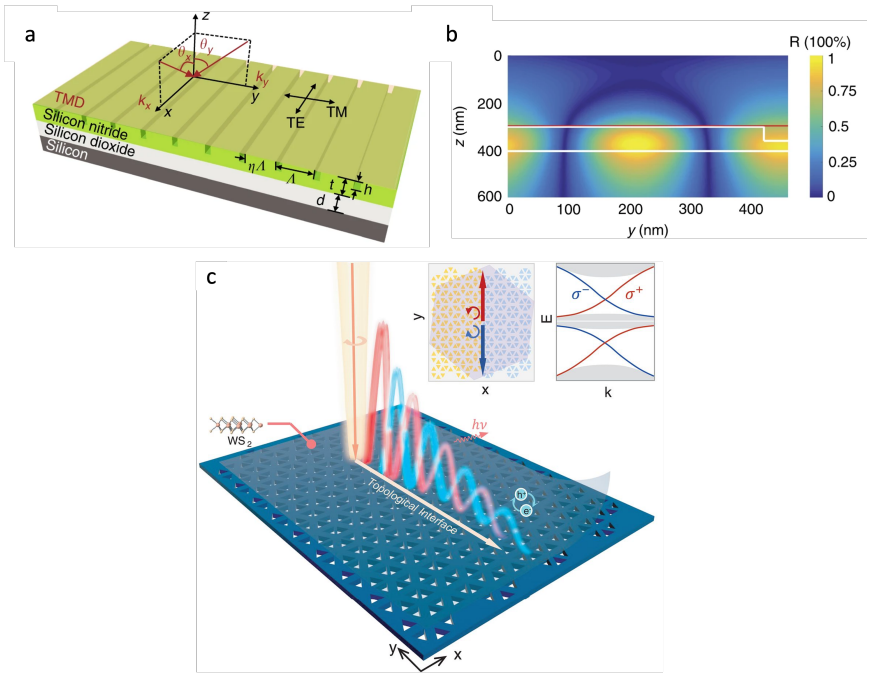

Fig. 31. Manipulation of TMDC polaritons. (a) Schematic of a 1D photonic grating cavity structure and its (b) simulated electric field profile of the TE mode. Reprinted from [240]. (c) Topological exciton polaritons. Reprinted with permission from [W. Liu, Z. Ji, Y. Wang, G. Modi, M. Hwang, B. Zheng, V. J. Sorger, A. Pan, and R. Agarwal, Science, 370, 600-604, 2020] [247].

TMDC-cavity system between strong and weak coupling regimes [267]. At low to moderate doping levels, trion or polaron polariton states can be studied [27,262]. The ultrafast optical Stark effect can be used to coherently manipulate polarization-selective valley polariton populations in TMDC [268]. Coupling between excitons, polaritons, and phonons can lead to hybridized states, which can be identified and studied using 2D spectroscopy techniques. The moiré superlattice can lead to quantum dot-array polaritons with enhanced noninearities [111].

To manipulate the cavity mode, photonic crystals can be used to generate interesting spatial symmetries, polarization selectivity, and topological properties [240, 247, 248], while these properties are transferred to polaritons when TMDCs are placed directly on the photonic crystals (Figure 31). In open vertical cavities, photonic lattices can be imprinted by etching the top DBR mirror, producing desired band structures of polaritons [269]. Naturally occurring dielectric disorders also modify the polariton energies of TMDCs, leading to trapped states or guided transport [270].

The multi-facet flexibility in integration and property engineering makes TMDC exciton polaritons a particularly attractive platform for room-temperature simulator of 1D and 2D Hamiltonians in condensed matter physics [271].

4.5. Polariton lasing in TMDCs system

In analogy to other bosonic systems, such as cold atoms and excitons, Bose-Einstein condensation can occur in polaritons, where a large number of polaritons occupy the same quantum state [46]. As a driven dissipative system where the photon component of the polariton has a fixed out-coupling rate from the cavity, a polariton condensate leads to coherent emission, called a polariton

laser. While conventional photon lasers require band inversion to establish stimulated scattering into the cavity mode, polariton condensates are formed by stimulated scattering into a polariton state as it approaches quantum degeneracy. Therefore, polariton condensation, and resulting polariton lasing, can take place at carrier densities many orders of magnitude below that required for conventional semiconductor lasing.

Although polariton condensation and lasing have been well established in GaAs and a number of other material systems, it has been challenging in TMDCs. To obtain quantum degeneracy, lighter effective mass, long polariton lifetime, and faster scattering rate to the lower energy polariton states are preferred. In TMDCs, the relatively higher density of defects in the materials and the lower quality of the cavity introduce significant loss and decoherence to the polariton states. Moreover, the weaker nonlinearity of the TMDC exciton limits the energy relaxation rate. Most recently, polariton lasing has been reported in a $MoSe_2$ monolayer assisted by a nearby GaAs quantum well, at cryogenetic temperature [228]. At room temperature, threshold behavior and increased spatial coherence have been reported in a WSe_2 monolayer [272]. Combining recent improvements in both material and cavity qualities may enable room-temperature polariton lasing in the near future.

5. Summary

In conclusion, TMDCs form a new class of excitonic materials with not only many unique physical properties but also unprecedented flexibility for engineering heterostructures and integration with photonic systems. A wealth of novel phenomena and device concepts have been explored, while abundant opportunities of new discoveries await.

Excitons with homogeneous linewidth have been demonstrated in TMDCs with hBN encapsulation, which is of great significance to identify coherent quantum states. Electronic and excitonic systems in heterostructures, especially in multi-layer moiré lattices and quasi-crystal lattices, will continue to be a testbed for novel fundamental phenomena. They may serve as quantum simulators with further technological development in fabrication, integration, and control. In TMDCs-cavity systems, combining excitons of homogeneous linewidth and a cavity of a high quality factor has yet to be demonstrated, which may enable macroscopic quantum states in TMDCs polaritons. Electrically injected polariton lasers in TMDCs system will be sought after as coherent light sources with high power efficiency, room-temperature operation, and compact size.

6. Acknowledgement

E.P., L.Z. and H.D. acknowledge the support by the Army Research Office (W911NF-17-1-0312); Office of Naval Research (N00014-21-1-2770); Air Force Office of Scientific Research (FA2386-21-1-4066); and National Science Foundation (DMR 2132470, DMR 2004287). L.Z. acknowledge the support by National Key Research and Development Program of China (2022YFA1206700); National Natural Science Foundation of China (No.62175207).

7. Data availability

No data were generated or analyzed in the presented research.

8. Disclosures

The authors declare no conflicts of interest.

9. Biography

Eunice Paik is currently a research scientist at the Army Research Laboratory. Her research interests include optical spectroscopy and photonics of two-dimensional and topological materials. She received her Ph.D. from University of Michigan and B.A. from Wellesley College.

Long Zhang is currently a Professor in the Department of Physics at the Xiamen University. He received Ph.D. in Optics from Fudan University, Shanghai, in 2015, and then worked as postdoc in the University of Michigan. In 2020, he joined Xiamen University as an Associate Professor. His current interest is the investigation of novel electronic and optical phenomena in 2D materials integrated with microcavities.

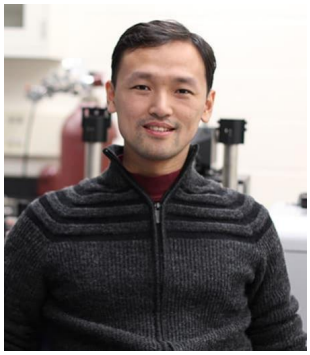

Kin Fai Mak is a Professor of Physics at Cornell University. His research combines techniques from nanoscale electronics and from optics to study the behavior of electrons in two-dimensional materials. His research is focused on understanding unusual electronic phenomena that occur when electrons are confined in crystals only a few atoms thick.

Jie Shan is a Professor of Engineering at Cornell University. Her research focuses on the optical and electronic properties of nanoscale materials. Of particular interest are atomically thin two-dimensional crystals (such as graphene and MoS_2) and their heterostructures. She develops experimental techniques to probe, image and control the internal degrees of freedom of electrons and their new phases in these nanoscale systems, and uses Various linear and nonlinear optical spectroscopy and microscopy techniques to access both the steady state properties and ultrafast dynamics.

Hui Deng Hui Deng is a Professor of Physics and Electrical and Computer Engineering at the University of Michigan, Ann Arbor. She currently serves as an Associate Editor of Advances in Optics and Photonics and a member of the Advisory Board of Physical Review X Quantum. Her lab focuses on light-matter interactions in van der Waals materials, phase transitions in strongly coupled charge and photon systems based on III-As or 2D materials in novel photonic structures, and applications of these systems to new photonic technologies and quantum information science.

References

1. K. S. Novoselov, A. K. Geim, S. V. Morozov, D. Jiang, Y. Zhang, S. V. Dubonos, I. V. Grigorieva, and A. A. Firsov, "Electric field effect in atomically thin carbon films," Science **306**, 666–669 (2004).
2. W. Liao, Y. Huang, H. Wang, and H. Zhang, "Van der waals heterostructures for optoelectronics: Progress and prospects," Appl. Mater. Today **16**, 435–455 (2019).
3. K. F. Mak and J. Shan, "Photonics and optoelectronics of 2D semiconductor transition metal dichalcogenides," Nat. Photonics **10**, 216–226 (2016).
4. C.-H. Lee, G.-H. Lee, A. M. van der Zande, W. Chen, Y. Li, M. Han, X. Cui, G. Arefe, C. Nuckolls, T. F. Heinz, J. Guo, J. Hone, and P. Kim, "Atomically thin p–n junctions with van der waals heterointerfaces," Nat. Nanotechnol. **9**, 676–681 (2014).
5. J. S. Ross, P. Rivera, J. Schaibley, E. Lee-Wong, H. Yu, T. Taniguchi, K. Watanabe, J. Yan, D. Mandrus, D. Cobden, W. Yao, and X. Xu, "Interlayer exciton optoelectronics in a 2d heterostructure p–n junction," Nano Lett. **17**, 638–643 (2017).
6. L. A. Jauregui, A. Y. Joe, K. Pistunova, D. S. Wild, A. A. High, Y. Zhou, G. Scuri, K. D. Greve, A. Sushko, C.-H. Yu, T. Taniguchi, K. Watanabe, D. J. Needleman, M. D. Lukin, H. Park, and P. Kim, "Electrical control of interlayer exciton dynamics in atomically thin heterostructures," Science **366**, 870–875 (2019).
7. M. M. Fogler, L. V. Butov, and K. S. Novoselov, "High-temperature superfluidity with indirect excitons in van der Waals heterostructures," Nat. Commun. **5**, 4555 (2014).
8. F.-C. Wu, F. Xue, and A. H. MacDonald, "Theory of two-dimensional spatially indirect equilibrium exciton condensates," Phys. Rev. B **92**, 165121 (2015).
9. D. G. Baranov, M. Wersäll, J. Cuadra, T. J. Antosiewicz, and T. Shegai, "Novel nanostructures and materials for strong light–matter interactions," ACS Photonics **5**, 24–42 (2018).

10. A. C. Dias, F. Qu, D. L. Azevedo, and J. Fu, "Band structure of monolayer transition-metal dichalcogenides and topological properties of their nanoribbons: Next-nearest-neighbor hopping," Phys. Rev. B **98**, 075202 (2018).
11. A. Splendiani, L. Sun, Y. Zhang, T. Li, J. Kim, C.-Y. Chim, G. Galli, and F. Wang, "Emerging photoluminescence in monolayer mos2," Nano Lett. **10**, 1271–1275 (2010).
12. K. F. Mak, C. Lee, J. Hone, J. Shan, and T. F. Heinz, "Atomically thin mos_2: A new direct-gap semiconductor," Phys. Rev. Lett. **105**, 136805 (2010).
13. M. Chhowalla, H. S. Shin, G. Eda, L.-J. Li, K. P. Loh, and H. Zhang, "The chemistry of two-dimensional layered transition metal dichalcogenide nanosheets," Nat. Chem. **5**, 263–275 (2013).
14. Z. Y. Zhu, Y. C. Cheng, and U. Schwingenschlögl, "Giant spin-orbit-induced spin splitting in two-dimensional transition-metal dichalcogenide semiconductors," Phys. Rev. B **84**, 153402 (2011).
15. D. Xiao, G.-B. Liu, W. Feng, X. Xu, and W. Yao, "Coupled spin and valley physics in monolayers of mos_2 and other group-vi dichalcogenides," Phys. Rev. Lett. **108**, 196802 (2012).
16. G. Wang, C. Robert, A. Suslu, B. Chen, S. Yang, S. Alamdari, I. C. Gerber, T. Amand, X. Marie, S. Tongay, and B. Urbaszek, "Spin-orbit engineering in transition metal dichalcogenide alloy monolayers," Nat. Commun. **6**, 10110 (2015).
17. M. V. Berry, "Quantal phase factors accompanying adiabatic changes," Proc. Royal Soc. London. A. Math. Phys. Sci. **392**, 45–57 (1984).
18. D. Xiao, M.-C. Chang, and Q. Niu, "Berry phase effects on electronic properties," Rev. Mod. Phys. **82**, 1959–2007 (2010).
19. K. F. Mak, D. Xiao, and J. Shan, "Light–valley interactions in 2D semiconductors," Nat. Photonics **12**, 451–460 (2018).
20. J. R. Schaibley, H. Yu, G. Clark, P. Rivera, J. S. Ross, K. L. Seyler, W. Yao, and X. Xu, "Valleytronics in 2D materials," Nat. Rev. Mater. **1**, 16055 (2016).
21. M. Sidler, P. Back, O. Cotlet, A. Srivastava, T. Fink, M. Kroner, E. Demler, and A. Imamoglu, "Fermi polaron-polaritons in charge-tunable atomically thin semiconductors," Nat. Phys. **13**, 255–261 (2017).
22. C. Fey, P. Schmelcher, A. Imamoglu, and R. Schmidt, "Theory of exciton-electron scattering in atomically thin semiconductors," Phys. Rev. B **101**, 195417 (2020).
23. C. Riva, F. M. Peeters, and K. Varga, "Excitons and charged excitons in semiconductor quantum wells," Phys. Rev. B **61**, 13873–13881 (2000).
24. K. F. Mak, K. He, C. Lee, G. H. Lee, J. Hone, T. F. Heinz, and J. Shan, "Tightly bound trions in monolayer mos2," Nat. Mater. **12**, 207–211 (2013).
25. T. C. Berkelbach, M. S. Hybertsen, and D. R. Reichman, "Theory of neutral and charged excitons in monolayer transition metal dichalcogenides," Phys. Rev. B **88**, 045318 (2013).
26. S. Dhara, C. Chakraborty, K. M. Goodfellow, L. Qiu, T. A. O'Loughlin, G. W. Wicks, S. Bhattacharjee, and A. N. Vamivakas, "Anomalous dispersion of microcavity trion-polaritons," Nat. Phys. **14**, 130–133 (2018).
27. R. P. A. Emmanuele, M. Sich, O. Kyriienko, V. Shahnazaryan, F. Withers, A. Catanzaro, P. M. Walker, F. A. Benimetskiy, M. S. Skolnick, A. I. Tartakovskii, I. A. Shelykh, and D. N. Krizhanovskii, "Highly nonlinear trion-polaritons in a monolayer semiconductor," Nat. Commun. **11**, 3589 (2020).
28. O. Kyriienko, D. Krizhanovskii, and I. Shelykh, "Nonlinear Quantum Optics with Trion Polaritons in 2D Monolayers: Conventional and Unconventional Photon Blockade," Phys. Rev. Lett. **125**, 197402 (2020).
29. G. Wang, A. Chernikov, M. M. Glazov, T. F. Heinz, X. Marie, T. Amand, and B. Urbaszek, "*Colloquium* : Excitons in atomically thin transition metal dichalcogenides," Rev. Mod. Phys. **90**, 021001 (2018).
30. A. Chernikov, T. C. Berkelbach, H. M. Hill, A. Rigosi, Y. Li, O. B. Aslan, D. R. Reichman, M. S. Hybertsen, and T. F. Heinz, "Exciton binding energy and nonhydrogenic rydberg series in monolayer ws_2," Phys. Rev. Lett. **113**, 076802 (2014).
31. H. Haug and S. W. Koch, *Quantum theory of the optical and electronic properties of semiconductors* (World Scientific, 2004), 4th ed.
32. C. F. Klingshirn, *Semiconductor Optics* (Springer, 2012), 4th ed.
33. I. Pelant and J. Valenta, *Luminescence spectroscopy of semiconductors* (Oxford University Press, 2012).
34. X. L. Yang, S. H. Guo, F. T. Chan, K. W. Wong, and W. Y. Ching, "Analytic solution of a two-dimensional hydrogen atom. i. nonrelativistic theory," Phys. Rev. A **43**, 1186–1196 (1991).
35. K. He, N. Kumar, L. Zhao, Z. Wang, K. F. Mak, H. Zhao, and J. Shan, "Tightly bound excitons in monolayer wse_2," Phys. Rev. Lett. **113**, 026803 (2014).
36. P. Cudazzo, I. V. Tokatly, and A. Rubio, "Dielectric screening in two-dimensional insulators: Implications for excitonic and impurity states in graphane," Phys. Rev. B **84**, 085406 (2011).
37. F. García Flórez, L. D. A. Siebbeles, and H. T. C. Stoof, "Effects of material thickness and surrounding dielectric medium on coulomb interactions and two-dimensional excitons," Phys. Rev. B **102**, 125303 (2020).
38. S. Latini, T. Olsen, and K. S. Thygesen, "Excitons in van der waals heterostructures: The important role of dielectric screening," Phys. Rev. B **92**, 245123 (2015).
39. N. S. Rytova, "Screened potential of a point charge in a thin film," (2018).
40. L. V. Keldysh, "Coulomb interaction in thin semiconductor and semimetal films," Sov. J. Exp. Theor. Phys. Lett. **29**, 658 (1979).
41. M. M. Ugeda, A. J. Bradley, S.-F. Shi, F. H. da Jornada, Y. Zhang, D. Y. Qiu, W. Ruan, S.-K. Mo, Z. Hussain, Z.-X.

Shen, F. Wang, S. G. Louie, and M. F. Crommie, "Giant bandgap renormalization and excitonic effects in a monolayer transition metal dichalcogenide semiconductor," Nat. Mater. **13**, 1091–1095 (2014).
42. J. Gu, V. Walther, L. Waldecker, D. Rhodes, A. Raja, J. C. Hone, T. F. Heinz, S. Kéna-Cohen, T. Pohl, and V. M. Menon, "Enhanced nonlinear interaction of polaritons via excitonic Rydberg states in monolayer WSe 2," Nat Commun **12**, 2269 (2021).
43. E. Malic, M. Selig, M. Feierabend, S. Brem, D. Christiansen, F. Wendler, A. Knorr, and G. Berghäuser, "Dark excitons in transition metal dichalcogenides," Phys. Rev. Mater. **2**, 014002 (2018).
44. X.-X. Zhang, Y. You, S. Y. F. Zhao, and T. F. Heinz, "Experimental evidence for dark excitons in monolayer wse_2," Phys. Rev. Lett. **115**, 257403 (2015).
45. T. Edvinsson, "Optical quantum confinement and photocatalytic properties in two-, one- and zero-dimensional nanostructures," Royal Soc. open science **5**, 180387–180387 (2018).
46. H. Deng, H. Haug, and Y. Yamamoto, "Exciton-polariton bose-einstein condensation," Rev. Mod. Phys. **82**, 1489–1537 (2010).
47. T. Cheiwchanchamnangij and W. R. L. Lambrecht, "Quasiparticle band structure calculation of monolayer, bilayer, and bulk mos_2," Phys. Rev. B **85**, 205302 (2012).
48. M. M. Glazov, T. Amand, X. Marie, D. Lagarde, L. Bouet, and B. Urbaszek, "Exciton fine structure and spin decoherence in monolayers of transition metal dichalcogenides," Phys. Rev. B **89**, 201302 (2014).
49. M. Palummo, M. Bernardi, and J. C. Grossman, "Exciton radiative lifetimes in two-dimensional transition metal dichalcogenides," Nano Lett. **15**, 2794–2800 (2015).
50. B. Deveaud, F. Clérot, N. Roy, K. Satzke, B. Sermage, and D. S. Katzer, "Enhanced radiative recombination of free excitons in gaas quantum wells," Phys. Rev. Lett. **67**, 2355–2358 (1991).
51. G. Moody, C. Kavir Dass, K. Hao, C.-H. Chen, L.-J. Li, A. Singh, K. Tran, G. Clark, X. Xu, G. Berghäuser, E. Malic, A. Knorr, and X. Li, "Intrinsic homogeneous linewidth and broadening mechanisms of excitons in monolayer transition metal dichalcogenides," Nat. Commun. **6**, 8315 (2015).
52. F. Cadiz, E. Courtade, C. Robert, G. Wang, Y. Shen, H. Cai, T. Taniguchi, K. Watanabe, H. Carrere, D. Lagarde, M. Manca, T. Amand, P. Renucci, S. Tongay, X. Marie, and B. Urbaszek, "Excitonic linewidth approaching the homogeneous limit in mos_2-based van der waals heterostructures," Phys. Rev. X **7**, 021026 (2017).
53. H. H. Fang, B. Han, C. Robert, M. A. Semina, D. Lagarde, E. Courtade, T. Taniguchi, K. Watanabe, T. Amand, B. Urbaszek, M. M. Glazov, and X. Marie, "Control of the exciton radiative lifetime in van der waals heterostructures," Phys. Rev. Lett. **123**, 067401 (2019).
54. E. W. Martin, J. Horng, H. G. Ruth, E. Paik, M.-H. Wentzel, H. Deng, and S. T. Cundiff, "Encapsulation narrows and preserves the excitonic homogeneous linewidth of exfoliated monolayer $mose_2$," Phys. Rev. Appl. **14**, 021002 (2020).
55. G. Z. Magda, J. Pető, G. Dobrik, C. Hwang, L. P. Biró, and L. Tapasztó, "Exfoliation of large-area transition metal chalcogenide single layers," Sci. Reports **5**, 14714 (2015).
56. M. Velický, G. E. Donnelly, W. R. Hendren, S. McFarland, D. Scullion, W. J. I. DeBenedetti, G. C. Correa, Y. Han, A. J. Wain, M. A. Hines, D. A. Muller, K. S. Novoselov, H. D. Abruña, R. M. Bowman, E. J. G. Santos, and F. Huang, "Mechanism of gold-assisted exfoliation of centimeter-sized transition-metal dichalcogenide monolayers," ACS Nano **12**, 10463–10472 (2018).
57. F. Liu, W. Wu, Y. Bai, S. H. Chae, Q. Li, J. Wang, J. Hone, and X.-Y. Zhu, "Disassembling 2D van der Waals crystals into macroscopic monolayers and reassembling into artificial lattices," Science **367**, 903–906 (2020).
58. J.-Y. Moon, M. Kim, S.-I. Kim, S. Xu, J.-H. Choi, D. Whang, K. Watanabe, T. Taniguchi, D. S. Park, J. Seo, S. H. Cho, S.-K. Son, and J.-H. Lee, "Layer-engineered large-area exfoliation of graphene," Sci. Adv. **6**, eabc6601 (2020).
59. Q. Li, A. Alfrey, J. Hu, N. Lydick, E. Paik, B. Liu, H. Sun, Y. Lu, R. Wang, S. Forrest, and H. Deng, "Macroscopic transition metal dichalcogenides monolayers with uniformly high optical quality," Nat. Commun. **14**, 1837 (2023).
60. Y.-H. Lee, X.-Q. Zhang, W. Zhang, M.-T. Chang, C.-T. Lin, K.-D. Chang, Y.-C. Yu, J. T.-W. Wang, C.-S. Chang, L.-J. Li, and T.-W. Lin, "Synthesis of large-area mos2 atomic layers with chemical vapor deposition," Adv. Mater. **24**, 2320–2325 (2012).
61. Y. Shi, W. Zhou, A.-Y. Lu, W. Fang, Y.-H. Lee, A. L. Hsu, S. M. Kim, K. K. Kim, H. Y. Yang, L.-J. Li, J.-C. Idrobo, and J. Kong, "van der waals epitaxy of mos2 layers using graphene as growth templates," Nano Lett. **12**, 2784–2791 (2012).
62. X. Lu, M. I. B. Utama, J. Lin, X. Gong, J. Zhang, Y. Zhao, S. T. Pantelides, J. Wang, Z. Dong, Z. Liu, W. Zhou, and Q. Xiong, "Large-area synthesis of monolayer and few-layer mose2 films on sio2 substrates," Nano Lett. **14**, 2419–2425 (2014).
63. Y.-H. Chang, W. Zhang, Y. Zhu, Y. Han, J. Pu, J.-K. Chang, W.-T. Hsu, J.-K. Huang, C.-L. Hsu, M.-H. Chiu, T. Takenobu, H. Li, C.-I. Wu, W.-H. Chang, A. T. S. Wee, and L.-J. Li, "Monolayer mose2 grown by chemical vapor deposition for fast photodetection," ACS Nano **8**, 8582–8590 (2014).
64. Y. Zhang, Y. Zhang, Q. Ji, J. Ju, H. Yuan, J. Shi, T. Gao, D. Ma, M. Liu, Y. Chen, X. Song, H. Y. Hwang, Y. Cui, and Z. Liu, "Controlled growth of high-quality monolayer ws2 layers on sapphire and imaging its grain boundary," ACS Nano **7**, 8963–8971 (2013).
65. Y. Gao, Z. Liu, D.-M. Sun, L. Huang, L.-P. Ma, L.-C. Yin, T. Ma, Z. Zhang, X.-L. Ma, L.-M. Peng, H.-M. Cheng, and W. Ren, "Large-area synthesis of high-quality and uniform monolayer ws2 on reusable au foils," Nat. Commun. **6**, 8569 (2015).
66. R. Yue, Y. Nie, L. A. Walsh, R. Addou, C. Liang, N. Lu, A. T. Barton, H. Zhu, Z. Che, D. Barrera, L. Cheng,

P.-R. Cha, Y. J. Chabal, J. W. P. Hsu, J. Kim, M. J. Kim, L. Colombo, R. M. Wallace, K. Cho, and C. L. Hinkle, "Nucleation and growth of wse2: enabling large grain transition metal dichalcogenides," 2D Mater. **4**, 045019 (2017).
67. S. M. Poh, X. Zhao, S. J. R. Tan, D. Fu, W. Fei, L. Chu, D. Jiadong, W. Zhou, S. J. Pennycook, A. H. Castro Neto, and K. P. Loh, "Molecular beam epitaxy of highly crystalline mose2 on hexagonal boron nitride," ACS Nano **12**, 7562–7570 (2018).
68. J. J. Pyeon, S. H. Kim, D. S. Jeong, S.-H. Baek, C.-Y. Kang, J.-S. Kim, and S. K. Kim, "Wafer-scale growth of mos2 thin films by atomic layer deposition," Nanoscale **8**, 10792–10798 (2016).
69. X. Liu, Q. Guo, and J. Qiu, "Emerging low-dimensional materials for nonlinear optics and ultrafast photonics," Adv. Mater. **29**, 1605886 (2017).
70. A. Autere, H. Jussila, Y. Dai, Y. Wang, H. Lipsanen, and Z. Sun, "Nonlinear optics with 2d layered materials," Adv. Mater. **30**, 1705963 (2018).
71. D. S. Wild, E. Shahmoon, S. F. Yelin, and M. D. Lukin, "Quantum nonlinear optics in atomically thin materials," Phys. Rev. Lett. **121**, 123606 (2018).
72. J. You, S. Bongu, Q. Bao, and N. Panoiu, "Nonlinear optical properties and applications of 2d materials: theoretical and experimental aspects," Nanophotonics **8**, 63–97 (2019).
73. J. Kim, X. Hong, C. Jin, S.-F. Shi, C.-Y. S. Chang, M.-H. Chiu, L.-J. Li, and F. Wang, "Ultrafast generation of pseudo-magnetic field for valley excitons in WSe2 monolayers," Science **346**, 1205–1208 (2014).
74. X. Li, M. Bamba, Q. Zhang, S. Fallahi, G. C. Gardner, W. Gao, M. Lou, K. Yoshioka, M. J. Manfra, and J. Kono, "Vacuum bloch–siegert shift in landau polaritons with ultra-high cooperativity," Nat. Photonics **12**, 324–329 (2018).
75. P. Tonndorf, R. Schmidt, P. Böttger, X. Zhang, J. Börner, A. Liebig, M. Albrecht, C. Kloc, O. Gordan, D. R. T. Zahn, S. M. de Vasconcellos, and R. Bratschitsch, "Photoluminescence emission and raman response of monolayer mos2, mose2, and wse2," Opt. Express **21**, 4908–4916 (2013).
76. T. Jakubczyk, V. Delmonte, M. Koperski, K. Nogajewski, C. Faugeras, W. Langbein, M. Potemski, and J. Kasprzak, "Radiatively limited dephasing and exciton dynamics in mose2 monolayers revealed with four-wave mixing microscopy," Nano Lett. **16**, 5333–5339 (2016).
77. C. Poellmann, P. Steinleitner, U. Leierseder, P. Nagler, G. Plechinger, M. Porer, R. Bratschitsch, C. Schüller, T. Korn, and R. Huber, "Resonant internal quantum transitions and femtosecond radiative decay of excitons in monolayer wse2," Nat. Mater. **14**, 889–893 (2015).
78. C. Robert, D. Lagarde, F. Cadiz, G. Wang, B. Lassagne, T. Amand, A. Balocchi, P. Renucci, S. Tongay, B. Urbaszek, and X. Marie, "Exciton radiative lifetime in transition metal dichalcogenide monolayers," Phys. Rev. B **93**, 205423 (2016).
79. P. Back, S. Zeytinoglu, A. Ijaz, M. Kroner, and A. Imamoğlu, "Realization of an Electrically Tunable Narrow-Bandwidth Atomically Thin Mirror Using Monolayer ${\mathrm{MoSe}}_{2}$," Phys. Rev. Lett. **120**, 037401 (2018).
80. G. Scuri, Y. Zhou, A. A. High, D. S. Wild, C. Shu, K. De Greve, L. A. Jauregui, T. Taniguchi, K. Watanabe, P. Kim, M. D. Lukin, and H. Park, "Large Excitonic Reflectivity of Monolayer ${\mathrm{MoSe}}_{2}$ Encapsulated in Hexagonal Boron Nitride," Phys. Rev. Lett. **120**, 037402 (2018).
81. J. Horng, E. W. Martin, Y.-H. Chou, E. Courtade, T.-c. Chang, C.-Y. Hsu, M.-H. Wentzel, H. G. Ruth, T.-c. Lu, S. T. Cundiff, F. Wang, and H. Deng, "Perfect Absorption by an Atomically Thin Crystal," Phys. Rev. Appl. **14**, 024009 (2020).
82. M. N. Islam, R. L. Hillman, D. A. B. Miller, D. S. Chemla, A. C. Gossard, and J. H. English, "Electroabsorption in gaas/algaas coupled quantum well waveguides," Appl. Phys. Lett. **50**, 1098–1100 (1987).
83. Z. Wang, Y.-H. Chiu, K. Honz, K. F. Mak, and J. Shan, "Electrical Tuning of Interlayer Exciton Gases in WSe_2 Bilayers," Nano Lett. **18**, 137–143 (2018).
84. K. F. Mak and J. Shan, "Opportunities and challenges of interlayer exciton control and manipulation," Nat. Nanotechnol. **13**, 974–976 (2018).
85. A. Ciarrocchi, D. Unuchek, A. Avsar, K. Watanabe, T. Taniguchi, and A. Kis, "Polarization switching and electrical control of interlayer excitons in two-dimensional van der waals heterostructures," Nat. Photonics **13**, 131–136 (2019).
86. Z. Huang, Y. Zhao, T. Bo, Y. Chu, J. Tian, L. Liu, Y. Yuan, F. Wu, J. Zhao, L. Xian, K. Watanabe, T. Taniguchi, R. Yang, D. Shi, L. Du, Z. Sun, S. Meng, W. Yang, and G. Zhang, "Spatially indirect intervalley excitons in bilayer Wse_2," Phys. Rev. B **105**, L041409 (2022).
87. J. P. Eisenstein and A. H. MacDonald, "Bose–Einstein condensation of excitons in bilayer electron systems," Nature **432**, 691–694 (2004).
88. Z. Wang, D. A. Rhodes, K. Watanabe, T. Taniguchi, J. C. Hone, J. Shan, and K. F. Mak, "Evidence of high-temperature exciton condensation in two-dimensional atomic double layers," Nature **574**, 76–80 (2019).
89. Q. Shi, E.-M. Shih, D. Rhodes, B. Kim, K. Barmak, K. Watanabe, T. Taniguchi, Z. Papić, D. A. Abanin, J. Hone, and C. R. Dean, "Bilayer wse2 as a natural platform for interlayer exciton condensates in the strong coupling limit," Nat. Nanotechnol. (2022).
90. J. I. A. Li, T. Taniguchi, K. Watanabe, J. Hone, and C. R. Dean, "Excitonic superfluid phase in double bilayer graphene," Nat. Phys. **13**, 751–755 (2017).
91. X. Liu, K. Watanabe, T. Taniguchi, B. I. Halperin, and P. Kim, "Quantum Hall drag of exciton condensate in graphene," Nat. Phys. **13**, 746–750 (2017).
92. L. Ma, P. X. Nguyen, Z. Wang, Y. Zeng, K. Watanabe, T. Taniguchi, A. H. MacDonald, K. F. Mak, and J. Shan,

"Strongly correlated excitonic insulator in atomic double layers," Nature **598**, 585–589 (2021).
93. Z. Zhang, E. C. Regan, D. Wang, W. Zhao, S. Wang, M. Sayyad, K. Yumigeta, K. Watanabe, T. Taniguchi, S. Tongay, M. Crommie, A. Zettl, M. P. Zaletel, and F. Wang, "Correlated interlayer exciton insulator in heterostructures of monolayer WSe2 and moiré WS2/WSe2," Nat. Phys. **18**, 1214–1220 (2022).
94. J. Gu, L. Ma, S. Liu, K. Watanabe, T. Taniguchi, J. C. Hone, J. Shan, and K. F. Mak, "Dipolar excitonic insulator in a moiré lattice," Nat. Phys. **18**, 395–400 (2022).
95. J. Horng, T. Stroucken, L. Zhang, E. Y. Paik, H. Deng, and S. W. Koch, "Observation of interlayer excitons in MoSe2 single crystals," Phys. Rev. B **97**, 241404 (2018).
96. I. C. Gerber, E. Courtade, S. Shree, C. Robert, T. Taniguchi, K. Watanabe, A. Balocchi, P. Renucci, D. Lagarde, X. Marie, and B. Urbaszek, "Interlayer excitons in bilayer MoS 2 with strong oscillator strength up to room temperature," Phys. Rev. B **99** (2019).
97. N. Leisgang, S. Shree, I. Paradisanos, L. Sponfeldner, C. Robert, D. Lagarde, A. Balocchi, K. Watanabe, T. Taniguchi, X. Marie, R. J. Warburton, I. C. Gerber, and B. Urbaszek, "Giant stark splitting of an exciton in bilayer mos(2)," Nat Nanotechnol **15**, 901–907 (2020). Leisgang, Nadine Shree, Shivangi Paradisanos, Ioannis Sponfeldner, Lukas Robert, Cedric Lagarde, Delphine Balocchi, Andrea Watanabe, Kenji Taniguchi, Takashi Marie, Xavier Warburton, Richard J Gerber, Iann C Urbaszek, Bernhard eng 2D-vdW-spin/Agence Nationale de la Recherche (French National Research Agency)/ VallEx/Agence Nationale de la Recherche (French National Research Agency)/ MagicValley/Agence Nationale de la Recherche (French National Research Agency)/ England 2020/08/12 Nat Nanotechnol. 2020 Nov;15(11):901-907. doi: 10.1038/s41565-020-0750-1. Epub 2020 Aug 10.
98. E. Lorchat, M. Selig, F. Katsch, K. Yumigeta, S. Tongay, A. Knorr, C. Schneider, and S. Höfling, "Excitons in bilayer mos_2 displaying a colossal electric field splitting and tunable magnetic response," Phys. Rev. Lett. **126**, 037401 (2021).
99. N. Peimyoo, T. Deilmann, F. Withers, J. Escolar, D. Nutting, T. Taniguchi, K. Watanabe, A. Taghizadeh, M. F. Craciun, K. S. Thygesen, and S. Russo, "Electrical tuning of optically active interlayer excitons in bilayer mos(2)," Nat Nanotechnol **16**, 888–893 (2021).
100. P. Rivera, J. R. Schaibley, A. M. Jones, J. S. Ross, S. Wu, G. Aivazian, P. Klement, K. Seyler, G. Clark, N. J. Ghimire, J. Yan, D. G. Mandrus, W. Yao, and X. Xu, "Observation of long-lived interlayer excitons in monolayer MoSe2–WSe2 heterostructures," Nat Commun **6**, 6242 (2015).
101. P. Rivera, K. L. Seyler, H. Yu, J. R. Schaibley, J. Yan, D. G. Mandrus, W. Yao, and X. Xu, "Valley-polarized exciton dynamics in a 2D semiconductor heterostructure," Science **351**, 688–691 (2016).
102. L. Zhang, R. Gogna, G. W. Burg, J. Horng, E. Paik, Y.-H. Chou, K. Kim, E. Tutuc, and H. Deng, "Highly valley-polarized singlet and triplet interlayer excitons in van der waals heterostructure," Phys. Rev. B **100**, 041402 (2019).
103. E. Liu, E. Barré, J. van Baren, M. Wilson, T. Taniguchi, K. Watanabe, Y.-T. Cui, N. M. Gabor, T. F. Heinz, Y.-C. Chang, and C. H. Lui, "Signatures of moiré trions in WSe2/MoSe2 heterobilayers," Nature **594**, 46–50 (2021).
104. M. Brotons-Gisbert, H. Baek, A. Campbell, K. Watanabe, T. Taniguchi, and B. D. Gerardot, "Moir\'e-Trapped Interlayer Trions in a Charge-Tunable ${\mathrm{WSe}}_{2}/{\mathrm{MoSe}}_{2}$ Heterobilayer," Phys. Rev. X **11**, 031033 (2021).
105. H. Heo, J. H. Sung, S. Cha, B.-G. Jang, J.-Y. Kim, G. Jin, D. Lee, J.-H. Ahn, M.-J. Lee, J. H. Shim, H. Choi, and M.-H. Jo, "Interlayer orientation-dependent light absorption and emission in monolayer semiconductor stacks," Nat. Commun. **6**, 7372 (2015).
106. M. Okada, A. Kutana, Y. Kureishi, Y. Kobayashi, Y. Saito, T. Saito, K. Watanabe, T. Taniguchi, S. Gupta, Y. Miyata, B. I. Yakobson, H. Shinohara, and R. Kitaura, "Direct and indirect interlayer excitons in a van der waals heterostructure of hbn/ws2/mos2/hbn," ACS Nano **12**, 2498–2505 (2018).
107. J. Kunstmann, F. Mooshammer, P. Nagler, A. Chaves, F. Stein, N. Paradiso, G. Plechinger, C. Strunk, C. Schüller, G. Seifert, D. R. Reichman, and T. Korn, "Momentum-space indirect interlayer excitons in transition-metal dichalcogenide van der waals heterostructures," Nat. Phys. **14**, 801–805 (2018).
108. O. Karni, E. Barré, S. C. Lau, R. Gillen, E. Y. Ma, B. Kim, K. Watanabe, T. Taniguchi, J. Maultzsch, K. Barmak, R. H. Page, and T. F. Heinz, "Infrared interlayer exciton emission in mos_2/wse_2 heterostructures," Phys. Rev. Lett. **123**, 247402 (2019).
109. L. Yuan, B. Zheng, J. Kunstmann, T. Brumme, A. B. Kuc, C. Ma, S. Deng, D. Blach, A. Pan, and L. Huang, "Twist-angle-dependent interlayer exciton diffusion in WS2–WSe2 heterobilayers," Nat. Mater. **19**, 617–623 (2020).
110. L. Zhang, Z. Zhang, F. Wu, D. Wang, R. Gogna, S. Hou, K. Watanabe, T. Taniguchi, K. Kulkarni, T. Kuo, S. R. Forrest, and H. Deng, "Twist-angle dependence of moiré excitons in WS 2 /MoSe 2 heterobilayers," Nat. Commun. **11**, 5888 (2020).
111. L. Zhang, F. Wu, S. Hou, Z. Zhang, Y.-H. Chou, K. Watanabe, T. Taniguchi, S. R. Forrest, and H. Deng, "Van der waals heterostructure polaritons with moiré-induced nonlinearity," Nature **591**, 61–65 (2021).
112. N. R. Wilson, P. V. Nguyen, K. Seyler, P. Rivera, A. J. Marsden, Z. P. L. Laker, G. C. Constantinescu, V. Kandyba, A. Barinov, N. D. M. Hine, X. Xu, and D. H. Cobden, "Determination of band offsets, hybridization, and exciton binding in 2d semiconductor heterostructures," Sci. Adv. **3**, e1601832 (2017).
113. X. Hong, J. Kim, S.-F. Shi, Y. Zhang, C. Jin, Y. Sun, S. Tongay, J. Wu, Y. Zhang, and F. Wang, "Ultrafast charge transfer in atomically thin mos2/ws2 heterostructures," Nat. Nanotechnol. **9**, 682–686 (2014).
114. Y. Jiang, S. Chen, W. Zheng, B. Zheng, and A. Pan, "Interlayer exciton formation, relaxation, and transport in TMD

van der Waals heterostructures," Light Sci Appl **10**, 72 (2021).
115. C. Jiang, W. Xu, A. Rasmita, Z. Huang, K. Li, Q. Xiong, and W.-b. Gao, "Microsecond dark-exciton valley polarization memory in two-dimensional heterostructures," Nat. Commun. **9**, 753 (2018).
116. R. Cheng, D. Li, H. Zhou, C. Wang, A. Yin, S. Jiang, Y. Liu, Y. Chen, Y. Huang, and X. Duan, "Electroluminescence and photocurrent generation from atomically sharp wse2/mos2 heterojunction p–n diodes," Nano Lett. **14**, 5590–5597 (2014). PMID: 25157588.
117. E. Barré, O. Karni, E. Liu, A. L. O'Beirne, X. Chen, H. B. Ribeiro, L. Yu, B. Kim, K. Watanabe, T. Taniguchi, K. Barmak, C. H. Lui, S. Refaely-Abramson, F. H. da Jornada, and T. F. Heinz, "Optical absorption of interlayer excitons in transition-metal dichalcogenide heterostructures," Science **376**, 406–410 (2022).
118. M. Koperski, M. R. Molas, A. Arora, K. Nogajewski, M. Bartos, J. Wyzula, D. Vaclavkova, P. Kossacki, and M. Potemski, "Orbital, spin and valley contributions to Zeeman splitting of excitonic resonances in MoSe $_2$, WSe $_2$ and WS $_2$ Monolayers," 2D Mater. **6**, 015001 (2018).
119. H. Yu, G.-B. Liu, and W. Yao, "Brightened spin-triplet interlayer excitons and optical selection rules in van der Waals heterobilayers," 2D Mater. **5**, 035021 (2018).
120. T. Wang, S. Miao, Z. Li, Y. Meng, Z. Lu, Z. Lian, M. Blei, T. Taniguchi, K. Watanabe, S. Tongay, D. Smirnov, and S.-F. Shi, "Giant valley-zeeman splitting from spin-singlet and spin-triplet interlayer excitons in wse2/mose2 heterostructure," Nano Lett. **20**, 694–700 (2020). Doi: 10.1021/acs.nanolett.9b04528.
121. W.-T. Hsu, B.-H. Lin, L.-S. Lu, M.-H. Lee, M.-W. Chu, L.-J. Li, W. Yao, W.-H. Chang, and C.-K. Shih, "Tailoring excitonic states of van der Waals bilayers through stacking configuration, band alignment, and valley spin," Sci. Adv. **5**, eaax7407 (2019).
122. E. C. Regan, D. Wang, E. Y. Paik, Y. Zeng, L. Zhang, J. Zhu, A. H. MacDonald, H. Deng, and F. Wang, "Emerging exciton physics in transition metal dichalcogenide heterobilayers," Nat. Rev. Mater. (2022).
123. E. C. Regan, D. Wang, C. Jin, M. I. Bakti Utama, B. Gao, X. Wei, S. Zhao, W. Zhao, Z. Zhang, K. Yumigeta, M. Blei, J. D. Carlström, K. Watanabe, T. Taniguchi, S. Tongay, M. Crommie, A. Zettl, and F. Wang, "Mott and generalized Wigner crystal states in WSe2/WS2 moiré superlattices," Nature **579**, 359–363 (2020).
124. Y. Tang, L. Li, T. Li, Y. Xu, S. Liu, K. Barmak, K. Watanabe, T. Taniguchi, A. H. MacDonald, J. Shan, and K. F. Mak, "Simulation of hubbard model physics in wse2/ws2 moire superlattices," Nature **579**, 353–358 (2020).
125. Y. Xu, S. Liu, D. A. Rhodes, K. Watanabe, T. Taniguchi, J. Hone, V. Elser, K. F. Mak, and J. Shan, "Correlated insulating states at fractional fillings of moiré superlattices," Nature **587**, 214–218 (2020).
126. Y. Shimazaki, I. Schwartz, K. Watanabe, T. Taniguchi, M. Kroner, and A. Imamoğlu, "Strongly correlated electrons and hybrid excitons in a moiré heterostructure," Nature **580**, 472–477 (2020).
127. L. Wang, E.-M. Shih, A. Ghiotto, L. Xian, D. A. Rhodes, C. Tan, M. Claassen, D. M. Kennes, Y. Bai, B. Kim, K. Watanabe, T. Taniguchi, X. Zhu, J. Hone, A. Rubio, A. N. Pasupathy, and C. R. Dean, "Correlated electronic phases in twisted bilayer transition metal dichalcogenides," Nat. Mater. **19**, 861–866 (2020).
128. D. M. Kennes, M. Claassen, L. Xian, A. Georges, A. J. Millis, J. Hone, C. R. Dean, D. N. Basov, A. N. Pasupathy, and A. Rubio, "Moiré heterostructures as a condensed-matter quantum simulator," Nat. Phys. **17**, 155–163 (2021).
129. I. Schwartz, Y. Shimazaki, C. Kuhlenkamp, K. Watanabe, T. Taniguchi, M. Kroner, and A. Imamoğlu, "Electrically tunable feshbach resonances in twisted bilayer semiconductors," Science **374**, 336–340 (2021).
130. C. Kuhlenkamp, M. Knap, M. Wagner, R. Schmidt, and A. m. c. Imamoğlu, "Tunable feshbach resonances and their spectral signatures in bilayer semiconductors," Phys. Rev. Lett. **129**, 037401 (2022).
131. K. L. Seyler, P. Rivera, H. Yu, N. P. Wilson, E. L. Ray, D. G. Mandrus, J. Yan, W. Yao, and X. Xu, "Signatures of moiré-trapped valley excitons in MoSe2/WSe2 heterobilayers," Nature **567**, 66–70 (2019).
132. C. Jin, E. C. Regan, A. Yan, M. Iqbal Bakti Utama, D. Wang, S. Zhao, Y. Qin, S. Yang, Z. Zheng, S. Shi, K. Watanabe, T. Taniguchi, S. Tongay, A. Zettl, and F. Wang, "Observation of moiré excitons in WSe 2 /WS 2 heterostructure superlattices," Nature **567**, 76–80 (2019).
133. F. Wu, T. Lovorn, and A. H. MacDonald, "Theory of optical absorption by interlayer excitons in transition metal dichalcogenide heterobilayers," Phys. Rev. B **97**, 035306 (2018).
134. K. Tran, G. Moody, F. Wu, X. Lu, J. Choi, K. Kim, A. Rai, D. A. Sanchez, J. Quan, A. Singh, J. Embley, A. Zepeda, M. Campbell, T. Autry, T. Taniguchi, K. Watanabe, N. Lu, S. K. Banerjee, K. L. Silverman, S. Kim, E. Tutuc, L. Yang, A. H. MacDonald, and X. Li, "Evidence for moiré excitons in van der Waals heterostructures," Nature **567**, 71–75 (2019).
135. C. Jin, E. C. Regan, D. Wang, M. Iqbal Bakti Utama, C.-S. Yang, J. Cain, Y. Qin, Y. Shen, Z. Zheng, K. Watanabe, T. Taniguchi, S. Tongay, A. Zettl, and F. Wang, "Identification of spin, valley and moiré quasi-angular momentum of interlayer excitons," Nat. Phys. **15**, 1140–1144 (2019).
136. Y. Tang, J. Gu, S. Liu, K. Watanabe, T. Taniguchi, J. Hone, K. F. Mak, and J. Shan, "Tuning layer-hybridized moiré excitons by the quantum-confined Stark effect," Nat. Nanotechnol. **16**, 52–57 (2021).
137. J. Choi, W.-T. Hsu, L.-S. Lu, L. Sun, H.-Y. Cheng, M.-H. Lee, J. Quan, K. Tran, C.-Y. Wang, M. Staab, K. Jones, T. Taniguchi, K. Watanabe, M.-W. Chu, S. Gwo, S. Kim, C.-K. Shih, X. Li, and W.-H. Chang, "Moiré potential impedes interlayer exciton diffusion in van der Waals heterostructures," Sci. Adv. **6**, eaba8866 (2020).
138. Z. Li, X. Lu, D. F. Cordovilla Leon, Z. Lyu, H. Xie, J. Hou, Y. Lu, X. Guo, A. Kaczmarek, T. Taniguchi, K. Watanabe, L. Zhao, L. Yang, and P. B. Deotare, "Interlayer Exciton Transport in MoSe2/WSe2 Heterostructures," ACS Nano **15**, 1539–1547 (2021).
139. S. Gupta, A. Kutana, and B. I. Yakobson, "Heterobilayers of 2D materials as a platform for excitonic superfluidity,"

Nat. Commun. **11**, 2989 (2020).
140. E. Y. Paik, L. Zhang, G. W. Burg, R. Gogna, E. Tutuc, and H. Deng, "Interlayer exciton laser of extended spatial coherence in atomically thin heterostructures," Nature **576**, 80–84 (2019).
141. A. F. Rigosi, H. M. Hill, Y. Li, A. Chernikov, and T. F. Heinz, "Probing interlayer interactions in transition metal dichalcogenide heterostructures by optical spectroscopy: MoS_2/WS_2 and $MoSe_2/WSe_2$," Nano Lett. **15**, 5033–5038 (2015).
142. C. Zhang, C.-P. Chuu, X. Ren, M.-Y. Li, L.-J. Li, C. Jin, M.-Y. Chou, and C.-K. Shih, "Interlayer couplings, Moiré patterns, and 2D electronic superlattices in MoS_2/WSe_2 hetero-bilayers," Sci. Adv. **3** (2017).
143. Y. Liu, H. Fang, A. Rasmita, Y. Zhou, J. Li, T. Yu, Q. Xiong, N. Zheludev, J. Liu, and W. Gao, "Room temperature nanocavity laser with interlayer excitons in 2D heterostructures," SCIENCE ADVANCES p. 6 (2019).
144. L. V. Butov, "Cold exciton gases in coupled quantum well structures," J. Physics. Condens. Matter: An Inst. Phys. J. **19**, 295202 (2007).
145. D. Snoke, "Spontaneous bose coherence of excitons and polaritons," Science **298**, 1368–1372 (2002).
146. D. Snoke and P. Littlewood, "Polariton condensates," Phys. Today **63**, 42–47 (2010).
147. J. M. Kosterlitz and D. J. Thouless, "Ordering, metastability and phase transitions in two-dimensional systems," J. Phys. C: Solid State Phys. **6**, 1181 (1973).
148. A. Posazhennikova, "Colloquium: Weakly interacting, dilute bose gases in 2d," Rev. Mod. Phys. **78**, 1111–1134 (2006).
149. Z. Hadzibabic and J. Dalibard, "Two-dimensional Bose fluids: An atomic physics perspective," La Rivista del Nuovo Cimento **34**, 389–434 (2011).
150. P. López Ríos, A. Perali, R. J. Needs, and D. Neilson, "Evidence from quantum monte carlo simulations of large-gap superfluidity and bcs-bec crossover in double electron-hole layers," Phys. Rev. Lett. **120**, 177701 (2018).
151. M. Xie and A. H. MacDonald, "Electrical reservoirs for bilayer excitons," Phys. Rev. Lett. **121**, 067702 (2018).
152. S. Conti, M. Van der Donck, A. Perali, F. M. Peeters, and D. Neilson, "Doping-dependent switch from one- to two-component superfluidity in coupled electron-hole van der waals heterostructures," Phys. Rev. B **101**, 220504 (2020).
153. O. L. Berman and R. Y. Kezerashvili, "High-temperature superfluidity of the two-component bose gas in a transition metal dichalcogenide bilayer," Phys. Rev. B **93**, 245410 (2016).
154. B. Debnath, Y. Barlas, D. Wickramaratne, M. R. Neupane, and R. K. Lake, "Exciton condensate in bilayer transition metal dichalcogenides: Strong coupling regime," Phys. Rev. B **96**, 174504 (2017).
155. D. Nandi, A. D. K. Finck, J. P. Eisenstein, L. N. Pfeiffer, and K. W. West, "Exciton condensation and perfect Coulomb drag," Nature **488**, 481–484 (2012).
156. X. Liu, J. I. A. Li, K. Watanabe, T. Taniguchi, J. Hone, B. I. Halperin, P. Kim, and C. R. Dean, "Crossover between strongly coupled and weakly coupled exciton superfluids," Science **375**, 205–209 (2022).
157. G. W. Burg, N. Prasad, K. Kim, T. Taniguchi, K. Watanabe, A. H. MacDonald, L. F. Register, and E. Tutuc, "Strongly enhanced tunneling at total charge neutrality in double-bilayer graphene-wse_2 heterostructures," Phys. Rev. Lett. **120**, 177702 (2018).
158. S. De Palo, F. Rapisarda, and G. Senatore, "Excitonic condensation in a symmetric electron-hole bilayer," Phys. Rev. Lett. **88**, 206401 (2002).
159. P. Rivera, H. Yu, K. L. Seyler, N. P. Wilson, W. Yao, and X. Xu, "Interlayer valley excitons in heterobilayers of transition metal dichalcogenides," Nat. Nanotechnol. **13**, 1004–1015 (2018).
160. M. A. Baranov, M. Dalmonte, G. Pupillo, and P. Zoller, "Condensed matter theory of dipolar quantum gases," Chem. Rev. **112**, 5012–5061 (2012).
161. Y. Zeng and A. H. MacDonald, "Electrically controlled two-dimensional electron-hole fluids," Phys. Rev. B **102**, 085154 (2020).
162. B. I. Halperin and T. M. Rice, "Possible anomalies at a semimetal-semiconductor transistion," Rev. Mod. Phys. **40**, 755–766 (1968).
163. D. Jérome, T. M. Rice, and W. Kohn, "Excitonic insulator," Phys. Rev. **158**, 462–475 (1967).
164. W. Kohn and D. Sherrington, "Two kinds of bosons and bose condensates," Rev. Mod. Phys. **42**, 1–11 (1970).
165. R. C. Ashoori, H. L. Stormer, J. S. Weiner, L. N. Pfeiffer, S. J. Pearton, K. W. Baldwin, and K. W. West, "Single-electron capacitance spectroscopy of discrete quantum levels," Phys. Rev. Lett. **68**, 3088–3091 (1992).
166. J. P. Eisenstein, L. N. Pfeiffer, and K. W. West, "Negative compressibility of interacting two-dimensional electron and quasiparticle gases," Phys. Rev. Lett. **68**, 674–677 (1992).
167. A. F. Young and L. S. Levitov, "Capacitance of graphene bilayer as a probe of layer-specific properties," Phys. Rev. B **84**, 085441 (2011).
168. N. F. Mott, "The transition to the metallic state," The Philos. Mag. A J. Theor. Exp. Appl. Phys. **6**, 287–309 (1961).
169. Y. E. Lozovik, I. L. Kurbakov, G. E. Astrakharchik, J. Boronat, and M. Willander, "Strong correlation effects in 2D Bose–Einstein condensed dipolar excitons," Solid State Commun. **144**, 399–404 (2007).
170. V. DeGiorgio and M. O. Scully, "Analogy between the laser threshold region and a second-order phase transition," Phys. Rev. A **2**, 1170–1177 (1970).
171. R. Graham and H. Haken, "Laserlight — first example of a second-order phase transition far away from thermal equilibrium," Zeitschrift für Physik **237**, 31–46 (1970).
172. M. O. Scully, "Condensation of N bosons and the laser phase transition analogy," Phys. Rev. Lett. **82**, 3927–3931

(1999).
173. B. Y.-K. Hu, "Prospecting for the superfluid transition in electron-hole coupled quantum wells using coulomb drag," Phys. Rev. Lett. **85**, 820–823 (2000).
174. D. K. Efimkin and V. Galitski, "Anomalous coulomb drag in electron-hole bilayers due to the formation of excitons," Phys. Rev. Lett. **116**, 046801 (2016).
175. C. P. Morath, J. A. Seamons, J. L. Reno, and M. P. Lilly, "Density imbalance effect on the coulomb drag upturn in an undoped electron-hole bilayer," Phys. Rev. B **79**, 041305 (2009).
176. E. Y. Andrei, D. K. Efetov, P. Jarillo-Herrero, A. H. MacDonald, K. F. Mak, T. Senthil, E. Tutuc, A. Yazdani, and A. F. Young, "The marvels of moiré materials," Nat. Rev. Mater. **6**, 201–206 (2021).
177. F. Wu, T. Lovorn, E. Tutuc, and A. H. MacDonald, "Hubbard model physics in transition metal dichalcogenide moiré bands," Phys. Rev. Lett. **121**, 026402 (2018).
178. Y. Zhang, N. F. Q. Yuan, and L. Fu, "Moiré quantum chemistry: Charge transfer in transition metal dichalcogenide superlattices," Phys. Rev. B **102**, 201115 (2020).
179. H. Pan, F. Wu, and S. Das Sarma, "Band topology, hubbard model, heisenberg model, and dzyaloshinskii-moriya interaction in twisted bilayer wse_2," Phys. Rev. Res. **2**, 033087 (2020).
180. H. Pan, F. Wu, and S. Das Sarma, "Quantum phase diagram of a moiré-hubbard model," Phys. Rev. B **102**, 201104 (2020).
181. A. Ghiotto, E.-M. Shih, G. S. S. G. Pereira, D. A. Rhodes, B. Kim, J. Zang, A. J. Millis, K. Watanabe, T. Taniguchi, J. C. Hone, L. Wang, C. R. Dean, and A. N. Pasupathy, "Quantum criticality in twisted transition metal dichalcogenides," Nature **597**, 345–349 (2021).
182. X. Huang, T. Wang, S. Miao, C. Wang, Z. Li, Z. Lian, T. Taniguchi, K. Watanabe, S. Okamoto, D. Xiao, S.-F. Shi, and Y.-T. Cui, "Correlated insulating states at fractional fillings of the WS2/WSe2 moiré lattice," Nat. Phys. **17**, 715–719 (2021).
183. T. Li, S. Jiang, L. Li, Y. Zhang, K. Kang, J. Zhu, K. Watanabe, T. Taniguchi, D. Chowdhury, L. Fu, J. Shan, and K. F. Mak, "Continuous Mott transition in semiconductor moiré superlattices," Nature **597**, 350–354 (2021).
184. T. Li, S. Jiang, B. Shen, Y. Zhang, L. Li, Z. Tao, T. Devakul, K. Watanabe, T. Taniguchi, L. Fu, J. Shan, and K. F. Mak, "Quantum anomalous Hall effect from intertwined moiré bands," Nature **600**, 641–646 (2021).
185. Y.-H. Zhang, "Doping a Mott insulator with excitons in a moir\'e bilayer: Fractional superfluid, neutral Fermi surface, and Mott transition," Phys. Rev. B **106**, 195120 (2022).
186. Y.-H. Zhang, D. N. Sheng, and A. Vishwanath, "Su(4) chiral spin liquid, exciton supersolid, and electric detection in moiré bilayers," Phys. Rev. Lett. **127**, 247701 (2021).
187. Y. Zeng, Z. Xia, R. Dery, K. Watanabe, T. Taniguchi, J. Shan, and K. F. Mak, "Exciton density waves in Coulomb-coupled dual moiré lattices," Nat. Mater. **22**, 175–179 (2023).
188. Y. Zeng, N. Wei, and A. H. MacDonald, "Layer pseudospin magnetism in a transition metal dichalcogenide double-moir\'e system," Phys. Rev. B **106**, 165105 (2022).
189. I. Bloch, J. Dalibard, and S. Nascimbène, "Quantum simulations with ultracold quantum gases," Nat. Phys. **8**, 267–276 (2012).
190. Y. Xu, K. Kang, K. Watanabe, T. Taniguchi, K. F. Mak, and J. Shan, "Tunable bilayer hubbard model physics in twisted wse2," (2022).
191. X. Xu, W. Yao, D. Xiao, and T. F. Heinz, "Spin and pseudospins in layered transition metal dichalcogenides," Nat. Phys. **10**, 343–350 (2014).
192. F. Wu, T. Lovorn, and A. H. MacDonald, "Topological exciton bands in moiré heterojunctions," Phys. Rev. Lett. **118**, 147401 (2017).
193. X. M. Chen and J. J. Quinn, "Excitonic charge-density-wave instability of spatially separated electron-hole layers in strong magnetic fields," Phys. Rev. Lett. **67**, 895–898 (1991).
194. H. P. Büchler and G. Blatter, "Supersolid versus phase separation in atomic bose-fermi mixtures," Phys. Rev. Lett. **91**, 130404 (2003).
195. Y. N. Joglekar, A. V. Balatsky, and S. Das Sarma, "Wigner supersolid of excitons in electron-hole bilayers," Phys. Rev. B **74**, 233302 (2006).
196. I. Titvinidze, M. Snoek, and W. Hofstetter, "Supersolid bose-fermi mixtures in optical lattices," Phys. Rev. Lett. **100**, 100401 (2008).
197. F. Wu, T. Lovorn, E. Tutuc, I. Martin, and A. H. MacDonald, "Topological insulators in twisted transition metal dichalcogenide homobilayers," Phys. Rev. Lett. **122**, 086402 (2019).
198. H. Li, S. Li, E. C. Regan, D. Wang, W. Zhao, S. Kahn, K. Yumigeta, M. Blei, T. Taniguchi, K. Watanabe, S. Tongay, A. Zettl, M. F. Crommie, and F. Wang, "Imaging two-dimensional generalized Wigner crystals," Nature **597**, 650–654 (2021).
199. E. Liu, T. Taniguchi, K. Watanabe, N. M. Gabor, Y.-T. Cui, and C. H. Lui, "Excitonic and valley-polarization signatures of fractional correlated electronic phases in a wse_2/ws_2 moiré superlattice," Phys. Rev. Lett. **127**, 037402 (2021).
200. S. Miao, T. Wang, X. Huang, D. Chen, Z. Lian, C. Wang, M. Blei, T. Taniguchi, K. Watanabe, S. Tongay, Z. Wang, D. Xiao, Y.-T. Cui, and S.-F. Shi, "Strong interaction between interlayer excitons and correlated electrons in WSe2/WS2 moiré superlattice," Nat. Commun. **12**, 3608 (2021).
201. A. J. Campbell, M. Brotons-Gisbert, H. Baek, V. Vitale, T. Taniguchi, K. Watanabe, J. Lischner, and B. D. Gerardot,

"Exciton-polarons in the presence of strongly correlated electronic states in a MoSe2/WSe2 moiré superlattice," npj 2D Mater Appl **6**, 1–8 (2022).
202. W. Li, L. M. Devenica, J. Zhang, Y. Zhang, X. Lu, K. Watanabe, T. Taniguchi, A. Rubio, and A. Srivastava, "Local sensing of correlated electrons in dual-moiré heterostructures using dipolar excitons," (2021).
203. A. Raja, A. Chaves, J. Yu, G. Arefe, H. M. Hill, A. F. Rigosi, T. C. Berkelbach, P. Nagler, C. Schüller, T. Korn, C. Nuckolls, J. Hone, L. E. Brus, T. F. Heinz, D. R. Reichman, and A. Chernikov, "Coulomb engineering of the bandgap and excitons in two-dimensional materials," Nat. Commun. **8**, 15251 (2017).
204. M. Imada, A. Fujimori, and Y. Tokura, "Metal-insulator transitions," Rev. Mod. Phys. **70**, 1039–1263 (1998).
205. N. F. Mott, "Metal-insulator transition," Rev. Mod. Phys. **40**, 677–683 (1968).
206. T. Senthil, "Theory of a continuous mott transition in two dimensions," Phys. Rev. B **78**, 045109 (2008).
207. R. V. Mishmash, I. González, R. G. Melko, O. I. Motrunich, and M. P. A. Fisher, "Continuous mott transition between a metal and a quantum spin liquid," Phys. Rev. B **91**, 235140 (2015).
208. S. Musser, T. Senthil, and D. Chowdhury, "Theory of a continuous bandwidth-tuned Wigner-Mott transition," Phys. Rev. B **106**, 155145 (2022).
209. Y. Xu, X.-C. Wu, M. Ye, Z.-X. Luo, C.-M. Jian, and C. Xu, "Interaction-Driven Metal-Insulator Transition with Charge Fractionalization," Phys. Rev. X **12**, 021067 (2022).
210. A. Szasz, J. Motruk, M. P. Zaletel, and J. E. Moore, "Chiral spin liquid phase of the triangular lattice hubbard model: A density matrix renormalization group study," Phys. Rev. X **10**, 021042 (2020).
211. Y. Tang, J. Gu, S. Liu, K. Watanabe, T. Taniguchi, J. C. Hone, K. F. Mak, and J. Shan, "Dielectric catastrophe at the Wigner-Mott transition in a moiré superlattice," Nat Commun **13**, 4271 (2022).
212. C. Aebischer, D. Baeriswyl, and R. M. Noack, "Dielectric catastrophe at the mott transition," Phys. Rev. Lett. **86**, 468–471 (2001).
213. A. A. Koulakov, M. M. Fogler, and B. I. Shklovskii, "Charge density wave in two-dimensional electron liquid in weak magnetic field," Phys. Rev. Lett. **76**, 499–502 (1996).
214. V. J. Emery, S. A. Kivelson, and J. M. Tranquada, "Stripe phases in high-temperature superconductors," Proc. National Acad. Sci. United States Am. **96**, 8814–8817 (1999).
215. C. Jin, Z. Tao, T. Li, Y. Xu, Y. Tang, J. Zhu, S. Liu, K. Watanabe, T. Taniguchi, J. C. Hone, L. Fu, J. Shan, and K. F. Mak, "Stripe phases in WSe2/WS2 moiré superlattices," Nat. Mater. **20**, 940–944 (2021).
216. M. Matty and E.-A. Kim, "Melting of generalized Wigner crystals in transition metal dichalcogenide heterobilayer Moiré systems," Nat Commun **13**, 7098 (2022).
217. P. W. Anderson, "Antiferromagnetism. theory of superexchange interaction," Phys. Rev. **79**, 350–356 (1950).
218. Y. Tang, K. Su, L. Li, Y. Xu, S. Liu, K. Watanabe, T. Taniguchi, J. Hone, C.-M. Jian, C. Xu, K. F. Mak, and J. Shan, "Evidence of frustrated magnetic interactions in a wigner–mott insulator," Nat. Nanotechnol. **18**, 233–237 (2023).
219. J. Knörzer, M. J. A. Schuetz, G. Giedke, D. S. Wild, K. De Greve, R. Schmidt, M. D. Lukin, and J. I. Cirac, "Wigner crystals in two-dimensional transition-metal dichalcogenides: Spin physics and readout," Phys. Rev. B **101**, 125101 (2020).
220. Y. Tang, K. Su, L. Li, Y. Xu, S. Liu, K. Watanabe, T. Taniguchi, J. Hone, C.-M. Jian, C. Xu, K. F. Mak, and J. Shan, "Evidence of frustrated magnetic interactions in a Wigner–Mott insulator," Nat. Nanotechnol. **18**, 233–237 (2023).
221. J. Merino, B. J. Powell, and R. H. McKenzie, "Ferromagnetism, paramagnetism, and a curie-weiss metal in an electron-doped hubbard model on a triangular lattice," Phys. Rev. B **73** (2006).
222. Y. Nagaoka, "Ferromagnetism in a narrow, almost half-filled *s* band," Phys. Rev. **147**, 392–405 (1966).
223. N. C. Hu and A. H. MacDonald, "Competing magnetic states in transition metal dichalcogenide moiré materials," Phys. Rev. B **104**, 214403 (2021).
224. N. Morales-Durán, N. C. Hu, P. Potasz, and A. H. MacDonald, "Nonlocal interactions in moiré hubbard systems," Phys. Rev. Lett. **128**, 217202 (2022).
225. A. E. Siegman, *Lasers* (University Science Books, 1986).
226. D. Kleppner, "Inhibited spontaneous emission," Phys. Rev. Lett. **47**, 233–236 (1981).
227. J. J. Hopfield, "Theory of the contribution of excitons to the complex dielectric constant of crystals," Phys. Rev. **112**, 1555–1567 (1958).
228. C. Anton-Solanas, M. Waldherr, M. Klaas, H. Suchomel, T. H. Harder, H. Cai, E. Sedov, S. Klembt, A. V. Kavokin, S. Tongay, K. Watanabe, T. Taniguchi, S. Höfling, and C. Schneider, "Bosonic condensation of exciton–polaritons in an atomically thin crystal," Nat. Mater. **20**, 1233–1239 (2021).
229. K. J. Vahala, "Optical microcavities," Nature **424**, 839–846 (2003).
230. B. E. A. Saleh and M. C. Teich, *Fundamentals of photonics*, Wiley series in pure and applied optics (Wiley, 1991).
231. K. Srinivasan, M. Borselli, O. Painter, A. Stintz, and S. Krishna, "Cavity q, mode volume, and lasing threshold in small diameter algaas microdisks with embedded quantum dots," Opt. Express **14**, 1094–1105 (2006).
232. G. R. Fowles, *Introduction to Modern Optics*, Dover Books on Physics (Dover Publications, 2012).
233. B. Osting, "Bragg structure and the first spectral gap," Appl. Math. Lett. **25**, 1926–1930 (2012).
234. Y. Yamamoto, F. Tassone, and H. Cao, *Semiconductor cavity quantum electrodynamics*, Springer tracts in modern physics (Springer, 2000).
235. X. Liu, T. Galfsky, Z. Sun, F. Xia, E.-c. Lin, Y.-H. Lee, S. Kéna-Cohen, and V. M. Menon, "Strong light–matter coupling in two-dimensional atomic crystals," Nat. Photon **9**, 30–34 (2015).
236. N. Lundt, M. Klaas, E. Sedov, M. Waldherr, H. Knopf, M. Blei, S. Tongay, S. Klembt, T. Taniguchi, K. Watanabe,

U. Schulz, A. Kavokin, S. Höfling, F. Eilenberger, and C. Schneider, "Magnetic-field-induced splitting and polarization of monolayer-based valley exciton polaritons," Phys. Rev. B **100**, 121303 (2019).
237. S. Dufferwiel, S. Schwarz, F. Withers, A. A. P. Trichet, F. Li, M. Sich, O. Del Pozo-Zamudio, C. Clark, A. Nalitov, D. D. Solnyshkov, G. Malpuech, K. S. Novoselov, J. M. Smith, M. S. Skolnick, D. N. Krizhanovskii, and A. I. Tartakovskii, "Exciton–polaritons in van der Waals heterostructures embedded in tunable microcavities," Nat. Commun. **6**, 8579 (2015).
238. N. Lundt, L. Dusanowski, E. Sedov, P. Stepanov, M. M. Glazov, S. Klembt, M. Klaas, J. Beierlein, Y. Qin, S. Tongay, M. Richard, A. V. Kavokin, S. Höfling, and C. Schneider, "Optical valley Hall effect for highly valley-coherent exciton-polaritons in an atomically thin semiconductor," Nat. Nanotechnol. **14**, 770–775 (2019).
239. E. Y. Paik, L. Zhang, S. Hou, H. Zhao, Y.-H. Chou, S. R. Forrest, and H. Deng, "High quality factor microcavity for van der waals semiconductor polaritons using a transferrable mirror," Adv. Opt. Mater. **11**, 2201440 (2023).
240. L. Zhang, R. Gogna, W. Burg, E. Tutuc, and H. Deng, "Photonic-crystal exciton-polaritons in monolayer semiconductors," Nat. Commun. **9**, 1–8 (2018).
241. J. O. Grepstad, M. M. Greve, B. Holst, I.-R. Johansen, O. Solgaard, and A. Sudbø, "Finite-size limitations on quality factor of guided resonance modes in 2d photonic crystals," Opt. Express **21**, 23640–23654 (2013).
242. D. Rosenblatt, A. Sharon, and A. Friesem, "Resonant grating waveguide structures," IEEE J. Quantum Electron. **33**, 2038–2059 (1997).
243. S. Fan and J. D. Joannopoulos, "Analysis of guided resonances in photonic crystal slabs," Phys. Rev. B **65**, 235112 (2002).
244. R. Gogna, L. Zhang, Z. Wang, and H. Deng, "Photonic crystals for controlling strong coupling in van der waals materials," Opt. Express **27**, 22700 (2019).
245. V. Kravtsov, E. Khestanova, F. A. Benimetskiy, T. Ivanova, A. K. Samusev, I. S. Sinev, D. Pidgayko, A. M. Mozharov, I. S. Mukhin, M. S. Lozhkin, Y. V. Kapitonov, A. S. Brichkin, V. D. Kulakovskii, I. A. Shelykh, A. I. Tartakovskii, P. M. Walker, M. S. Skolnick, D. N. Krizhanovskii, and I. V. Iorsh, "Nonlinear polaritons in a monolayer semiconductor coupled to optical bound states in the continuum," Light. Sci. & Appl. **9**, 56 (2020).
246. Y. Chen, S. Miao, T. Wang, D. Zhong, A. Saxena, C. Chow, J. Whitehead, D. Gerace, X. Xu, S.-F. Shi, and A. Majumdar, "Metasurface integrated monolayer exciton polariton," Nano Lett. **20**, 5292–5300 (2020).
247. W. Liu, Z. Ji, Y. Wang, G. Modi, M. Hwang, B. Zheng, V. J. Sorger, A. Pan, and R. Agarwal, "Generation of helical topological exciton-polaritons," Science **370**, 600–604 (2020).
248. M. Li, I. Sinev, F. Benimetskiy, T. Ivanova, E. Khestanova, S. Kiriushechkina, A. Vakulenko, S. Guddala, M. Skolnick, V. M. Menon, D. Krizhanovskii, A. Alù, A. Samusev, and A. B. Khanikaev, "Experimental observation of topological Z2 exciton-polaritons in transition metal dichalcogenide monolayers," Nat. Commun. **12**, 4425 (2021).
249. D. Zheng, S. Zhang, Q. Deng, M. Kang, P. Nordlander, and H. Xu, "Manipulating coherent plasmon–exciton interaction in a single silver nanorod on monolayer WSe2," Nano Lett. **17**, 3809–3814 (2017).
250. J. Wen, H. Wang, W. Wang, Z. Deng, C. Zhuang, Y. Zhang, F. Liu, J. She, J. Chen, H. Chen, S. Deng, and N. Xu, "Room-temperature strong light–matter interaction with active control in single plasmonic nanorod coupled with two-dimensional atomic crystals," Nano Lett. **17**, 4689–4697 (2017).
251. Y. Jiang, H. Wang, S. Wen, H. Chen, and S. Deng, "Resonance Coupling in an Individual Gold Nanorod–Monolayer WS2 Heterostructure: Photoluminescence Enhancement with Spectral Broadening," ACS Nano **14**, 13841–13851 (2020).
252. J. Cuadra, D. G. Baranov, M. Wersäll, R. Verre, T. J. Antosiewicz, and T. Shegai, "Observation of tunable charged exciton polaritons in hybrid monolayer ws2 plasmonic nanoantenna system," Nano Lett. **18**, 1777–1785 (2018).
253. B. Munkhbat, D. G. Baranov, A. Bisht, M. A. Hoque, B. Karpiak, S. P. Dash, and T. Shegai, "Electrical Control of Hybrid Monolayer Tungsten Disulfide–Plasmonic Nanoantenna Light–Matter States at Cryogenic and Room Temperatures," ACS Nano **14**, 1196–1206 (2020).
254. J. Sun, Y. Li, H. Hu, W. Chen, D. Zheng, S. Zhang, and H. Xu, "Strong plasmon–exciton coupling in transition metal dichalcogenides and plasmonic nanostructures," Nanoscale **13**, 4408–4419 (2021).
255. J. Qin, Y.-H. Chen, Z. Zhang, Y. Zhang, R. J. Blaikie, B. Ding, and M. Qiu, "Revealing Strong Plasmon-Exciton Coupling between Nanogap Resonators and Two-Dimensional Semiconductors at Ambient Conditions," Phys. Rev. Lett. **124**, 063902 (2020).
256. W. Liu, B. Lee, C. H. Naylor, H.-S. Ee, J. Park, A. T. C. Johnson, and R. Agarwal, "Strong Exciton–Plasmon Coupling in MoS $_2$ Coupled with Plasmonic Lattice," Nano Lett. **16**, 1262–1269 (2016).
257. S. Wang, S. Li, T. Chervy, A. Shalabney, S. Azzini, E. Orgiu, J. A. Hutchison, C. Genet, P. Samorì, and T. W. Ebbesen, "Coherent Coupling of WS2 Monolayers with Metallic Photonic Nanostructures at Room Temperature," Nano Lett. **16**, 4368–4374 (2016).
258. B. Lee, W. Liu, C. H. Naylor, J. Park, S. C. Malek, J. S. Berger, A. T. C. Johnson, and R. Agarwal, "Electrical Tuning of Exciton–Plasmon Polariton Coupling in Monolayer MoS2 Integrated with Plasmonic Nanoantenna Lattice," Nano Lett. **17**, 4541–4547 (2017).
259. A. M. Dibos, Y. Zhou, L. A. Jauregui, G. Scuri, D. S. Wild, A. A. High, T. Taniguchi, K. Watanabe, M. D. Lukin, P. Kim, and H. Park, "Electrically Tunable Exciton–Plasmon Coupling in a WSe2 Monolayer Embedded in a Plasmonic Crystal Cavity," Nano Lett. **19**, 3543–3547 (2019).
260. L. Qiu, C. Chakraborty, S. Dhara, and A. N. Vamivakas, "Room-temperature valley coherence in a polaritonic system," Nat. Commun. **10**, 1513 (2019).

261. S. Dufferwiel, T. P. Lyons, D. D. Solnyshkov, A. A. P. Trichet, F. Withers, S. Schwarz, G. Malpuech, J. M. Smith, K. S. Novoselov, M. S. Skolnick, D. N. Krizhanovskii, and A. I. Tartakovskii, "Valley-addressable polaritons in atomically thin semiconductors," Nat. Photonics **11**, 497–501 (2017).
262. L. B. Tan, O. Cotlet, A. Bergschneider, R. Schmidt, P. Back, Y. Shimazaki, M. Kroner, and A. İmamoğlu, "Interacting polaron-polaritons," Phys. Rev. X **10**, 021011 (2020).
263. B. Datta, M. Khatoniar, P. Deshmukh, F. Thouin, R. Bushati, S. De Liberato, S. K. Cohen, and V. M. Menon, "Highly nonlinear dipolar exciton-polaritons in bilayer MoS2," Nat Commun **13**, 6341 (2022).
264. C. Louca, A. Genco, S. Chiavazzo, T. P. Lyons, S. Randerson, C. Trovatello, P. Claronino, R. Jayaprakash, X. Hu, J. Howarth, K. Watanabe, T. Taniguchi, S. Dal Conte, R. Gorbachev, D. G. Lidzey, G. Cerullo, O. Kyriienko, and A. I. Tartakovskii, "Interspecies exciton interactions lead to enhanced nonlinearity of dipolar excitons and polaritons in MoS2 homobilayers," Nat Commun **14**, 3818 (2023).
265. A. Camacho-Guardian and N. R. Cooper, "Moir\'e-Induced Optical Nonlinearities: Single- and Multiphoton Resonances," Phys. Rev. Lett. **128**, 207401 (2022).
266. A. Camacho-Guardian and N. R. Cooper, "Optical nonlinearities and spontaneous translational symmetry breaking in driven-dissipative moir\'e exciton-polaritons," Phys. Rev. B **106**, 245402 (2022).
267. B. Chakraborty, J. Gu, Z. Sun, M. Khatoniar, R. Bushati, A. L. Boehmke, R. Koots, and V. M. Menon, "Control of strong light–matter interaction in monolayer WS $_2$ through electric field gating," Nano Lett. **18**, 6455–6460 (2018).
268. T. LaMountain, J. Nelson, E. J. Lenferink, S. H. Amsterdam, A. A. Murthy, H. Zeng, T. J. Marks, V. P. Dravid, M. C. Hersam, and N. P. Stern, "Valley-selective optical stark effect of exciton-polaritons in a monolayer semiconductor," Nat. Commun. **12**, 4530 (2021).
269. L. Lackner, M. Dusel, O. A. Egorov, B. Han, H. Knopf, F. Eilenberger, S. Schröder, K. Watanabe, T. Taniguchi, S. Tongay, C. Anton-Solanas, S. Höfling, and C. Schneider, "Tunable exciton-polaritons emerging from WS2 monolayer excitons in a photonic lattice at room temperature," Nat. Commun. **12**, 4933 (2021).
270. M. Wurdack, E. Estrecho, S. Todd, T. Yun, M. Pieczarka, S. K. Earl, J. A. Davis, C. Schneider, A. G. Truscott, and E. A. Ostrovskaya, "Motional narrowing, ballistic transport, and trapping of room-temperature exciton polaritons in an atomically-thin semiconductor," Nat. Commun. **12**, 5366 (2021).
271. C. Schneider, K. Winkler, M. D. Fraser, M. Kamp, Y. Yamamoto, E. A. Ostrovskaya, and S. Höfling, "Exciton-polariton trapping and potential landscape engineering," Reports on Prog. Phys. **80**, 016503 (2017).
272. H. Shan, L. Lackner, B. Han, E. Sedov, C. Rupprecht, H. Knopf, F. Eilenberger, J. Beierlein, N. Kunte, M. Esmann, K. Yumigeta, K. Watanabe, T. Taniguchi, S. Klembt, S. Höfling, A. V. Kavokin, S. Tongay, C. Schneider, and C. Antón-Solanas, "Spatial coherence of room-temperature monolayer WSe2 exciton-polaritons in a trap," Nat. Commun. **12**, 6406 (2021).